微型渦輪引擎環型燃燒室對使用低熱值燃料之可容許性

模擬研究

學　　生　　:吳迪翰　　指導教授:陳俊勳

國立交通大學機械工程學系

摘要

本研究以商業套裝軟體 CFD-ACE+ 模擬微型氣渦輪引擎燃燒室在保持外型結構，但更換原廠預設的液態 Jet A1 燃料為較低熱值的氣態甲烷混合氣燃料時的燃燒流場。 所得之數值模擬計算結果在著重於經燃燒反應後所產生的推力值與熱傳效應所造成襯筒壁與燃燒室出口的高溫之探討。

研究中模擬四組的渦輪轉速條件(155000, 120000, 80000, 45000 轉/分)，並分別在各組的甲烷燃料中混入六種不同二氧化碳質量濃度(0%, 10%, 20%, 30%, 40%, 50%)來做為稀釋效應的研究。

模擬結果如下: (1) 甲烷燃料加入 CO_2 氣體後其產生的推力更低 (2) 半數襯筒壁可能會受高溫熱破壞 (3) 襯筒壁上稀釋孔所產生的噴流能有效降低燃燒室出口排氣溫度，使渦輪葉片不致產生熱破壞。由於 (2) 之模擬結果有待商確，因此有一系列的修正探討以作為未來改善之用。

Performance simulation analysis on low-heating value fuel acceptability of a micro gas turbine annular combustor operation

Student: Di-Han Wu Advisor: Prof. Chiun-Hsun Chen

Institute of Mechanical Engineering

National Chiao Tung University

Abstract

This thesis applies a commercial package CFD-ACE+ to simulate the combustion flow field in combustion chamber of a micro gas turbine. The purpose is to investigate whether the original structural configuration can sustain its power performance by using the low-heating-value methane gas instead of the original liquid Jet A1 fuel. The numerical data are mainly emphasized on the thrust generated by combustion power and the temperature distributions over solid annular liners and combustor outlet. In the research, one of the parameters is the turbine rotational speed. Four rotational speeds, 155000, 120000, 80000, and 45000 rpm, are considered. The other parameter is the mass fraction of CH_4 in the fuel mixture, consisting of CH_4 and CO_2. Six weight percentages of 100, 90, 80, 70, 60 and 50% are taken into consideration. The simulation results are as follows: (1) The thrust is reduced as a result of the addition of CO_2. (2) The liner walls in half parametric studies might be burnt out. (3) The hot gas exhausted from combustor outlet is cooled down effectively by jet flow discharged from dilution holes, which prevent turbine blade from heat damage. Finally, several recommendations are suggested for the possible future improvements and extensions.

誌謝

走筆至此，已是論文臻於完結的時候，心中感想萬千，情緒激昂。回想這兩年的研究與學習生活，喜樂苦悶交織；過程中讓我更知道時間規劃的重要性，誠懇溝通的必要性，沉著、冷靜思考的情緒鍛鍊，積極探求和打鐵趁熱的研究態度，以及培養面對人事物能有正面樂觀的爽朗心態，造就在未來期勉自己能邁開大步、勇敢向前的我。

本論文能順利完成要感念所有兩年來，給予我精神上支持鼓勵和實質上幫助的大家。感謝實驗室學長 俊翔、振忠，在論文與研究過程的討論與建議，期刊論文搜尋與投影片製作的教導與幫忙。 遠達，在電腦軟硬體上的解釋與幫忙。 文義、文奎，在模擬軟體上的彼此討論和學習。 彥成，兩次生日請客及豪爽個性。 榮貴，沉穩開朗態度和論文中 CAD 軟體建模的大力幫忙。 瑭原，幽默穩健和多種才藝的學習對象；同學 炳坤、建宏、耀文，感謝你們陪伴兩年來課業與生活上的彼此切磋學習與相互扶持，你們是我攻讀碩士學位的最佳戰友；學弟 皓正、仁浩、宏一、靖山、昇宏、彥佐、長新，雖然和你們相處的時間不長，但是你們的熱情與活力仍讓我感受良多；助理 雅雪，說話總是含蓄溫柔和在各種行政作業上的貼心幫忙。

最要感激的是吾師 陳俊勳教授，雖然老師日理萬機，接觸時間少，但在開會之時總能感受到老師對學術的嚴謹治學態度，和條理清晰的思路。感謝老師的諄諄教誨，學生不才，未能將論文內容臻於完善，在未來的路上，會謹記師訓認真負責。感謝口試委員的悉心建議與指導，讓我在論文相關領域知曉更深。

我尤其要將這份榮耀和我的家人分享，感謝爸爸 志明先生及媽媽 妙春女士多年來對我的付出與關愛，和包容我兩年來低潮時稚氣的抱怨，加上姐姐純瑾的打氣鼓舞，讓我能通過這心靈、體力與耐力的考驗，謝謝你們的支持，我愛你們！最後再一次感激所有曾經幫助過我的人，謝謝你們。

Contents

List of tables

List of figures

Nomenclature

a, b	constants
B	pre-exponential factor
C_p	constant-pressure specific heat
D_h	hydraulic diameter
D_i	mass diffusivity
Ea	activation energy
h	specific enthalpy
$h_{coef.}$	convection heat-transfer coefficient
I	turbulence intensity
k	thermal conductivity
k	turbulence energy
k	k-equation for turbulent model
k_r	reaction rate constant
M_i	molecular weight
$\dot{m}$	mass flow rate
p	pressure
Pr	Prandtl number
R	ideal gas constant
R_u	universal gas constant
Re	Reynolds number
s_{ij}	the rate of strain tensor
S_h	energy source
Sc	Schmidt number
T	temperature
u, v, w	velocity components in the (x, y, z) system of coordinates
u_i	velocity component
u+	velocity scale value
$\vec{V}$	velocity vector
x_i	Cartesian coordinate (i=1,2,3)
y+	length scale value
Y_i	mass fraction

Greek Symbols

α	temperature exponent
ρ	density
τ_{ij}	stress tensor component
ε	dissipation rate

ε	turbulence dissipation function
κ	von Karman's constant (Eq. 2-27)
σ_k, σ_ε	constants (Eq. 2-23, 2-24)
δ_{ij}	Kronecker Delta
μ	viscosity
η	efficiency
Φ_{ij}	dimensionless quantity
ω_i	molar production rate of species i
π	compression ratio

Overhead

$\bar{}$	time-averaged part

Superscript

‘	fluctuation about the ensemble average value
+	wall coordinates and wall variables
primary	primary zone of liner

Subscript

eff	effective
i, j, m	component / direction x, y, z
t	turbulent
p	constant pressure
r	reaction rate
mix	mixture
air	in air condition

Chapter 1
Introduction

1.1 Background

Gas turbine is a system device, which supplies jet propulsion and power. The nature of continuous processes in a gas turbine is that it can pass very much larger volume of gas flows than that of a piston engine in the same engine volume. The turbine size is relatively compact and it has a high power-to-weight ratio [1]. It is also more efficient compared with the reciprocate engine, because of its simple structure and less driving components, like crank, cam, and etc. In terms of power density, gas turbine is superior to traditional batteries.

Several applications are brought into practice based on above-mentioned merits. Recently, with the development of small scale gas turbine, which can be served as not only the propulsive power of MAV (Micro Air Vehicle) and UAV (Unmanned Aerial Vehicle), but also more probably the generators for those portable electronic equipments, such as notebook, PDA, cellular phones, GPS receivers, which demand high power density [2].

For the energy resource and environmental protection issues, there are other applications and advantages by using gas turbine. On the basis of high efficiency consideration, the idea is combined it with biomass fuels to accommodate the Distributed Power Generation [3]. In practice, this laboratory has been awarded a three-year integrated research project supported by National Science Council to upgrade the utilization efficiency of biogas by removing H_2S and improve the power generation rate. One of the subprojects is to develop a low heating value biogas fuel power system [4], whose objective is to modify the burner of a micro gas turbine (MGT) from a liquid-fuel burning gas turbine system into a gas-burning one to generate the combustion power, used to drive a generator to produce the electricity. Therefore, this numerical simulation work serves as a preliminary study for such re-modification of burner.

As mentioned above, the fuel employed in this prototype gas turbine is the relative low heating value methane gas [5] to replace the original liquid fuel of Jet A1 (aviation kerosene). The heating value of methane is range about $0.8\,MJ/mol$, which is much lower than kerosene one, $6.9\,MJ/mol$, at STP [6]. Therefore, it needs to supply a much larger mass flow rate of methane to fit the designed values for operating burner temperature and demanding thrust.

In addition to the concern of heating value, the phase state of liquid is different from that of gas. This difference would cause the mismatch of the gas turbine system. The components of gas turbine can be roughly divided into three parts: compressor, turbine wheel, combustion chamber. With introducing the low heating value (low calorific value) fuel, its total mass flow has a much greater fraction of air mass than that with a liquid fuel. Consequently, the mass flow passing turbine considerably exceeds the one passing compressor, and a mismatch between compressor and turbine will result. The reaction behaviors in combustion chamber are also changed. Therefore, it will affect the flow fields in the chamber and discharge characteristics via liner holes. That is to say, the three parts are essentially coupled with each other.

There are many variations on the basic structure of combustion chamber, however, all types of chambers generally incorporate with the key components, such as air casing, diffuser, liner, and fuel injector. The basic requirements for all combustors may be listed as follows: high combustion efficiency, reliable and smooth ignition, wide stability limits, low pressure loss, ideal outlet temperature distribution (pattern factor) for maximizing the life of turbine blades and nozzle guide vanes, low emissions of pollutant species, durability. Furthermore, for small-scale gas turbine, reduction of combustor size and weight are the additional and important requirements [7]. Hence, there is a stricter condition to adequate combustion in the limited-scale chamber. It implies that the difficulty which not only to expect fuel and air to be able to mix well to

obtain completely stable combustion in finite space but also to avoid the local hot point to damage turbine as a result of high and concentrated temperature. These practical requirements should be complied for modifying the combustion chamber.

It is assumed that the original chamber design for liquid fuel Jet A1 can work with the best power performance and ideal temperature distribution. As it converts into gas fuels that maybe emerge the above-mentioned problems. Thus, this work is motivated to study if the original chamber design is still worthy to be expected to maintain its performance or it needs other specific modification on its components.

1.2 Literature survey

The function of the liner is to provide a region of low velocity, where the combustion is sustained by a re-circulatory flow of burned products that provide a continuous source of ignition for the incoming fuel-air mixture. The air not used for combustion flows to downstream of the combustion zone to mix with the hot burned products and thereby reduces its temperature to a value that is acceptable by the turbine. In practice, it is customary to insert, between the primary and dilution zones, a so-called intermediate zone whose purpose is to recover losses due to chemical dissociation of the primary combustion products. This is done via the addition of small, discrete amounts of air. Hence, the hole shapes and configurations for these three zones are one of the important design features at liners [7].

Chomiak et al. [8] studied the problems and prospects for combustion of LCVG (low calorific value gases). They summarized that (1) the main problem in LCVG combustion is that of flame stability. (2) small size combustors offer minimum pressure losses for achieving the required high fluid uniformity in the flame stabilization zone.

Ho et al. [9] investigated the combustion characteristics of a miniature annual combustor experimentally. In experiments, the combustor inlet pressure, axial temperature distribution inside the combustor, and exhaust gas concentrations were measured. To study the operation range of the combustor, three sets of turndown ratio experiments were performed. It was found that the increase of the inlet pressure will decrease the value of the fuel lean limit. According to the temperature distribution, the optimal A/F ratio is changed with the operation pressure. The NO_x concentration will be increased with the increase of the temperature of the main combustion zone.

Crocker et al. [10] used a software CFD-ACE to simulate a combustor model from compressor diffuser exit to turbine inlet. The comprehensive model made it possible to predict flow splits for the various openings into the combustor liner and to remove the guesswork required for prescribing accurate boundary conditions for those openings. The coupled modeling of the flow inside and outside the liners, combined with conjugate heat transfer analysis and participating gas radiation, provided a direct prediction of liner wall temperatures. Non-luminous gas radiation added approximately 40K to the hot side of metal wall temperature.

Kousuke et al. [11] studied the micromachining gas turbine, which is under development at Tohoku University. In the research, they pointed out that based on the approximation of compressor casing being an adiabatic wall, the compressor efficiency is found to be feasible to achieve the efficiency required for closing the Brayton cycle. When the length scale of the gas turbine is large, this approximation is valid because the heat flow through the wall is negligible comparing to the heat carried by the main flow. However, for micro scale gas turbine, the heat transfer from the combustor and the turbine to the lower temperature components, such as the compressor, becomes large because the distance to separate the high and low temperature components is small, while the

highest and lowest temperature in the system are same as the macro-scale system, consequently, the temperature gradient becomes large. The compressor efficiencies by changing the adiabatic and isothermal wall condition with several different temperatures were calculated by computational fluid dynamics. The results showed that the efficiency drops as changing from the adiabatic wall to isothermal wall. The decrease of efficiency will cause the compressor efficiency too low to close Brayton cycle. Therefore, the micro-machine gas turbine cannot be directly utilized by just scaling down the same structure of the macro-scale gas turbine. It really needs a new heat shielding method.

Yamashita et al. [12] studied a laboratory-based MGT operated with the experimental conditions using low-heating value fuels simulated in terms of the dilution of LPG (liquefied petroleum gas) with N_2. Efficiencies at each system component were calculated from the measured temperature and pressure. The obtained results were summarized as follows: Under the condition of a fixed mass flow rate of the supplied fuel, TIT (turbine inlet temperature) is decreased with an increase in the LPG-N_2 mixing ratio that results in the deterioration of the overall system efficiency. As the LPG-N_2 mixing ratio is increased, NO_x emission is decreased while CO is increased that is related to the incomplete combustion occurring at the combustor. The MGT system is successful in operating at the fuel condition of heating value less than 50% of that of LPG, indicating the acceptability to such low-heating value fuels without any modification of the combustor.

Roberts et al. [13] studied the hybrid fuel cell (SOFC)/gas turbine (FC/GT) system at an atmospheric pressure. The main objective of the study was to arrive at solutions and/or control architectures for maintaining fuel cell and gas turbine inlet temperatures during severe load changes. The transient response of such system to perturbations in the power demand was investigated. Two operational strategies of gas turbines were compared: (1) fixed speed operation, and (2)

variable speed operation. For both operation strategies, a wide range of power productions were numerically simulated. The results show that variable speed operation is superior for the FC/GT hybrid configuration studied.

Chen et al. [4] brought up a novel idea that through biochemical procedures to effectively using marsh biogas and producing bio-diesel, which cooperated with hybrid generating power devices to demonstrate the promising utilization of renewable energy. One of the programs was to develop a low heating value biogas fuel power system. Based on the low heating value methane obtained from the bio-process to remove H_2S from marsh gas, it developed a micro gas turbine by modifying the burner from a liquid-fuel burning gas turbine system into a gas-burning one to generate the combustion power, used to drive a generator to produce the electricity. The CO_2 product produced from combustion reaction was conducted to bio-process to produce bio-diesel.

1.3 Scopes of the present study

The object of study is to investigate the performance of annular combustion chamber, which originally uses the liquid aviation Jet A1 as the fuel, by using the low-heating-value gaseous biomass fuel, CH_4, in a micro gas turbine of type WREN MW54. The methane gas is obtained from the purified marsh gas through bio-process. According to the present biochemical technique, there still exists a little amount of impurity gases, such as carbon dioxide (CO_2), which cannot be removed completely. It would dilute the concentration of pure methane gas such that the combustion power output is cut down. In other words, there exist two factors that make combustion power to reduce: one is the relative low heating value of methane gas, the other is the dilution effect.

The research applied commercial packaging software CFD-ACE+ to calculate the thrust generated by combustion power, and the temperature patterns of solid annular liners and combustor outlet. The above investigations

are based on the original structural configuration of combustion chamber. The varying parameter is proportion of inert gas, CO_2, in the fuel, a mixture of CO_2 and CH_4. Eventually, use the predicted results to assess whether the original combustion chamber designed for using jet A1 liquid fuel can still be applied for methane fuel. If the answer is not, then the recommendations for re-modification will be issued according to the predictions.

Chapter 2
Mathematical model

2.1 Domain descriptions

The actual micro gas turbine, WREN MW54, is illustrated in Fig.2-1 [14]. It comprises five units, which are shown in Figs. 2-2(a) ~ (d). They are the compressor, diffuser, turbine, combustion chamber and casing. A shaft is connected compressor with turbine and passed through combustion chamber, then, they are assembled between compressor and turbine. Finally, the casing is placed to cover them to accomplish the entirety.

In this study, it is interesting in the thermo-flow fields caused by combustion behaviors resulted from the oxidation of gaseous fuel, methane. Especially, the emphases are on the heat transfer of spreading flame, heat damage of solid bodies, and thrust generated from expansion of hot gases.

In order to simplify the simulation, it does not include the consideration of rotating parts, such as compressor, turbine, and shaft. However, it retains the combustion chamber and the remaining zones, including the space in between casing and outer liner, the gap between diffuser outlet and front cover of combustion chamber, which are shown in Fig. 2-5(c). This simplification is feasible as a result of the acquirable performance map of compressor shown as Fig. 2-3, which can provide enough information to confirm the air mass flow rate at specific operation point. Furthermore, through the thermodynamic formula it can calculate the air properties before it entering the combustion chamber. That is to say, the boundary conditions on the adjacent components are known. As a consequence, this study can simulate the flow field in combustion chamber, which are separated from whole the gas turbine.

The domain of combustion chamber consists of three major components. They are the solid annulus dual liners (inner and outer), which have several discharge holes, the vaporizing tube, which plays the role of fuel transportation,

and the fluids, such as gas fuel and air, filling with the remaining spaces. The annulus combustor has twelve fuel tubes and the liner holes and relative components are in a periodic arrangement shown as Fig 2-4(a), (b). Therefore, the combustor can be divided into twelve sub-chambers geometrically as shown in Fig 2-4(c), (d). Any one of twelve sub-chambers can be further divided into two similar regions based on physical symmetry. Because of this, one twenty-fourth zone out of combustor can be drawn as for computational domain. The configuration of the full-size, three dimensional model domain employed for simulation is illustrated in Fig.2-4(e). The components configuration of sub-chambers is shown as Fig. 2-5, and the size specification of sub-chamber is shown as Fig. 2-6.

2.2 Governing equations

In order to make the physical problem more tractable, several assumptions are made as follows:

1. One-twenty fourth annular zone of actual physical domain is considered due to symmetry, as shown in Fig. 2-4(e).
2. All gaseous mixtures are regarded as the ideal gases.
3. The flow is steady, compressible, and turbulent.
4. Properties in solid are constant.
5. Neglect the turbulence-combustion interaction and radiation heat transfer.
6. One step global reaction is adopted to represent the chemical reaction of methane gas combustion.
7. Soret (or thermo) diffusion, accounting for the mass diffusion resulting from temperature gradients, is neglected.[15]

Based on the assumptions mentioned above, the governing equations are given as follows [16]:

Mass conservation:

$$\nabla \bullet \left(\rho \vec{V}\right) = 0 \qquad (2\text{-}1)$$

which describes the net mass flow across the control volume's boundaries is zero.

Momentum conservation:

Based on the general Newton's second law and particular viscous stress law, the momentum equations are developed as Navier-Stokes equations:

$$\frac{\partial}{\partial x_j}\left(\rho u_j u_i - \tau_{ij}\right) = -\frac{\partial p}{\partial x_i} \qquad (2\text{-}2)$$

where suffixes i, and j represent Cartesian coordinates (i = 1,2,3), u_i and u_j are absolute fluid velocity components in directions of x_i and x_j, ρ is density, τ_{ij} is shear stress tensor component, and p is pressure.

In Newtonian fluid, the viscous stresses are proportional to the deformation rates of the fluid element. The nine viscous stress components can be related to velocity gradients to produce the following shear stress terms:

$$\tau_{ij} = 2\mu s_{ij} - \frac{2}{3}\mu \frac{\partial u_k}{\partial x_k}\delta_{ij} - \overline{-\rho u_i' u_j'} \qquad (2\text{-}3)$$

$$s_{ij} = \frac{1}{2}\left(\frac{\partial u_i}{\partial x_j} + \frac{\partial u_j}{\partial x_i}\right), \qquad (2\text{-}4)$$

where μ is the molecular dynamic fluid viscosity, δ_{ij} the 'kronecker delta', which is unity when i = j and zero otherwise, s_{ij} the rate of strain tensor.

For turbulent flow, u_i, p and other dependent variables, including τ_{ij}, assume their ensemble averaged values (equivalent to time averages for steady-state situations). Get back to Eq.(2-3), the rightmost term represents the additional Reynolds stresses due to turbulent motion. These are linked to the mean velocity field via the turbulence models. u' is fluctuation about the ensemble average velocity and the overbar denotes the ensemble averaging

process.

Energy conservation:

Heat transfer processes are computed by energy equation in the form known as the total enthalpy equation:

$$\nabla \bullet \left(\rho u_i h\right) = \nabla \bullet \left(k_{eff} \nabla T\right) + \frac{\partial}{\partial x_j}\left(u_i \tau_{ij}\right) + S_h \tag{2-5}$$

where S_h are the energy sources, h is the total enthalpy and defined as:

$$h = i + \frac{p}{\rho} + \frac{1}{2}\left(u^2 + v^2 + w^2\right) \tag{2-6}$$

where i is internal energy. k_{eff} is the effective thermal conductivity of the material. In laminar flow, this will be the thermal conductivity of the fluid, k; In turbulent flow,

$$k_{eff} = k + \frac{\mu_t C_p}{\mathrm{Pr}_t} \tag{2-7}$$

where Pr_t is the turbulent Prandtl number.

Species conservation:

$$\frac{\partial}{\partial x_j}\left(\rho u_j Y_i\right) = \frac{\partial}{\partial x_j}\left(\rho D_i \frac{\partial Y_i}{\partial x_j}\right) + M_i \omega_i \tag{2-8}$$

where Y_i represents mass fraction for mixture gas of CH_4, O_2, CO_2, H_2O and inert N_2. The term $M_i \omega_i$ is mass production rate of species. M_i is the molecular weight of i-th species. ω is global one-step reaction rate and in the Arrhenius form for methane combustion is computed as (Bui-Pham 1992) [17]:

$$\omega = k_r Y_{CH_4} Y_{O_2} \tag{2-9}$$

where k is the reaction rate constant for methane combustion reaction:

$$CH_4 + 2O_2 \rightarrow CO_2 + 2H_2O \tag{2-10}$$

and can be written in the Arrhenius form:

$$k_r = BT^{\alpha} \exp\left(-Ea/RT\right) \tag{2-11}$$

the rate constants that pre-exponential factor B, temperature exponent α, and

activation temperature Ea/R are tabulated in Table 2-1.

The equation of state for ideal gas is used to close these conservation sets:

$$\frac{P}{\rho} = R_u T \sum_{i=1}^{N} \frac{Y_i}{M_i} \tag{2-12}$$

the above equation is rewritten to express ρ as

$$\rho = \frac{P}{R_u T \sum_{i=1}^{N} \frac{Y_i}{M_i}} \tag{2-13}$$

The gas properties μ, k, C_p, D are calculated by particular law as the following:

The dynamic viscosity for each species is calculated using Sutherland's law [18]:

$$\mu = \frac{aT^{3/2}}{(b+T)} \tag{2-14}$$

where a and b are constants, they are specific for different species. The selected values for species which we need are tabulated in Table 2-2. The mixture viscosity is then calculated using mix kinetic theory of gases:

$$\mu_{mix} = \sum_{i=1}^{N} \frac{Y_i \mu_i}{\sum_j Y_j \Phi_{ij}} \tag{2-15}$$

where Y_i, Y_j are mass fraction of species i and species j, μ_i is viscosity of species i, Φ_{ij} is dimensionless quantity, and Φ_{ij} is given by:

$$\Phi_{ij} = \frac{1}{\sqrt{8}} \left(1 + \frac{MW_i}{MW_j}\right)^{-1/2} \left[1 + \left(\frac{\mu_i}{\mu_j}\right)^{1/2} \left(\frac{MW_j}{MW_i}\right)\right]^2 \tag{2-16}$$

where MW is molecule weight.

The mean specific heat at constant pressure, C_p, can be written as

$$C_p = \sum_{i=1}^{N} C_{p_i} Y_i \tag{2-17}$$

JANNAF thermodynamic polynomials are used to estimate the specific enthalpy,

h_i, and specific heat, C_{p_i}, for each species, [19]

$$\frac{C_{p_i}}{R} = a_{1,i} + a_{2,i}T + a_{3,i}T^2 + a_{4,i}T^3 + a_{5,i}T^4 \tag{2-18}$$

$$\frac{h_i}{RT} = a_{1,i} + \frac{a_{2,i}T}{2} + \frac{a_{3,i}T^2}{3} + \frac{a_{4,i}T^3}{4} + \frac{a_{5,i}T^4}{5} + \frac{a_6}{T} \tag{2-19}$$

The coefficients, $a_{1,i}$, $a_{2,i}$, $a_{3,i}$,$a_{4,i}$, $a_{5,i}$, and $a_{6,i}$ in Eqs.(2-18) and (2-19) can be found in Table 2-3.

Gas thermal conductivity, k, is derived from Prandtl number:

$$\mathrm{Pr} = \frac{\mu C_p}{k} \tag{2-20}$$

in this work, Pr=0.707 is selected.

The diffusion coefficient, D, is calculated by Schmidt number:

$$\mathrm{Sc} = \frac{\mu}{D} \tag{2-21}$$

in this work, Sc=0.7 is selected.

The constant properties of solid are tabulate in Table 2-4. [20]

2.2.1 Turbulent model

The Reynolds averaged Navier-Stokes simulation adopt $k-\varepsilon$ model which involves solutions of transport equations for turbulent kinetic energy and its rate of dissipation. The model adopted here is based on Launder and Spalding (1974). In the model, the turbulent viscosity is expressed as:

$$\upsilon_t = \frac{C_\mu k^2}{\varepsilon} \tag{2-22}$$

the transport equation for k and ε are,

$$\frac{\partial}{\partial x_j}\left(\rho u_j k\right) = \rho P - \rho\varepsilon + \frac{\partial}{\partial x_j}\left[\left(\mu + \frac{\mu_t}{\sigma_k}\right)\frac{\partial k}{\partial x_j}\right] \tag{2-23}$$

$$\frac{\partial}{\partial x_j}\left(\rho u_j \varepsilon\right) = C_{\varepsilon_1}\frac{\rho P\varepsilon}{k} - C_{\varepsilon_2}\frac{\rho\varepsilon^2}{k} + \frac{\partial}{\partial x_j}\left[\left(\mu + \frac{\mu_t}{\sigma_\varepsilon}\right)\frac{\partial \varepsilon}{\partial x_j}\right] \tag{2-24}$$

with the production term P defined as:

$$P = \upsilon_t \left(\frac{\partial u_i}{\partial u_j} + \frac{\partial u_j}{\partial x_i} - \frac{2}{3} \frac{\partial u_m}{\partial x_m} \delta_{ij} \right) \frac{\partial u_i}{\partial x_j} - \frac{2}{3} k \frac{\partial u_m}{\partial x_m} \qquad (2\text{-}25)$$

the five constants used in this model are:

$C_\mu = 0.09, \quad C_{\varepsilon_1} = 1.44, \quad C_{\varepsilon_2} = 1.92, \quad \sigma_k = 1.0, \quad \sigma_\varepsilon = 1.3$

the standard $k-\varepsilon$ model is a high Reynolds model and is not intended to be used in the near-wall regions where viscous effects dominate the effects of turbulence. Instead, wall functions are used in cells adjacent to walls. Adjacent to a wall the non-dimensional wall parallel velocity is obtained from

$$u^+ = y^+ \qquad u^+ \le y_\upsilon^+ \qquad (2\text{-}26)$$

$$u^+ = \frac{1}{\kappa} \ln\left(E y^+\right) \qquad y^+ > y_\upsilon^+ \qquad (2\text{-}27)$$

where:

$y^+ = y \frac{u_\tau}{\upsilon}$, $u^+ = \frac{u}{u_\tau}$ ($u_\tau = C_\mu^{1/4} k^{1/2}$ and $\kappa = 0.4$), and $E = 9.0$ for smooth walls.

2.3 Setting up the air/fuel ratio & two stage simulation procedures

Under maintaining the original configuration of combustion chamber geometry, it is advisable to reset the default value of the original air/fuel ratio designed for Jet-A1 fuel to let methane gas (low heating-value fuel) be able to generate more appropriate thrust. From the view point of thermodynamics, under the same supply volume of air it is necessary to provide more methane gas to produce the same thrust as that of Jet-A1 fuel.

The related literature mentioned that liner gas holes distribute over three zones, and that is similar to the very substantial turbine engine. Among the three zones, the holes in the primary zone provide air jet to mix well with fuel to result in combustion reaction.

From the above discussion, it can apply the proper amount of air via the gas holes in the primary zone to achieve the stoichiometric air/fuel ratio under the

specified consumption of methane gas. The purpose of arrangement is to prevent from fuel-lean condition causing poor thrust or fuel-rich one causing incomplete burning and overheating in downstream. Therefore, this work divides the simulation procedure into 2 stages. They are described as follows:

1. **Non-combustion stage－fuel tube without exhausting methane gas**

When the air flow coming from compressor enters annular combustion chamber, part of air stream flows into the gas holes of inner/outer liners at the primary zone. To sum up the amount of air flow per unit of time into the primary zone, then the required consumption rate of methane gas can be calculated based on stoichiometry.

2. **Combustion stage－fuel tube with exhausting methane gas**

Following the first stage, it proceeds to maintain all of the boundary conditions except that now the fuel tube is exhausting methane gas with the stoichiometric rate mentioned previously. After that, a series of parametric studies is carried out by changing the methane ratio in the fuel. That is, different amount of CO_2 gas is mixed with methane under fixed output of the mass flow rate (same as 100% methane) for total fuels.

Although these two stages seem different, their governing equations should be the same except that the extra species conservation equations and the additional heat source term due to combustion need to be included in the combustion stage.

2.4 Boundary conditions

The setting of boundary conditions are specific within the operating range of components, the setting is confirmed by means of the size specification through the classically thermodynamic theory. There are different boundary values corresponding to different operating conditions.

In the model domain, there exist boundary conditions as the following: two

inlets, one outlet, two physical symmetric surfaces (including one cyclic symmetric surface), interfaces between two different phases, solid and gas, and the remaining wall boundary conditions. The related configuration of boundaries is shown as Fig. 2-7.

What follows give an example involved with the calculation methods and steps for setting of boundary conditions.

Operating conditions:

The compressor wheel works at the rotational speed 155000 rpm, compression ratio 2.35.

2.4.1 The inlet boundary conditions

There are two inlet boundaries. One supply compressed air from the end of diffuser, and the other one supply mixed fuel gas.

1. Air inlet boundary conditions of combustor

The boundary conditions here are demand for temperature, velocity, turbulent kinetic energy, turbulent dissipation rate, and species mass fraction.

Step1. Modified compression ratio:

The user manual of micro gas turbine MW54 account for the compression ratio of compressor produced by Garrett is needed to be modified when it is assembled on this engine type. The empirical formula of modified compression ratio is

$$\pi_{\text{mod.}} = \sqrt{\pi} \quad , \quad \pi = compression\ ratio \equiv \frac{Outlet\ \ pressure\ of\ \ the\ compressor}{Inlet\ \ pressure\ of\ \ the\ compressor} \qquad (2\text{-}28)$$

$$\Rightarrow \pi_{\text{mod.}} = \sqrt{2.35} = 1.533$$

Step2. Look up the corresponding values for mass flow rates $\dot{m}$ and compression efficiency η at the specified operating conditions on compressor map for rotational speed 155000 rpm, compression ratio 2.35.

$$\Rightarrow \eta = 0.7$$

$$\dot{m} = 0.166\,(kg/s)$$

Step3. Decide the temperature rise after compressing process:

Assume the ideal air gas compression process for compressor is isentropic and adiabatic, the temperature rise could be calculated through the thermodynamics formula as follows

$$\frac{\Delta h_{ideal}^{1\to 2}}{\eta} = \Delta h_{actual}^{1\to 2} = C_p \Delta T_{actual}^{1\to 2}$$

$$\Rightarrow \Delta T_{actual}^{1\to 2} = \frac{\Delta h_{ideal}^{1\to 2}}{C_p \cdot \eta} = \frac{T_1}{\eta}\left[\left(\frac{P_2}{P_1}\right)^{0.286} - 1\right] \qquad (2\text{-}29)$$

where 1 *represents the state at compressor inlet*

2 *represents the state at compressor outlet*

$$\Rightarrow T_1 = 298K$$

$$\Delta T_{actual}^{1\to 2} = \frac{298}{0.7}\left(1.533^{0.286} - 1\right) = 55.3$$

$$\therefore\ T_2 = 353.3K$$

Step4. Calculate the air flow speed at compressor outlet:

According to state equation and continuity equation, the air flow velocity for outlet of compressor is derived as

$$P_2 = \pi_{\text{mod.}} \cdot P_1 = \rho R_u T \qquad (2\text{-}30)$$

$$\Rightarrow 1.533 \times 101.325kPa = \rho \times \frac{8.314}{28.8} \times 353.3\ ,\ \rho = 1.523\left(\frac{kg}{m^3}\right)$$

$$\dot{m}_{air} = \rho V A\ ,\ \textit{where } A \textit{ is the outlet cross-section of compressor} \qquad (2\text{-}31)$$

$$\Rightarrow 0.166\left(\frac{kg}{s}\right) = 1.523\left(\frac{kg}{m^3}\right) \times V \times 1545.66\left(mm^2\right)\ ,\ V = 70.52\left(\frac{m}{s}\right)$$

Step5. Decide turbulent kinetic energy and dissipation rate

Set turbulence intensity by empirical formula [16]:

$$I = 0.16\,\mathrm{Re}^{-\frac{1}{8}} \qquad (2\text{-}32)$$

$$\Rightarrow \mathrm{Re} = \frac{\rho V D_h}{\mu} = \frac{1.523\left(\frac{kg}{m^3}\right) \times 70.52\left(\frac{m}{s}\right) \times 12(mm)}{0.000018(kg/s \cdot m)} = 71601(turbulent\ \ flow)$$

where D_h is the hydraulic diameter of compressor outlet

$\Rightarrow I = 0.04$

Set dissipation rate in terms of hydraulic diameter:

$\Rightarrow D_h = 12(\mathrm{mm})$

Step6. Set species compositions and mass fraction of air at compressor outlet

Mass fraction: $N_2 = 0.768$, $O_2 = 0.232$

2. Fuel inlet boundary conditions of combustor

When the second stage simulation proceed, the fuel is injected. The boundary conditions here are demanded for temperature, mass flow rate, turbulent kinetic energy, turbulent dissipation rate, and species mass fraction.

Step1. Decide the fuel mass flow rate counting on the air/fuel ratio of stoichiometry.

$$CH_4 + 2O_2 \rightarrow CO_2 + 2H_2O$$

$$1:2 = \frac{\dot{m}_{CH_4}}{16} : \frac{\dot{m}_{O_2}}{32}$$

where $\dot{m}_{O_2} = 0.23\dot{m}_{air}$

$\therefore \dot{m}_{CH_4} = 0.0575\dot{m}_{air}$

For the domain that one part of 24 dividing zones. Total air mass flow rate of liner holes at the primary zone is

$\dot{m}_{air}^{primary} = 0.00123\,(kg/s)$

then $\dot{m}_{CH_4} = 7.08E-05\,(kg/s)$

Step2. Set species compositions of mixed fuel at fuel tube inlet

Set variously different ratio CO_2 gas mixed with methane. For example, volume

percentage as 80% methane, 20% CO_2 possess mixed molecular weight:

$$80\% \times 16 + 20\% \times 44 = 12.8 + 8.8 = 21.6$$

$$\therefore mass\ \ fraction\ of\ \ CH_4 = \frac{12.8}{21.6} = 0.593$$

$$mass\ \ fraction\ of\ \ CO_2 = 0.407$$

The different concentration percentage of mixed fuel are listed in Table 2-5 where is provided six suits (100%~50%) corresponding species mass fraction for parameter studying.

Step3. Set boundary temperature $T_{ambient} = 298K$

Step4. Set turbulence intensity $I = 0.04$, dissipation rate in terms of hydraulic diameter $D_h = 0.001\,(\text{mm})$.

Because the practical operating conditions of the compressor could afford range from critical rotating speed 155000 rpm to idle 45000 rpm according to compressor map, in addition to implement the case of operating condition 155000 rpm to simulate, the study provides the other three operating conditions of rpm 12000, 80000, and 45000 to simulate. All the air inlet boundary conditions and fuel inlet boundary conditions are summarized in Table 2-6, 2-7.

2.4.2 The outlet boundary conditions

The only one outlet locates the rear of combustor chamber which function is to exhaust the hot gas to generate thrust power. The outlet conditions of combustion chamber mainly determined by what is happening upstream. The pressure at outlet boundary is defined as casing pressure P_2 which derived from Eq. (2-30). The parameters such as temperature, velocity, pressure, at outlet boundary are assumed zero gradients, and the flow rate in outlet boundary must satisfy with mass balance.

2.4.3 The symmetry boundary conditions

The component of velocity vector which perpendicular to symmetric surfaces are set zero.

2.4.4 The interface boundary conditions

The interfaces between two different phases, solid and gas, are the no-slip boundary conditions (u, v, w = 0) for velocity.

2.4.5 Wall boundary conditions

Except the inlet, outlet, symmetry, and interface boundaries, the remaining geometry is all wall boundaries, which are the no-slip boundary conditions (u, v, w = 0) for velocity and adiabatic for temperature.

Chapter 3
Introduction to Numerical Algorithm

3.1 Introduction to CFD-ACE+ software

To solve the mathematical model described in Chapter two, this work uses a commercial package software, CFD-ACE+, to carry out the numerical computation. CFD-ACE+ is an Advanced CFD and Multiphysics software for simulations of fluid, thermal, chemical, biological, electrical and mechanical phenomena [21]. The solver, based on a finite-volume method [22], divides the physical domain into many control volumes invoked by computational grids and then discretizs differential equation into algebraic one for numerical computation on each grid. [23, 24]

3.2 Numerical method for CFD-ACE+

The CFD-ACE+ employs the finite-volume method to discretize the partial differential equations and then utilize SIMPLEC scheme to obtain the pressure and velocity fields by solving mass and momentum conservation equations. Then, substitute the obtained pressure and velocity fields into energy, species equations, etc. in sequence.

3.2.1 Finite-volume method

The transport conservation equations illustrated from chapter two can be summarized by four terms which are the unsteady, the convection, the diffusion, and the source terms, respectively, in a general differential equation as the following:

$$\frac{\partial(\rho\phi)}{\partial t} + \nabla\cdot\left(\rho\vec{U}\phi\right) = \nabla\cdot\left(\Gamma\nabla\phi\right) + S \qquad (3\text{-}1)$$

where ϕ is a general variable to be solved, ρ the density, $\vec{U}$ the velocity vector, Γ the diffusion coefficient, and S a source term which includes all

terms that can't be included in the previous terms.[23]

With two dimensional consideration, to discretize Eq. (3-1), it uses finite-volume method to divide the physical domain into many control volumes as shown in Fig. 3-1(a). From which the shadow area is one of the control volumes. P is the center point of a control volume. E,W,N,S are the center points of neighboring control volumes, respectively.

Take volume integrals to Eq. (3-1) for the shadow area, it can get

$$\frac{\partial}{\partial t}\int_{\forall}\rho\phi d\forall+\int_{A}\rho\phi\vec{U}\cdot d\vec{A}=\int_{A}\Gamma\nabla\phi\cdot d\vec{A}+\int_{\forall}S_{\phi}d\forall \tag{3-2}$$

where $\forall$ represents the volume, A represents each surface of the control volume P. Furthermore, applying the symbols in Fig. 3-1(a), it becomes

$$\frac{\partial}{\partial t}\int_{s}^{n}\int_{w}^{e}\rho\phi dxdy+\int_{s}^{n}\int_{w}^{e}\rho\phi\vec{U}\cdot dxdy=\int_{s}^{n}\int_{w}^{e}\Gamma\nabla\phi\cdot dxdy+\int_{s}^{n}\int_{w}^{e}S_{\phi}dxdy \tag{3-3}$$

where e,w,n,s are the interfaces of both P control volume and neighboring control volumes. Then, use the difference scheme (e.g. upwind scheme or central difference scheme) to discretize each terms of Eq.(3-3) into finite difference equations. Via arrangement, the finite difference equation can be written as the form of [23, 24]

$$a_P\phi_P=a_E\phi_E+a_W\phi_W+a_N\phi_N+a_S\phi_S+b \tag{3-4}$$

where a_P,a_E,a_W,a_N,a_S are the coefficients of general variables $\phi_P,\phi_E,\phi_W,\phi_N,\phi_S$. b is a coefficient part drawn from S_{ϕ}, the other part of S_{ϕ} is merged into a_P. Thus, general variables can be obtained through the iteration calculation from Eq.(3-4).

The integral conservation equation (3-2) is applied to each control volume, as well as to the solution domain as a whole. To sum up the equations for all control volumes, it can obtain the global conservation equation, since the surface integrals over inner control volume faces cancel out each other. Thus global

conservation is built into the method and this provides one of its principal advantages.[24]

3.2.2 SIMPLEC scheme

SIMPLEC stands for “Semi-Implicit Method for Pressure-Linked Equations Consistent” and is an enhancement to the well known SIMPLE algorithm. In SIMPLEC, originally proposed by Van Doormal and Raithby [22], an equation for pressure-correction is derived from the continuity equation. It is inherently an iterative method.

The staggered grids shown in Figs. 3-1(a) and (b), the difference equation derived from x-direction momentum equation for the e interface is

$$a_e u_e = \sum a_{nb} u_{nb} + b_e + A_e (P_P - P_E) \tag{3-5}$$

where P is pressure, A_e is the e interface area on which the control volume possessed center point p. The subscribe nb represents the grids surrounding with position e. It needs to provide pressure field to solve velocity u. It begins with a guessed pressure value P^* to solve this equation, then get a response of velocity value u^* to satisfy

$$a_e u_e^* = \sum a_{nb} u_{nb}^* + b_e + A_e (P_P^* - P_E^*) \tag{3-6}$$

usually, u^* does not satisfy the continuity equation. The stratagem of SIMPLEC scheme is to find the correction values for u^* and P^* to get their improved values. Now, represent the correction velocity u' and correction pressure P' as follows:

$$u = u^* + u' \tag{3-7}$$

$$P = P^* + P' \tag{3-8}$$

Subtracting Eq.(3-6) from Eq.(3-5) can obtain a relation between u' and P', that is

$$a_e u_e' = \sum a_{nb} u_{nb}' + A_e (P_P' - P_E') \tag{3-9}$$

Subtract $\sum a_{nb} u_e'$ from both side of equal sign in Eq.(3-9), then

$$(a_e - \sum a_{nb})u_e^{'} = \sum a_{nb}(u_{nb}^{'} - u_e^{'}) + A_e(P_P^{'} - P_E^{'}) \tag{3-10}$$

Let $u_{nb}^{'}$ approximate to $u_e^{'}$, and then substitute $u^{'} = u - u^{*}$ into Eq.(3-10)

$$u_e = u_e^{*} + d_e(P_P^{'} - P_E^{'}) \tag{3-11}$$

where

$$d_e = \frac{A_e}{a_e - \sum a_{nb}} \tag{3-12}$$

The control volume shown by Fig.3-1(a) at steady state leads the continuity equation to the form as

$$(\rho uA)_w - (\rho uA)_e - (\rho uA)_s - (\rho uA)_n = 0 \tag{3-13}$$

Substitute u_w, u_e, u_s, u_n derived from Eq.(3-11) into Eq.(3-13), it can get

$$a_P P_P^{'} = a_E P_E^{'} + a_W P_W^{'} + a_N P_N^{'} + a_S P_S^{'} + b \tag{3-14}$$

where

$$a_E = (\rho Ad)_e \tag{3-15}$$

$$a_W = (\rho Ad)_w$$

$$a_N = (\rho Ad)_n$$

$$a_S = (\rho Ad)_s$$

$$a_P = a_E + a_W + a_N + a_S \tag{3-16}$$

$$b = (\rho u^{*}A)_w - (\rho u^{*}A)_e - (\rho v^{*}A)_s - (\rho v^{*}A)_n \tag{3-17}$$

The sequence of operation for SIMPLEC scheme is summarized as follows

1. Guess the pressure field P^{*}.
2. Solve the discretized momentum equations, such as Eq.(3-6), to obtain u^{*}, v^{*}, w^{*}.
3. Solve b of Eq. (3-17) and then $P^{'}$ of Eq.(3-14).
4. Calculate P from Eq. (3-8).
5. Calculate u, v, w from their starred values using the velocity-correction formula

in Eq.(3-11).

6. Solve the discretization equation for other ϕ's (such as temperature, concentration, and so on), if they influence the flow field through fluid properties, source terms, etc.
7. Treat the corrected pressure P as a new guessed pressure P^*, return to step 2, and repeat the whole procedure until a converged solution is obtained.

3.3 Computational procedure of simulation

The complete operating procedure for using CFD-ACE+ package software is carried out through three processes in sequence.

Firstly, import the computational model of 1/24 zone of combustion chamber to pre-processing software CFD-CADalyzer, which is the computational grid generator for computational model. This work adopts unstructured tetrahedral grid because of the complicated geometry structure of combustion chamber. The pattern and distribution of grids generated for combustion chamber is shown in Fig 3-2.

Secondly, import the computational domain which possesses grids to solver software CFD-ACE-GUI, used to set the model options, the properties of fluid and solid, boundary conditions, and the numerical methods. Then, execute numerical calculation with these data and commands.

Thirdly, import the resultant .DTF file solved by CFD-ACE-GUI to post-processing software CFD-VIEW, which is used to visualize and analyze the results. It can present the visible flow field and draw out the required data.

The flowchart of solution procedure for combustion flow field is shown in Fig 3-3. It illustrates that utilize SIMPLEC scheme to start iterative computation, which first solve the pressure and velocity fields, and then solve the temperature, concentration, turbulence energy, and turbulence dissipation rate, in sequence.

3.4 Grid-independence test

For obtaining the acceptable numerical solution, this work applies the unstructured grids produced from geometry models to carry out grid-independence test. The grid-independence tests include both cold flow and combustion cases.

Because the over-heating problem of liners is one of concerns in this research, the grid densities is increased especially near the liners, whose thicknesses are only 0.4mm and the vaporizing tube, which is about 0.3mm in thickness. Owing to adoption of upwind numerical difference scheme, the grid amount should be dense enough to avoid the false diffusion phenomenon.

For stage1: **Cold flow case**

The operating conditions are that the air inflow is generated by compressor, with a compression ratio of 2.35, under a rotation rate 155,000 rpm.

The purpose for simulating the cold-flow condition is to obtain the amount of air flow in primary zone. Thus the total flow amount through the liner holes of the primary zone is the major concern.

Two different grid distributions (densities) are tested: One is the grid number of 446097, the other is 525165. The test results are given in Table 3-1, in which the locations of face1 to face5 are illustrated schematically in Fig. 3-4. From this table, it can be seen that the maximum relative error among these holes in primary zone is less than 2%, even the relative error of the sum of total amount of air flows through these holes is less than 0.6%. To negotiate with the computational time, the grid number of 446097 is adopted in this cold flow case.

Table 3-1 Grid test results of different grid densities for cold flow case

Mass Flow Rate (kg/s)	446097grids	525165grids	Relative Error (%)
face1	3.13E-04	3.18E-04	1.53
face2	3.84E-04	3.85E-04	0.23
face3	2.21E-04	2.17E-04	1.84
face4	1.54E-04	1.56E-04	1.15
face5	1.58E-04	1.61E-04	1.98
Summation	1.23E-03	1.24E-03	0.57

For stage2: **combustion case**

The operating conditions are that the air inflow of v=70.52m/s is generated by compressor with a compression ratio 2.35 under the rotation rate 155000 rpm, and the fuel tube supplies a mixing fuel of methane (mass fraction 0.8) and CO_2 (mass fraction 0.2) under a fixed mass flow rate (m=7.08E-05kg/s).

There are two major concerns for the combustion case, and they are as follows:

1) To obtain the thrust of high temperature gases expanded after combustion reaction.
2) To obtain the maximum allowable temperature that may cause the heat damage on turbine blades.

From the above discussion, the mass flow rate, velocity and temperature of gas mixture ejecting from the rear of combustion chamber are the emphasized data.

The grid numbers adopted for the grid-independence tests in this case are the same as the ones in cold flow case (446097and 525165). The test results are listed in Table 3-2, in which the area of illustrated data is shown in Fig 3-5. From the information given by the table, it can be seen that the maximum

relative errors of various physical quantities are all less than 2%. Under such circumstance, it is naturally to select the grid number of 446097 to compromise the computational time.

Table 3-2 Grid test results of different grid densities for combustion case

	446097grids	525165grids	Relative Error (%)
Outlet mass flow rates (kg/s)	7.04E-03	7.02E-03	0.28
Outlet max. temperature (K)	788.7	794.7	0.76
Outlet max. velocity (z-direction) (m/s)	192.4	188.7	1.96
Average outlet velocity (z-direction) (m/s)	149.4	146.7	1.84

Apply PC of Pentium 4 with CPU 3.0 GHz, 2GB RAM to carry out the computation, and select convergence criterion as 10^{-4}. Then the computational time for a typical simulation in the cold flow case needs about 12 hours, whereas it spend about 100 hours for a combustion simulation.

Chapter 4
Results and Discussion

4-1 Cold flow case

The cold flow cases are carried out in the first stage simulation interpreted in section 2.3. The main object is to obtain air mass flow rates on primary zone to calculate fuel consumption. Moreover, flow rates data of each liner hole are recorded in this stage, which provides information for discharge coefficients calculation and reference for modifying liner holes.

There are four cases of cold flow simulation with different inlet air flow conditions, which are at turbine rotational speed at 155000, 120000, 80000, and 45000 rpm, respectively. The resultant air mass flow rates for the five liner holes in primary zone for each rotational speed are listed in Table 4-1. The assigned face numbers (face1- face5) were defined previously in Fig. 3-4. The corresponding flow rates of the five specific liner holes are also illustrated in Fig. 4-1. From Table 4-1, it can be seen apparently that the total air mass flow rate of primary zone decrease with the reduction of turbine rotational speed. Figure 4-1 also shows that the respective flow rates for the five specific liner holes have the same descending trend as the total air mass flow rates. In addition, the individual four lines strung across five flow rates of specific liner holes are not intersected, which represents each air flow rate decreases with the reduction of compressor rpm for same hole. Among all four cases, face2 have the maximum flow rate. The flow rates distribution of remaining liner holes (face6 ~ face11) are listed in Table 4-3. The assigned face numbers (face1- face11) are defined in Fig. 4-2.

The other interesting issue is whether the ratios of the total flow rate of primary zone to that of the engine in the four cold flow cases are the same or not. The results are shown in Table 4-2, which indicates the ratios being convergent to a value of 0.178 approximately with four different air inlet conditions. This

phenomenon implies that the total air flow rate is distributed with fixed proportion to the primary, intermediate and dilution zones that maintains their functions.

4-2 Combustion case

In the combustion cases, the same four air inlet flow rates are considered. The corresponding calculated fuel of inlet flow rates can be divided into six mass-fraction conditions, that is, the highest one is 100 percent of methane and the lowest is 50 percent. The inlet fuel flow rate of 100 percentage methane is obtained by stoichiometric calculation. The other concentration of fuel is a mixture of carbon dioxide (CO_2) and pure methane (CH_4). The simulation results are listed in Table 4-4 (a) ~ (d).

The simulation results of thrust generated by combustion energy are also exhibited in Fig. 4-3. The figure shows that the thrust decreases with the reductions of the methane mass fraction and the air flow rate (i.e. turbine rotational speed). The variation of thrust caused by the increase of methane mass fraction is larger in 155000 rpm case than that in 45000 rpm case. This phenomenon can be derived from average outlet mass flow rate and average outlet velocity. Both data are tabulated in Table 4-4 (a) ~ (d). These two sets of data are extracted to depict Figs. 4-4 and 4-5. They illustrate that the average outlet velocity increases with an increase of methane mass fraction, however, the outlet mass flow rate does not. The above information indicates that mass conservation is established firmly, and with an increase of methane fraction at higher air flow rate the gas expansion effect is more severe which causes the higher variation and value of average outlet velocity.

Table 4-4 and Fig. 4-3 show that the maximum thrust generated by methane

fuel is 32N. However, the thrust is calculated from combustion outlet. It's different from the real thrust calculated from nozzle outlet; hence, we can't compare the data with the engine instruction manual demonstrating that the maximum thrust generated by Jet A1 fuel is 54N.

The results of the maximum temperatures on liner walls are listed in Table 4-4 and depicted in Fig. 4-6 as well. It is critical if the combustor wall, made of stainless 316, has the capability to tolerate the heat. The maximum temperature allowance is about $900\,°C$ (=1173K); therefore, most liners under the simulation conditions, which are above the red dotted line in Fig. 4-6, should be burned out. The simulation results of liner temperature distribution in the case of 155000 rpm under different mass percentages of methane are shown from Figs. 4-7 (a) to 4-7 (f). These figures demonstrate that the overheat points are located at the outer liners. The high temperature areas on outer liners are bigger and bigger with methane mass fraction increasing; moreover, the most high temperature values gradually move toward intermediate zone of outer liners with methane mass fraction increasing. The phenomenon of overheat is unreasonable since the heating value of methane is lower than that of Jet Al and the original combustor design for Jet A1 fuel will not cause the heat damage to liners. The possible reasons are explained as follows: (1) The simulation lacks appropriate data for physical properties of solid stainless steel 316. Both thermal conductivity and specific heat employed in the simulation for solid liner are measured at low temperature and they are listed in Table 2-4. However, for the high critical temperature as $900\,°C$, these parameters are uncertained. Based on the thermodynamics, $\Delta H \approx C_p \Delta T$, and the heat conduction theory, $\ddot{q} = k\Delta T = h_{coef.}\Delta T$, the increase of specific heat C_p and heat conduction will result in a decrease of ΔT when the heat flux and enthalpy variation are fixed. That is to say that it decreases the temperature rise from cold flow case to combustion one on liners. C_p and k rise with the increase of temperature. Hence, here using of the

smaller data would cause liners temperature to be over predicted. (2) The simulation employs fixed constant setting of turbulent Prandtl and Schmidt numbers at everywhere in combustor. The turbulent Prandtl and Schmidt numbers are set to 0.7 for the CFD model. This relatively low value may agree with the condition as combustor is in fuel-air mixing circumstance. However, the relative lower value results in an increment of heat transfer rate compared to that using the higher value. Since the convective heat transfer rate is increased on both sides of the liner, the effect on the wall temperature is relatively small. The temperature gradient through the wall, however, is over predicted. [10] (3) The internal flow fields are changed by methane gas. The process of transportation and consumption for original liquid fuel Jet A1 is stated as follows: The liquid fuel Jet A1 absorbs latent heat of vaporization when it pass through the vaporizing tube. In the meantime, the liquid Jet A1 fuel gradually transfers to gas fuel. Continuously, the gas fuel combines with oxygen of air to start combustion reaction. Comparing methane gas with Jet A1 liquid fuel, it is single phase in process of transportation. In addition, its' energy density is smaller than Jet A1, which makes flow rate increase to supply fuel consumption. These changes can cause the flow fields very different.

The high temperature distributions on solid liner walls are induced by heat transfer of combustion flow; hence, the flow field in between the annulus outer liner and inner liner walls are considerable information. Here exhibits combustion flow field by means of physical quantities value and color distinction on cross-section of combustor for combustion case 155000 rpm. The flow field is analyzed by two selected cross-sections; one locates symmetric face (0 degree cross-section), the other locates included angle 7.5 degrees measured from datum symmetric face illustrated as Fig. 4-8, 9. Both cross-sections show that distributions of CH_4 mass fraction, O_2 mass fraction, temperature, and velocity vector.

For symmetric face (0 degree cross-section) which passes through two liner holes. Fig. 4-10 (a) ~ (f) show that the CH_4 mass fractions in primary zone increase with methane concentration rising; moreover, larger CH_4 mass fraction produce much more severe reaction at interface between zero methane mass fraction and mass diffusion zone of methane concentration gradient. Fig. 4-11 (a) ~ (f) show that the distribution range of zero O_2 mass fraction in primary zone increase with methane concentration rising; inversely, the distribution range of higher O_2 mass fraction are decrease with methane concentration rising. In addition, the jets flow core discharged from two liner holes possess the almost highest O_2 mass fraction 0.232 because they come from fresh air. Fig. 4-12 (a) ~ (f) show that the spaces which are occupied by high temperature increase with methane concentration rising. From the color distinction of temperature distributions for different six methane concentrations, each reveals that high temperature extend to outer liner wall, which may cause heat damage. For each picture, the front outline of high temperature flame presented with red approximately match together with outline of mass diffusion zone shown as Fig. 4-10 (a) ~ (f). Fig. 4-13 (a) ~ (f) show that the combustor outlet velocity magnitude increase with methane mass fraction rising. In addition, the distributions of exhausting velocity at outlet are not uniform. The distributions of velocity vector inside combustor are complicated as a result of mutual influence of jets flow discharged from liner holes. The flow paths and directions in between outer liner wall and vaporizing tube roughly induced toward the outer liner wall.

For 7.5 degrees cross-section which passes through five liner holes. Fig. 4-14 show that the same trend as symmetric face (0 degree cross-section); however, the situation of methane mass fraction distributions are different because the flow structure in this site are different. Figure 4-15 (a) ~ (f) illustrate O_2 mass fraction. Figure 4-16 (a) ~ (f) show that different temperature

distributions from Fig. 4-12 (a) ~ (f), which elucidates different mix extent and intensity of air and methane. Figure 4-17 (a) ~ (f) show the same trend of combustor outlet velocity magnitude as Fig. 4-13 (a) ~ (f); however, the direction of outlet velocity vector are different, for symmetric face is toward northeast, for 7.5 degrees cross-section is toward southeast. In addition, a few vortices are discovered inside combustor. They result from jets flow mutual influence.

The temperature distribution in depth of outer liner result from the heat transfer among three zones: combustion gas flow, air flow comes from compressor, and solid outer liner in between. Here, we illustrate the radial temperature distribution for case 155000 rpm with 100% methane by line probe which pass through above-mentioned three zones. The temperature distribution on line probe and corresponding position are shown as Fig. 4-18. The line probe is on symmetric face. Its' end points are wall edge of vaporizing tube and half depth of outer annual flow channel. From this figure, we can see that the liner temperature gradient across liner is small (outer liner, 1301K; inner liner 1320K) because the liner thickness is thin (0.4mm). However, it shows that the two side flows adjacent outer liner wall have sharp temperature gradients because of the relative poor heat transfer effects to solid liner.

The combustor outlet, which is next to turbine, emits high temperature gas. The critical endurance temperature of turbine blade is about $700°C$ (=973K). Figure 4-19 shows the simulation results of maximum temperature in combustor outlet. Each case expresses the same trend that the outlet temperature will raise with the increase of methane mass fraction. When 100% methane fuel is employed, all predictions exceed the maximum temperature that the turbine wheel can tolerate, and they should damage the turbine blade. The results show that, among 24 simulation conditions, the heat damages to turbine blade are less than those to liners. One of the reasons is that outlet is away from the solid zone

of liners and then it suffers less over-heating problem as mentioned maximum previously. The other one is that the cool air flows via dilution holes on liners are fully functional. The jet flow discharged from dilution holes cool down the exhaust gas temperature effectively. The average exhaust temperature of combustor outlet is showed out on Fig. 4-20. All data are below the endurance temperature $700\,^{\circ}C$, the results contrast with Fig. 4-19 explain that turbine blades would incur heat damage locally not totally in case of methane mass fraction unity.

The CO_2 gas emitted from combustor would cause the environmental pollution. Recently, the ideas for recycling or absorbing CO_2 through bio-chemical procedures are feasible. The data of average outlet CO_2 and H_2O mass flow rates are both listed in Tables 4-4 for future reference. Figures 4-21 and 4-22 show the similar trends that with the increase of methane mass fraction, CO_2 and H_2O mass flow rates rise. These results are apparently as expected. In addition, for an example, the case of 155000 rpm with 100% of methane, the value of CO_2 mass flow rate (2.11E-04) is bigger than H_2O (1.73E-04). Based on Eq. (2-10), $CH_4 + 2O_2 \rightarrow 2H_2O + CO_2$, the stoichiometric relation is clear that confirms the output results.

The other physical quantities, maximum reaction rates, are also given in Table 4-4 (a) ~ (d). It is govern by Arrhenius reaction rate law as shown by Eqs. (2-9) and (2-11). From Eq. (2-9), it interprets that reaction rate is affected by methane and oxygen concentrations. When one of them increases, reaction rate rises. The simulation results complies with the rule when methane mass fraction increases, representing that reaction rate rises at the interface of methane and air.

From Table 4-4 (a) ~ (d), all the data of maximum temperature in combustor are shown above 2000K. The results can be conformed by the reference, which states that temperature above this value can generate stable flame [6]. However, this software does not have the built-in program to

demonstrate the flammability limits in air. The flammability limits in air at 1atm & 298K for weak mixture of methane is at the equivalence ratio equal to 0.53 [6]. In this study, stoichiometric calculation of methane air/fuel ratio is 0.0575. Hence, when air/fuel ratio is below 0.03 (=0.53*0.0575), it is hard to fire for combustion. Based on this viewpoint, the cases of methane concentration 60% and 50% are fail to generate combustion because their low methane mass fractions as shown in Table 2-5. Nevertheless, the qualitative analysis for different methane concentrations is still worthy.

The mass fractions of combustion product, H_2O, accompanying with combustion reaction at 155000 rpm case are shown in Figs. 4-23 (a) ~ (f). The existence of H_2O illustrates that combustion reaction is under developing. The legend of color bar in the figures shows the H_2O mass fraction distributions in combustor. The high concentrations of H_2O are mainly located at primary to intermediate zones, which represents the vigorous combustion with high temperature. At the rear of combustor, it shows the lower H_2O mass fraction because it is diluted by air from dilution holes.

By means of the merit of flow visible properties of CFD, the case 155000 rpm with pure methane fuel is selected to illustrate the inner flow field of combustor. Figure 4-24 shows the temperature distributions of combustor in several cross-sections. From this figure, it can be seen that the jet flow discharged from liner holes (the third cross-section) reduces the heat transfer from flame to liner. Figure 4-25 shows parts of stream lines in combustor. From the stream line distributions, the recirculation in the combustor is identified, and it can enhance the mixing of fuel and air. The colors of stream lines can illustrate the velocity magnitude of flow. At the front of combustor, velocity is smaller, but at the rear it become greater due to the transform of pressure and mass continuity. Yet, these are just parts of stream lines; there are still a lot of them being left, representing the complicated flow structure.

Chapter 5
Conclusions and recommendations

The research contents are the applications of CFD simulations on low heating value methane gas fuel for the acceptability of MW54 micro gas turbine. The results are summarized as follows:

(1) The thrust is diminished again as a result of adding non-fuel substance CO_2 into pure methane fuel.

(2) The liners temperature may be estimated unreasonable because it lacks appropriate data of specific heat and heat conductivity for stainless steel liner at high temperature. In addition, fixed constant setting of turbulent Prandtl and Schmidt numbers would cause liner over heat.

(3) The function of dilution holes is maintained. Although the fuel is changed into methane gas, the hot gas exhausted from combustor outlet is cooled down by jet flow effectively.

Based on the above-mentioned conclusions and drawbacks, here some recommendations are addressed for possible solutions.

(1) Using more accurate expressions for heat conductivity and mass diffusivity for air-fuel mixing flow, like kinetic theory for heat conductivity and Stefan-Maxwell law of multi-component diffusion for mass diffusivity. Both models are developed from the viewpoint of particle motion, which is more fundamental and then make the solutions more accurate, especially for liner temperature. However, the better models cost much more calculation time for computer.

(2) Join compressor and turbine with combustor to complete the coupled fluid-solid simulation. In order to get more real physical mechanism, the coupled fluid-solid simulation should take into consideration. Moreover, adding nozzle guide vanes and nozzle to accomplish real thrust calculating, which helps comparing thrust generated by Jet A1 fuel.

(3) Improve the one step chemical reaction model to two steps. The reason to recommend two-step reaction model is that it includes the oxidation of substance CO, which is also a fuel. In many textbooks, the jet flow discharged from intermediate zone of liner is designed for recovering the dissociation losses of CO. In addition, the exhaust of CO is an issue of environment protection. Moreover, the difference of total reaction rates between one step and two steps may result in different level of heat accumulation in combustor. Thus, more phenomena can be studied by using two-step chemical reactions.

References

[1] Wilson, David Gordon, The Design of High-Efficiency Turbomachinery and Gas Turbines, Cambridge, Mass., MIT Press, 1984.

[2] Epstein, A. H. & Senturia, S. D., "Macro Power form Micro Machinery", Science, 276, pp. 1211, 1997.

[3] Carno, Johanna et al., "Micro gas turbine for combined heat and power in distributed generation", Proceedings of the 1998 International Gas Turbine & Aeroengine Congress & Exhibition, n GT, 6p, Stockholm, Sweden, American Society of Mechanical Engineers(paper), 1998.

[4] 陳俊勳等, 「低熱值生質燃料甲烷發電系統之建立」, 行政院國家科學委員會專題研究計畫, 計畫編號NSC 94-2218-E-009-032, 民國九十五年十月。

[5] Mike Murphy, Kit Assembly and Operation Manual of MW54 Gas Generator, Wren Turbines Ltd., Feb, 2005.

[6] J. Odgers and D. Kretschmer, Gas Turbine Fuels and Their Influence on Combustion, A. K. Gupta & D. G. Lilley, Turnbridge Wells, Kent & Cambridge, Mass., Abacus Press, 1986.

[7] Arthur H. Lefebvre, Gas Turbine Combustion, McGraw-Hill, New York, 1983.

[8] J. Chomiak et al., "Combustion of Low Calorific Value Gases; Problems and Prospects", Prog. Energy Combust. Sci., 15, pp.109-129, 1989.

[9] W. C. Ho et al., "An Experimental Investigation of the Combustion Characteristics of a Miniature Annual Combustor", 中華民國第五屆燃燒科技應用研討會, pp.179-185, Kaohsiung, Taiwan, March 18-19, 1995.

[10] D. S. Crocker et al., "CFD Modeling of a Gas Turbine Combustor from Compressor Exit to Turbine Inlet", Journal of Engineering for Gas Turbines and Power, 121, pp. 89-95, January 1999.

[11] Kousuke Isomura et al., "Development of Micromachine Gas Turbine for Portable Power Generation", JSME International Journal, Series B: Fluids and Thermal Engineering, V.47, N.3, pp. 459-464, Micro Mechanical Engineering, August, 2004.

[12] Daisuke Yamashita et al., “Experimental Evaluation on Low-Heating Value Fuel Acceptability of Micro Gas Turbine System Operation”, The 16th International Symposium on Transport Phenomena, ISTP-16, pp. 1-7, Prague, 2005.

[13] Rory Roberts et al., “Control Design of an Atmospheric Solid Oxide Fuel Cell/ Gas Turbine Hybrid System: Variable versus Fixed Speed Gas Turbine Operation”, Journal of Power Sources, 161, pp.484-491, 2006.

[14] http://www.wrenturbines.co.uk/product.php?pid=2

[15] Kenneth K. Kuo, Principles of Combustion, John Wiley & Sons, Canada, 1986.

[16] CFD-ACE+ V2004 Modules Manual V1, ESI group company.

[17] Bui Pham, M. N., ”Studies in Structures of Laminar Hydrocarbon Flames, Ph. D. Dissertation. University of California, San Diego, 1992.

[18] Frank M. White, Viscous Fluid Flow, 2nd ed., McGraw-Hill, Inc., 1991.

[19] Andrews J. R. and Biblarz O. “Temperature Dependence of Gas Properties in Polynomial Form”, NPS67-81-001, Naval Postgraduate School, Monterey, California, 1981.

[20] Engineering Properties of Steel, Philip D. Harvey, American Society for Metals, Metals Park, Ohio 44073, 1982.

[21] http://www.cfdrc.com/

[22] CFD-ACE+ V2004 User Manual, ESI group company.

[23] Patankar, Numerical heat transfer and fluid flow, Taylor & Francies, 1980.

[24] Ferziger & Peric, Computational methods for fluid dynamics, 3rd ed., Springer ,2002.

Table 2-1 Reaction rate constants used in one-step methane/air reduced kinetic scheme adopted form Bui-Pham (1992).

$k_r = BT^{\alpha}\exp(-Ea/RT)$		
$B[mol, cm^3, s]$	α	$E(=RT)[kJ/mol]$
5.2×10^{13}	0	123.98

Table 2-2 Sutherland's law coefficients of dynamic viscosity

	Species				
Sutherland's Law Coefficients	CH_4	O_2	CO_2	H_2O	N_2
A	1.2515E-06	1.7830E-06	1.5034E-06	1.8670E-06	1.4050E-06
B	197.4	156	222.26	708	111.5

Table 2-3 JANNAF coefficients of gas specific heat

	Species				
Temperature limits(K)	CH_4	O_2	CO_2	H_2O	N_2
lower limit	300				
break point	1000				
upper limit	5000				
Coefficients at lower limit	※ These coefficients will be used at temperatures between the lower limet and the break point				
a1	7.79E-01	3.21E+00	2.28E+00	3.39E+00	3.30E+00
a2	1.75E-02	1.13E-03	9.92E-03	3.47E-03	1.41E-03
a3	-2.78E-05	-5.76E-07	-1.04E-05	-6.35E-06	-3.96E-06
a4	3.05E-08	1.31E-09	6.87E-09	6.97E-09	5.64E-09
a5	-1.22E-11	-8.77E-13	-2.12E-12	-2.51E-12	-2.44E-12
a6	-9.83E+03	-1.01E+03	-4.84E+04	-3.02E+04	-1.02E+03
a7	1.37E+01	6.03E+00	1.02E+01	2.59E+00	3.95E+00
Coefficients at upper limit	※ These coefficients will be used at temperatures between the break point and the upper limit				
a1	1.68E+00	3.70E+00	4.45E+00	2.67E+00	2.93E+00
a2	1.02E-02	6.14E-04	3.14E-03	3.06E-03	1.49E-03
a3	-3.88E-06	-1.26E-07	-1.28E-06	-8.73E-07	-5.68E-07
a4	6.79E-10	1.78E-11	2.39E-10	1.20E-10	1.01E-10
a5	-4.50E-14	-1.14E-15	-1.67E-14	-6.39E-15	-6.75E-15
a6	-1.01E+04	-1.23E+03	-4.90E+04	-2.99E+04	-9.23E+02
a7	9.62E+00	3.19E+00	-9.55E-01	6.86E+00	5.98E+00

Table 2-4 Properties of solid liner

Material	Density(kg/m^3)	Specific heat(J/kg-K) at 0~100^{o}C	Thermal conductivity(W/m-K) at 500^{o}C
Stainless steel 316	8000	500	21.5

Table 2-5 Different concentration percentage of mixed fuel

Concentration of CH4		100 %	90 %	80 %	70 %	60 %	50%
Mass fraction	CH4	1	0.766	0.593	0.459	0.353	0.267
	CO2	0	0.234	0.407	0.541	0.647	0.733

Table 2-6 Air inlet boundary conditions of combustor

Conditions		**Parameters**				
r.p.m.	Compression ratio	V(m/s)	T_2(K)	turbulence intensity, I	hydraulic diameter(mm)	mass fraction
155000	2.35	70.52	353.33	0.04	12	N_2=0.768, O_2=0.232
120000	1.85	50.26	337.13	0.04	,,	,,
80000	1.35	38.03	316.68	0.04	,,	,,
45000	1.1	16.04	304.32	0.05	,,	,,

Table 2-7 Fuel inlet boundary conditions of combustor

Conditions		**Parameters**					
r.p.m.	Compression ratio	Total air mass flow rate at primary zone (kg/s)	fuel mass flow rate (kg/s)	T(K)	turbulence intensity, I	hydraulic diameter(mm)	mass fraction
155000	2.35	1.23E-03	7.08E-05	298	0.04	0.001	specified in Table.2-5
120000	1.85	8.15E-04	4.69E-05	,,	0.04	,,	,,
80000	1.35	5.61E-04	3.23E-05	,,	0.04	,,	,,
45000	1.1	2.23E-04	1.28E-05	,,	0.05	,,	,,

Table 4-1 Mass flow rates of liner holes at primary zone for different turbine rotational speed

	Diameter(mm)	155000 rpm	120000 rpm	80000 rpm	45000 rpm
face1	1.5	3.13E-04	2.07E-04	1.43E-04	5.66E-05
face2	2.3	3.84E-04	2.55E-04	1.75E-04	6.93E-05
face3	1.5	2.21E-04	1.47E-04	1.01E-04	4.02E-05
face4	1.7	1.54E-04	1.02E-04	7.05E-05	2.81E-05
face5	1.7	1.58E-04	1.05E-04	7.18E-05	2.83E-05
Total flow rates of		1.23E-03	8.15E-04	5.61E-04	2.23E-04
primary zone (kg/s)					

Table 4-2 Relation between total mass flow rate and total mass flow rate of primary zone

	Compression ratio	Total flow rate (kg/s)	Total flow rate (1/24) (kg/s)	Total flow rate of primary zone (1/24) (kg/s)	Ratio of total flow rate of primary zone to total flow rate(1/24)
155000 rpm	2.35	0.166	6.917E-03	1.231E-03	1.780E-01
120000 rpm	1.85	0.110	4.583E-03	8.153E-04	1.779E-01
80000 rpm	1.35	0.076	3.154E-03	5.611E-04	1.779E-01
45000 rpm	1.1	0.030	1.250E-03	2.226E-04	1.781E-01

Table 4-3 Mass flow rates of liner holes at intermediate, dilution zone for different turbine rotational speed

	Diameter(mm)	155000 rpm	120000 rpm	80000 rpm	45000 rpm
face6	3.25	1.55E-03	1.03E-03	7.08E-04	2.80E-04
face7	4.9	1.73E-03	1.15E-03	7.94E-04	3.17E-04
face8	1.5	3.50E-04	2.33E-04	1.61E-04	6.33E-05
face9	2.8	4.02E-04	2.65E-04	1.82E-04	7.19E-05
face10	4.9	1.54E-03	1.02E-03	6.99E-04	2.76E-04
face11	1.5	1.56E-04	1.03E-04	7.05E-05	2.72E-05
Summation (kg/s)		5.73E-03	3.80E-03	2.61E-03	1.04E-03

Table 4-4 (a) Simulation results for combustion case of 155000 rpm

Rotational speed = 155000 rpm (critical)						
Mass fraction of methane in fuel mixture	1	0.9	0.8	0.7	0.6	0.5
Outlet mass flow rate (kg/s)	7.054E-03	7.044E-03	7.040E-03	7.035E-03	7.018E-03	7.018E-03
Outlet maximum temperature (K)	1215	963	789	667	583	525
Outlet maximum speed (z direction) (m/s)	258.1	219.1	192.4	173.2	158.9	148.9
Average flow speed of outlet (z direction) (m/s)	193.8	168.2	149.4	134.9	122.7	113.6
Average thrust (kg/s)(m/s)=(N)	1.4	1.2	1.1	0.9	0.9	0.8
Average thrustX24 (N)	32.8	28.4	25.2	22.8	20.7	19.1
Maximum temperature in combustor	2374	2332	2286	2189	2122	2047
Maximum temperature on liners	1647	1519	1392	1289	1219	1194
Maximum reaction rate in combustor	265	255	108	93	82	70
Average outlet mass fraction of CO_2	2.99E-02	2.47E-02	2.11E-02	1.83E-02	1.67E-02	1.50E-02
Average outlet mass flow rate of CO_2 (kg/s)	2.112E-04	1.742E-04	1.483E-04	1.290E-04	1.172E-04	1.050E-04
Average outlet mass fraction of H_2O	2.45E-02	1.82E-02	1.38E-02	1.05E-02	8.20E-03	6.14E-03
Average outlet mass flow rate of H_2O (kg/s)	1.729E-04	1.284E-04	9.716E-05	7.391E-05	5.758E-05	4.306E-05

Table 4-4 (b) Simulation results for combustion case of 120000 rpm

Rotational speed = 120000 rpm						
Mass fraction of methane in fuel mixture	1	0.9	0.8	0.7	0.6	0.5
Outlet mass flow rate (kg/s)	4.670E-03	4.667E-03	4.663E-03	4.657E-03	4.648E-03	4.650E-03
Outlet maximum temperature (K)	1181	945	768	644	565	509
Outlet maximum speed (z direction) (m/s)	190.9	162.6	142.0	127.3	116.6	109.2
Average flow speed of outlet (z direction) (m/s)	142.8	124.0	109.4	98.1	89.1	82.4
Average thrust (kg/s)(m/s)=(N)	0.7	0.6	0.5	0.5	0.4	0.4
Average thrustX24 (N)	16.0	13.9	12.2	11.0	9.9	9.2
Maximum temperature in combustor	2364	2329	2275	2177	2104	2017.7
Maximum temperature on liners	1577.7	1481	1319	1191	1132	1096.8
Maximum reaction rate in combustor	176	189	75	63	55	48
Average outlet mass fraction of CO_2	2.97E-02	2.44E-02	2.08E-02	1.82E-02	1.66E-02	1.49E-02
Average outlet mass flow rate of CO_2 (kg/s)	1.386E-04	1.139E-04	9.712E-05	8.454E-05	7.702E-05	6.926E-05
Average outlet mass fraction of H_2O	2.43E-02	1.80E-02	1.36E-02	1.04E-02	8.14E-03	6.11E-03
Average outlet mass flow rate of H_2O (kg/s)	1.134E-04	8.392E-05	6.363E-05	4.844E-05	3.783E-05	2.840E-05

Table 4-4 (c) Simulation results for combustion case of 80000 rpm

Rotational speed = 80000 rpm						
Mass fraction of methane in fuel mixture	1	0.9	0.8	0.7	0.6	0.5
Outlet mass flow rate (kg/s)	3.215E-03	3.213E-03	3.210E-03	3.207E-03	3.197E-03	3.197E-03
Outlet maximum temperature (K)	1158	924	750	624	554	485
Outlet maximum speed (z direction) (m/s)	151.2	128.2	111.5	99.5	91.7	84.1
Average flow speed of outlet (z direction) (m/s)	112.9	97.5	85.6	76.4	69.9	63.2
Average thrust (kg/s)(m/s)=(N)	0.4	0.3	0.3	0.2	0.2	0.2
Average thrustX24 (N)	8.7	7.5	6.6	5.9	5.4	4.9
Maximum temperature in combustor	2359	2319	2273	2163	2080	2012.4
Maximum temperature on liners	1523	1416	1263	1110	1073	948.5
Maximum reaction rate in combustor	95	143	68	47	41	36
Average outlet mass fraction of CO_2	2.92E-02	2.44E-02	2.08E-02	1.81E-02	1.69E-02	1.50E-02
Average outlet mass flow rate of CO_2 (kg/s)	9.397E-05	7.849E-05	6.688E-05	5.815E-05	5.387E-05	4.798E-05
Average outlet mass fraction of H_2O	2.39E-02	1.80E-02	1.36E-02	1.04E-02	8.28E-03	6.15E-03
Average outlet mass flow rate of H_2O (kg/s)	7.693E-05	5.784E-05	4.382E-05	3.333E-05	2.647E-05	1.967E-05

Table 4-4 (d) Simulation results for combustion case of 45000 rpm

Rotational speed = 45000 rpm (idle)						
Mass fraction of methane in fuel mixture	1	0.9	0.8	0.7	0.6	0.5
Outlet mass flow rate (kg/s)	1.275E-03	1.274E-03	1.272E-03	1.269E-03	1.269E-03	1.268E-03
Outlet maximum temperature (K)	1091	876	715	600	527	476
Outlet maximum speed (z direction) (m/s)	64.6	54.9	48.0	43.0	39.5	37.0
Average flow speed of outlet (z direction) (m/s)	48.6	41.7	36.6	32.6	29.6	27.4
Average thrust (kg/s)(m/s)=(N)	0.1	0.1	0.0	0.0	0.0	0.0
Average thrustX24 (N)	1.5	1.3	1.1	1.0	0.9	0.8
Maximum temperature in combustor	2349.19	2317	2265.5	2170.8	2110.5	2021
Maximum temperature on liners	1371	1222	1097.2	956.5	875.4	842.4
Maximum reaction rate in combustor	45	40	37	24	27	25
Average outlet mass fraction of CO_2	2.87E-02	2.38E-02	2.06E-02	1.84E-02	1.65E-02	1.48E-02
Average outlet mass flow rate of CO_2 (kg/s)	3.661E-05	3.035E-05	2.627E-05	2.334E-05	2.093E-05	1.876E-05
Average outlet mass fraction of H_2O	2.35E-02	1.76E-02	1.35E-02	1.05E-02	8.11E-03	6.06E-03
Average outlet mass flow rate of H_2O (kg/s)	2.997E-05	2.236E-05	1.721E-05	1.337E-05	1.028E-05	7.685E-06

(a) Micro gas turbine WREN MW54 (b) The core of WREN MW54

Fig. 2-1 Micro gas turbine WREN MW54

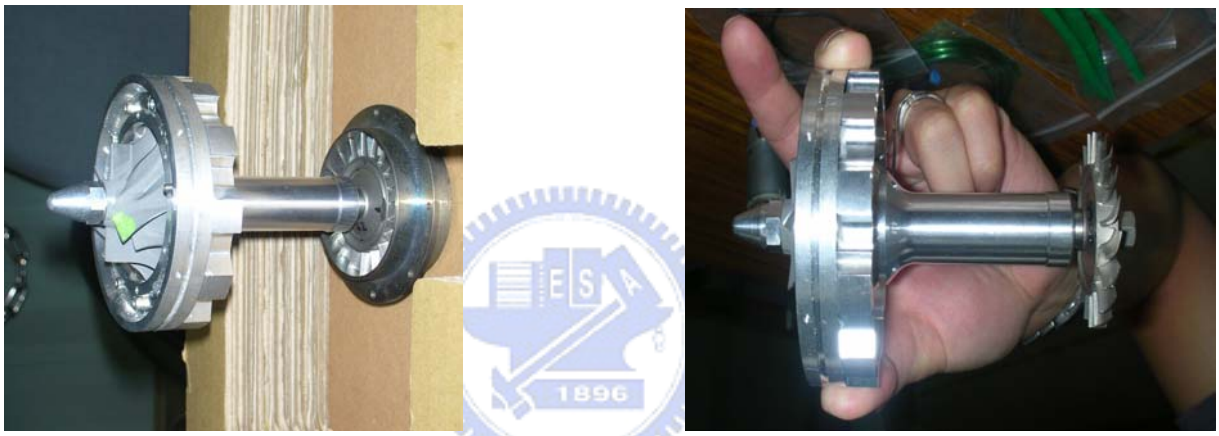

(a) Compressor, diffuser, turbine (b) The lateral view of (a)

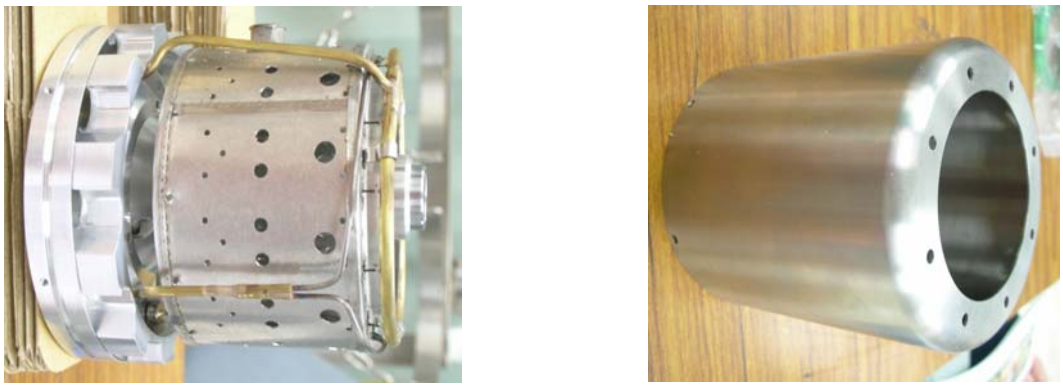

(c) Combustion chamber (d) Casing

Fig. 2-2 Components of the micro gas turbine WREN MW54

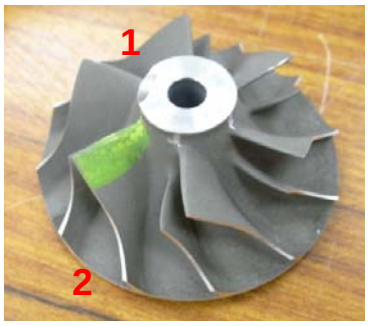

(a) Compressor (1, 2 represent air property at inlet and outlet, respectively)

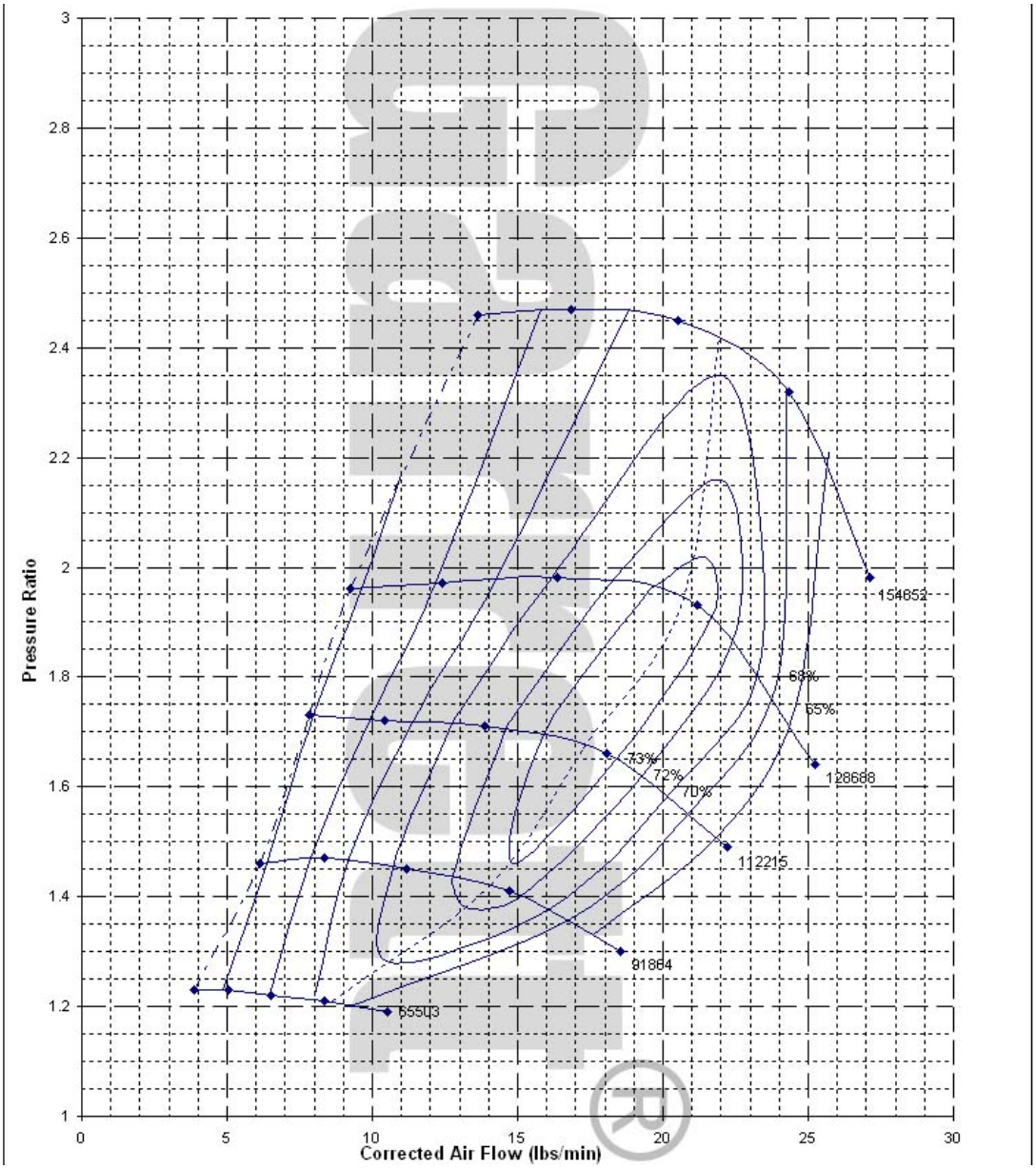

(b) Compressor map

Fig. 2-3 Compressor and compressor map

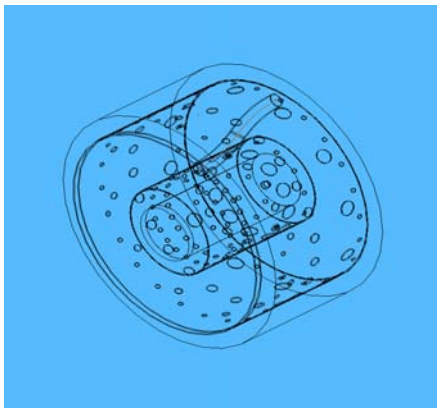

(a) Annulus combustion chamber

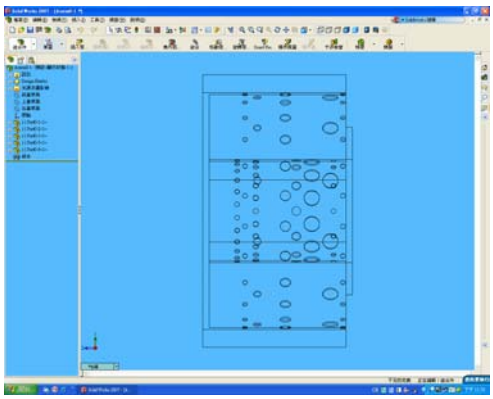

(b) The lateral view of (a)

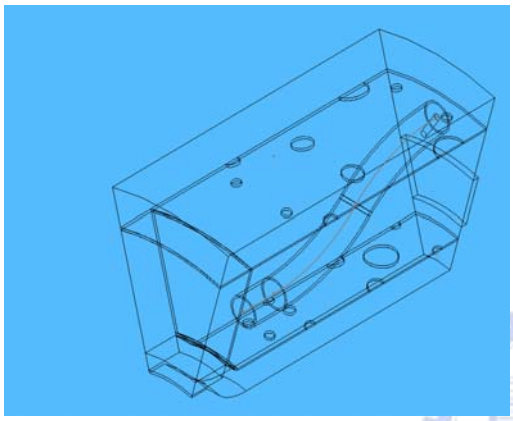

(c) One sub-chamber (one-twelfth) of annulus combustion chamber

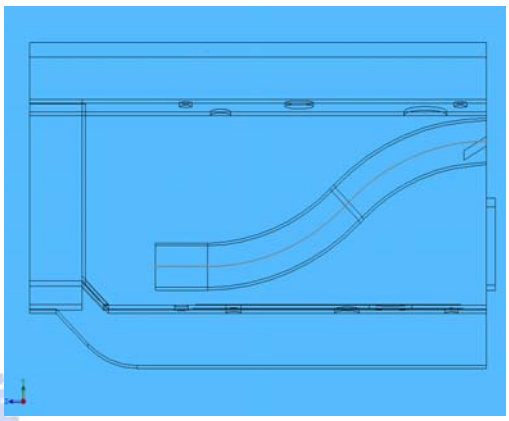

(d) The lateral view of (c)

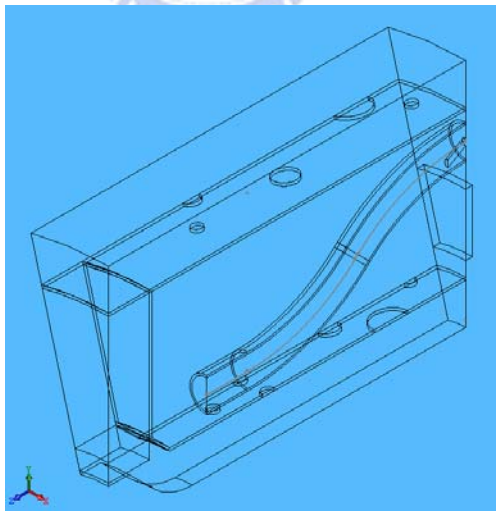

(e) The computational domain of symmetric zone of sub-chamber

Fig. 2-4 The simplifying procedure of model domain illustrated by software Solid Works

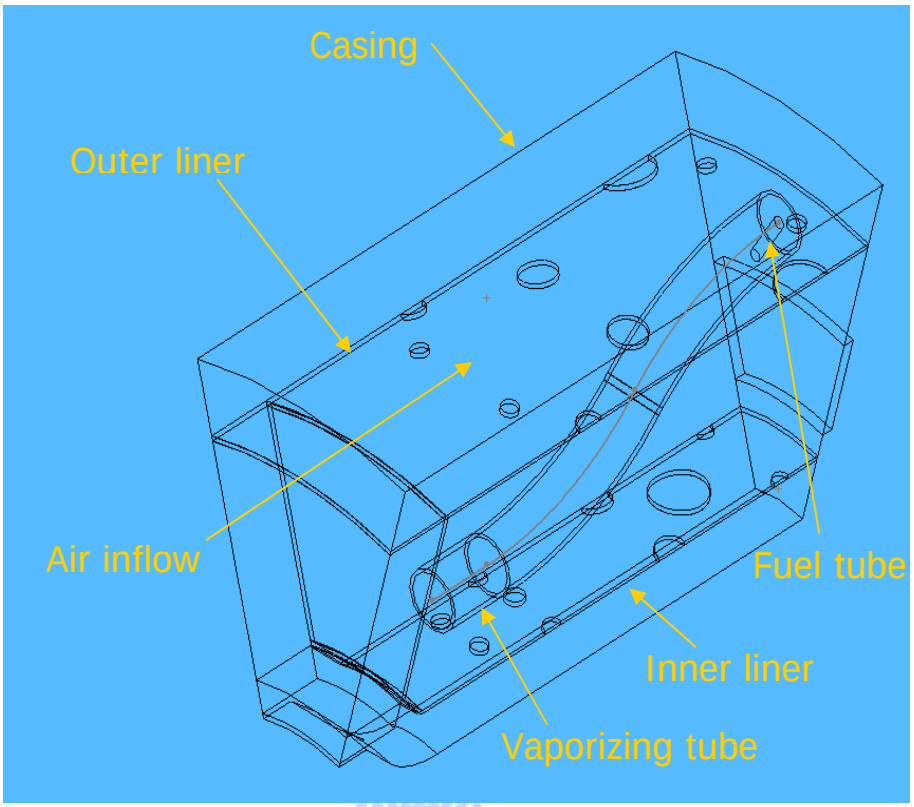

(a) The components configuration of sub-chamber

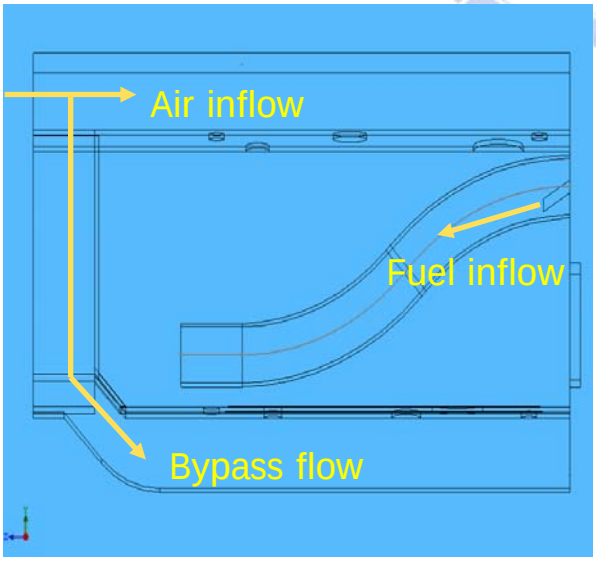

(b) The flow configuration of air inflow and fuel inflow

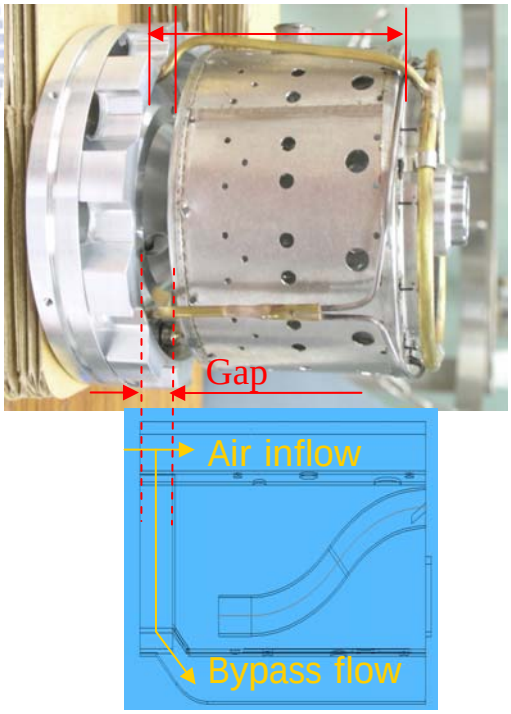

(c) The corresponding zone of actual chamber

Fig. 2-5 The configurations of a sub-chamber

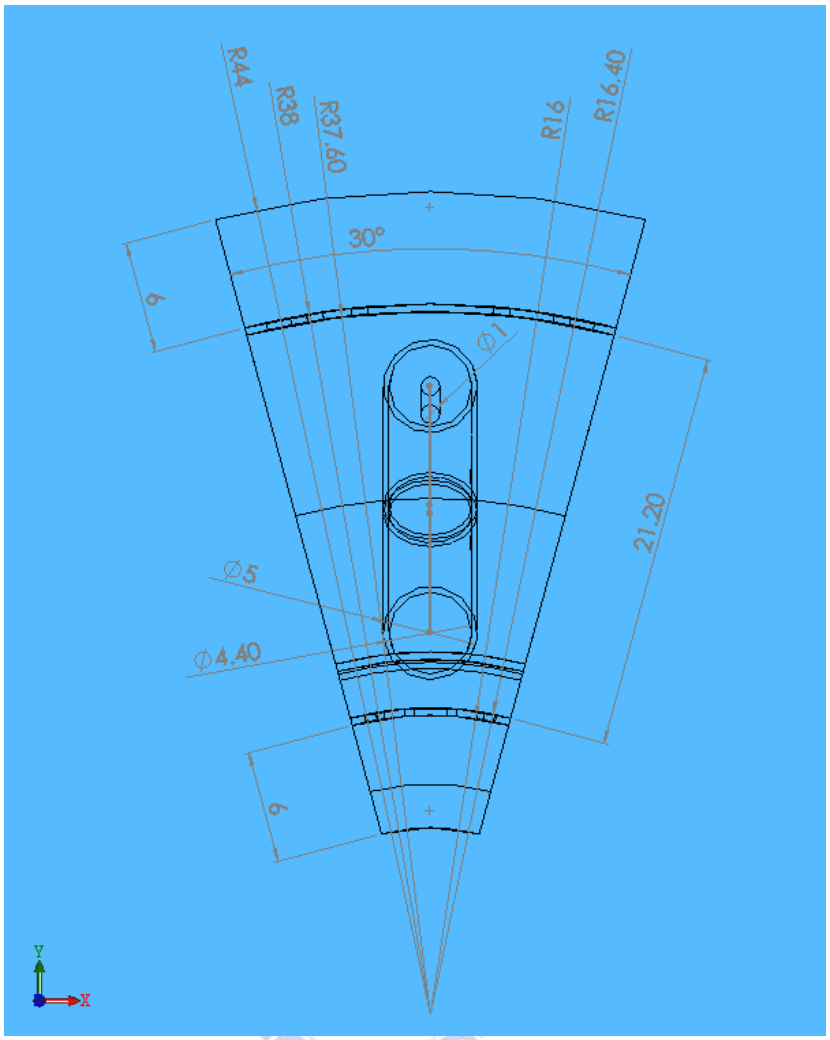

(a) The front view of sub-chamber

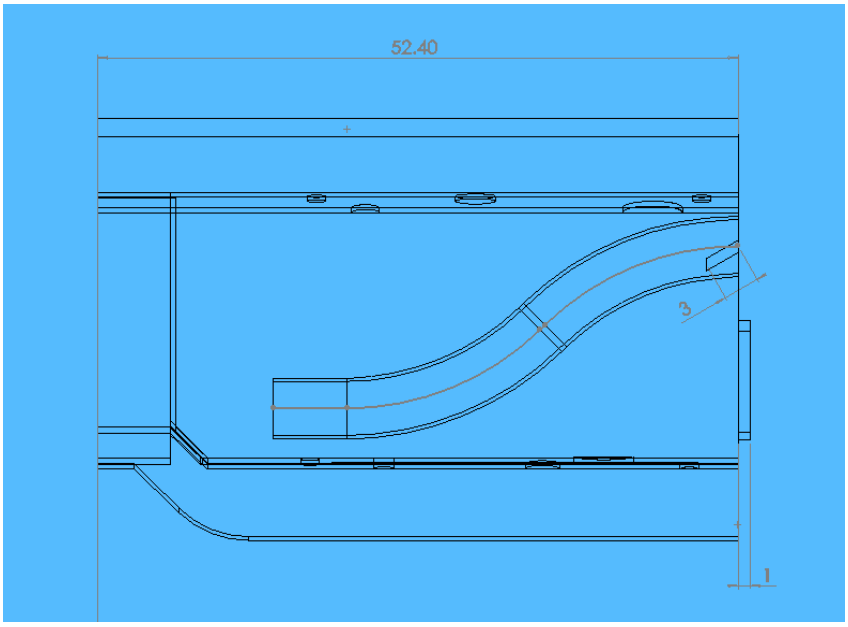

(b) The lateral view of sub-chamber

Fig. 2-6 The size specification of sub-chamber

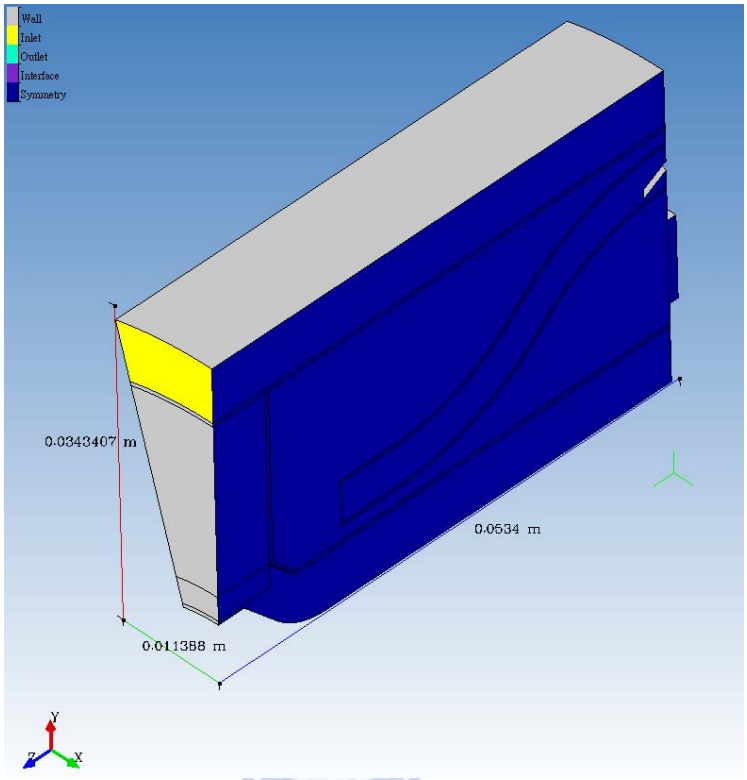

(a) Equal angle (face of air inlet, wall, symmetry)

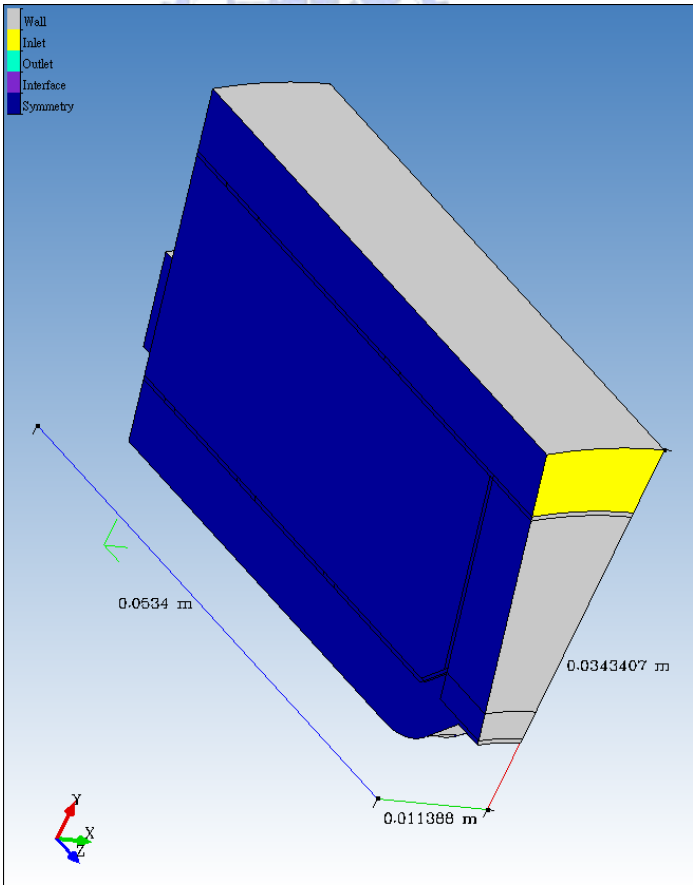

(b) The other view (face of air inlet, wall, and another symmetric face)

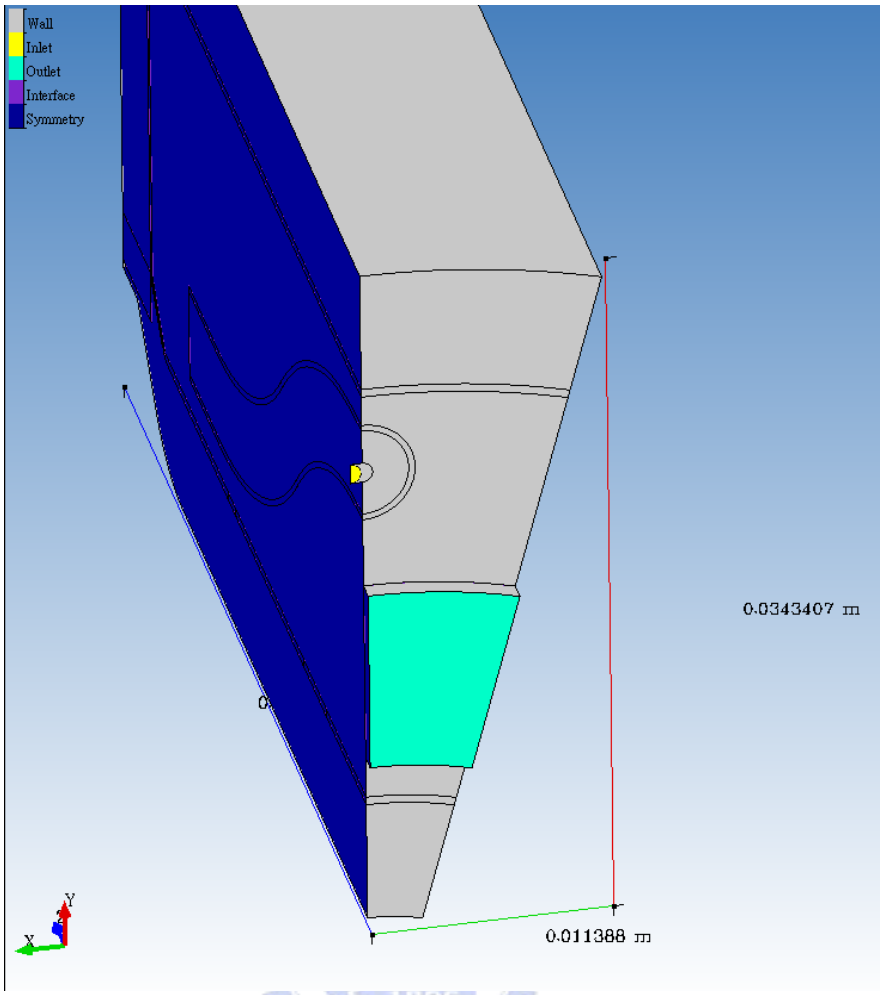

(c) The other view of combustor rear

Fig. 2-7 Boundary conditions set by software CFD-CADalyzer (Color denotation: yellow, inlet; green, outlet; blue, symmetry; gray, wall)

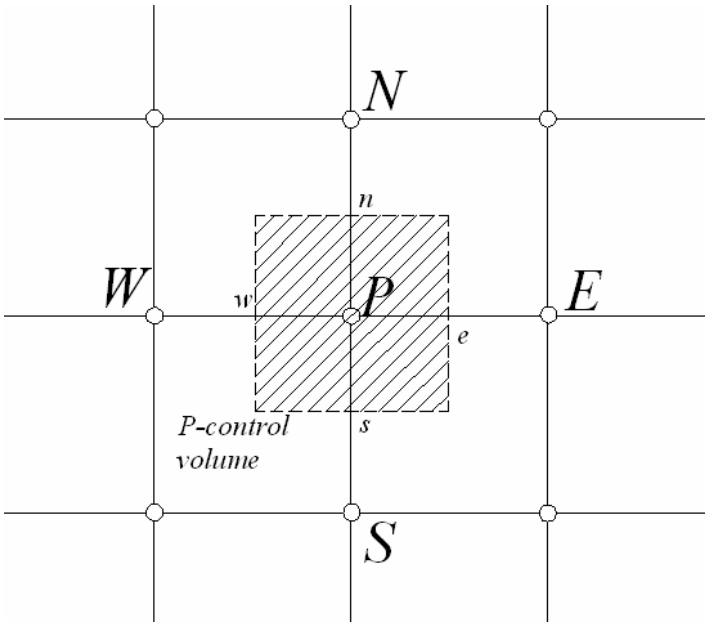

(a) Illustration of Control volume grids

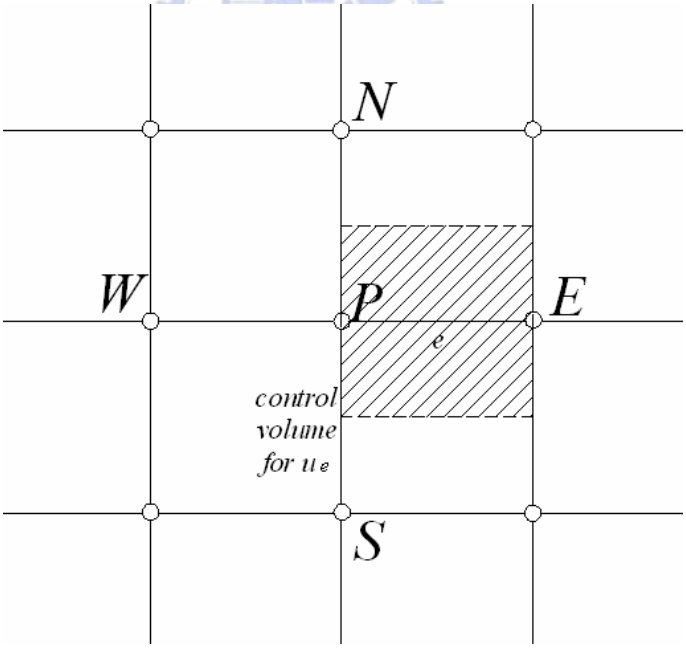

(b) Illustration of Control volume grids for u_e consideration

Fig. 3-1 Control volume grids

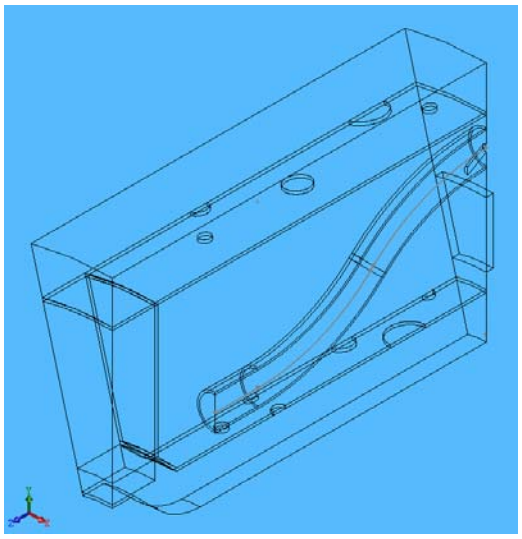

(a) Model domain of combustor

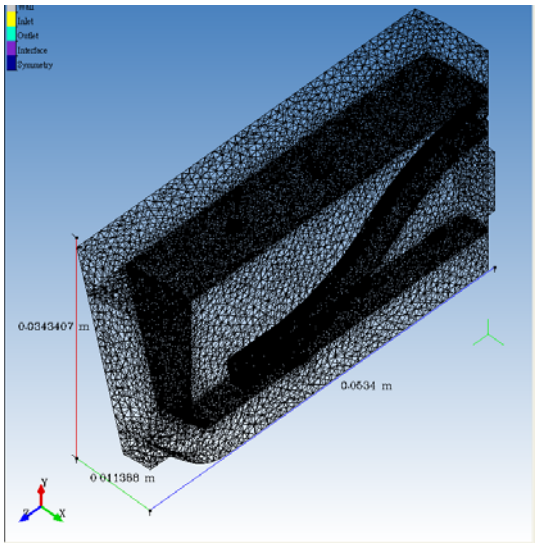

(b) Grids generation

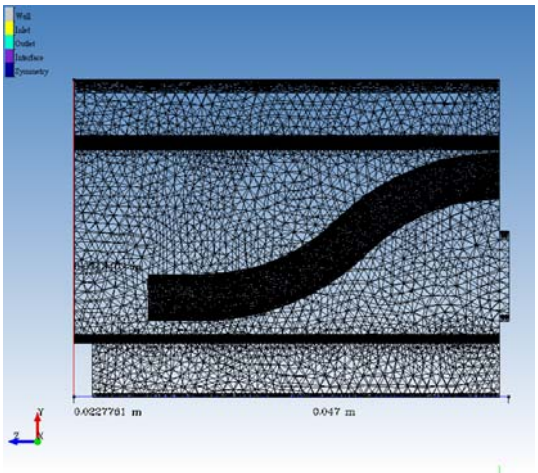

(c) Lateral view of (b)

Fig. 3-2 Grids generation for numerical computation

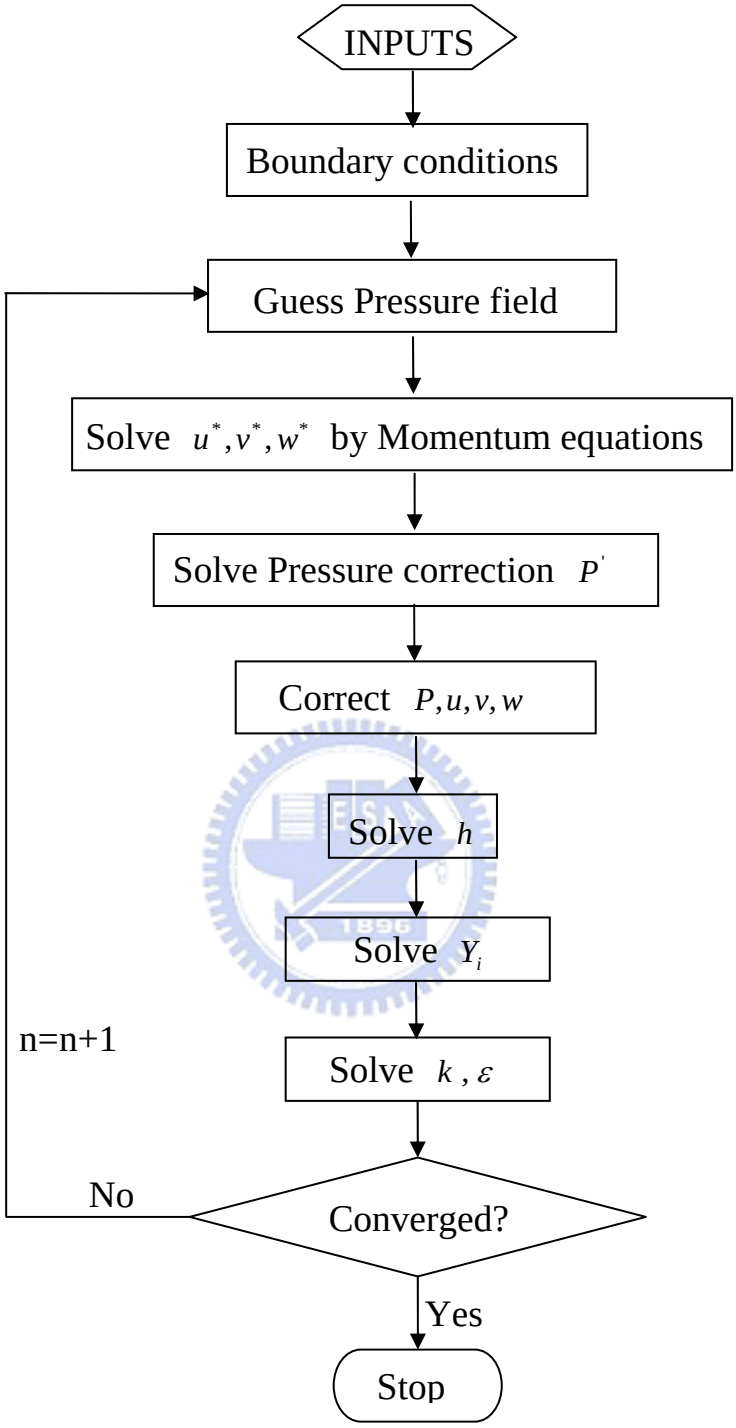

Fig. 3-3 Flowchart of CFD-ACE+ solution algorithm

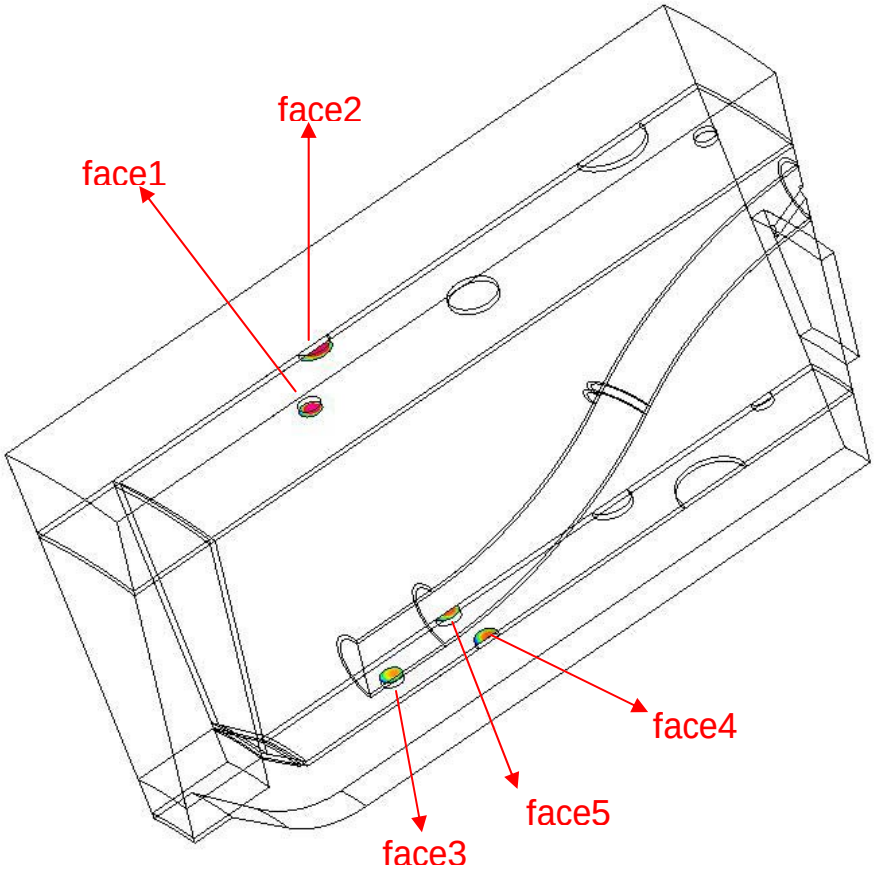

Fig. 3-4 Configuration of liner holes for primary zone

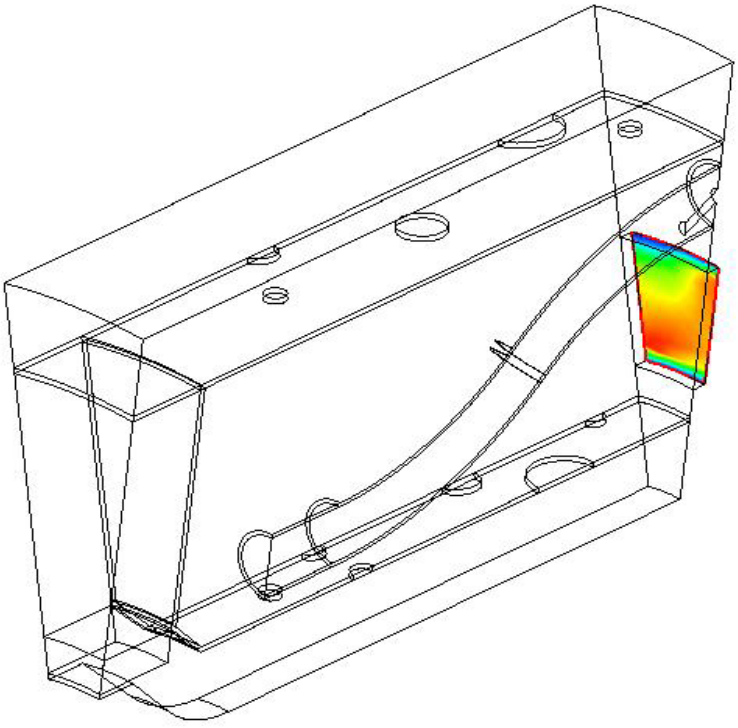

Fig. 3-5 Display of physical quantities for combustor outlet

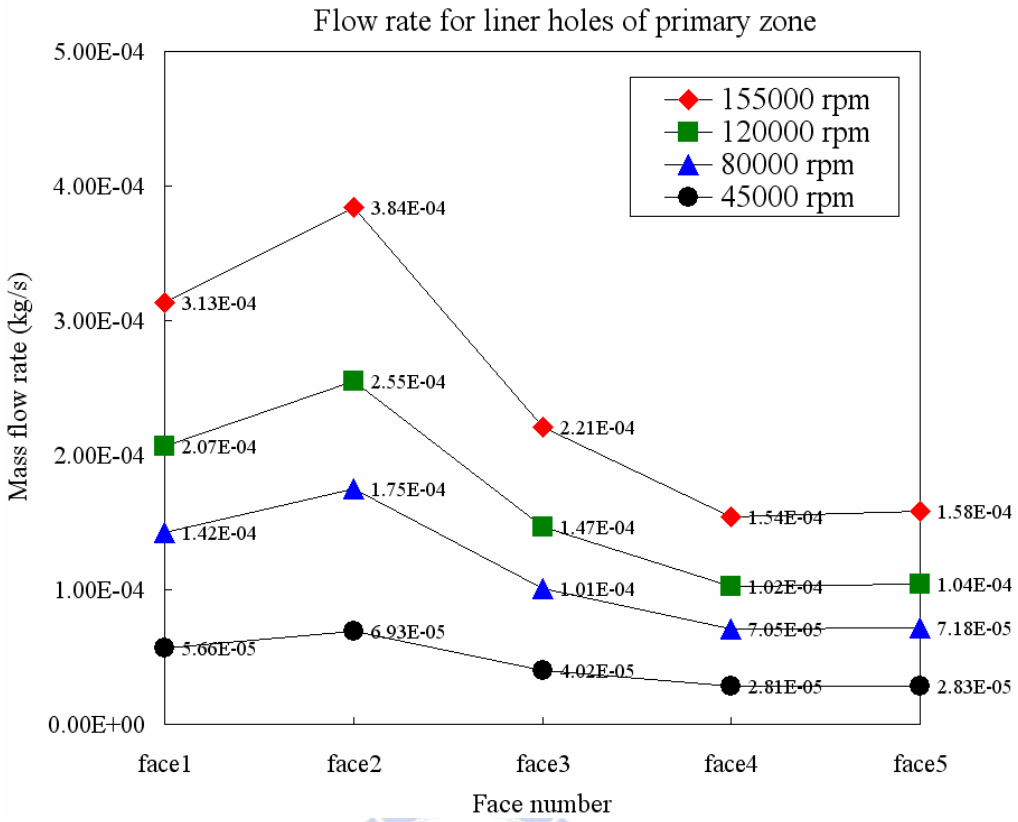

Fig. 4-1 Liner hole mass flow rates in primary zone for cold flow case

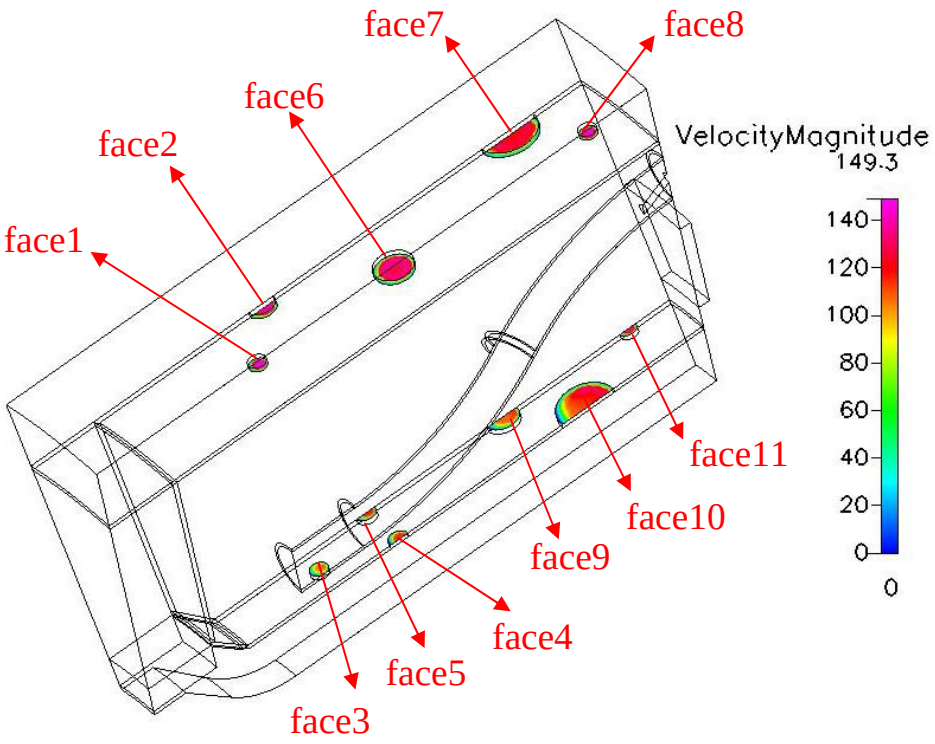

Fig. 4-2 Configuration of liner holes

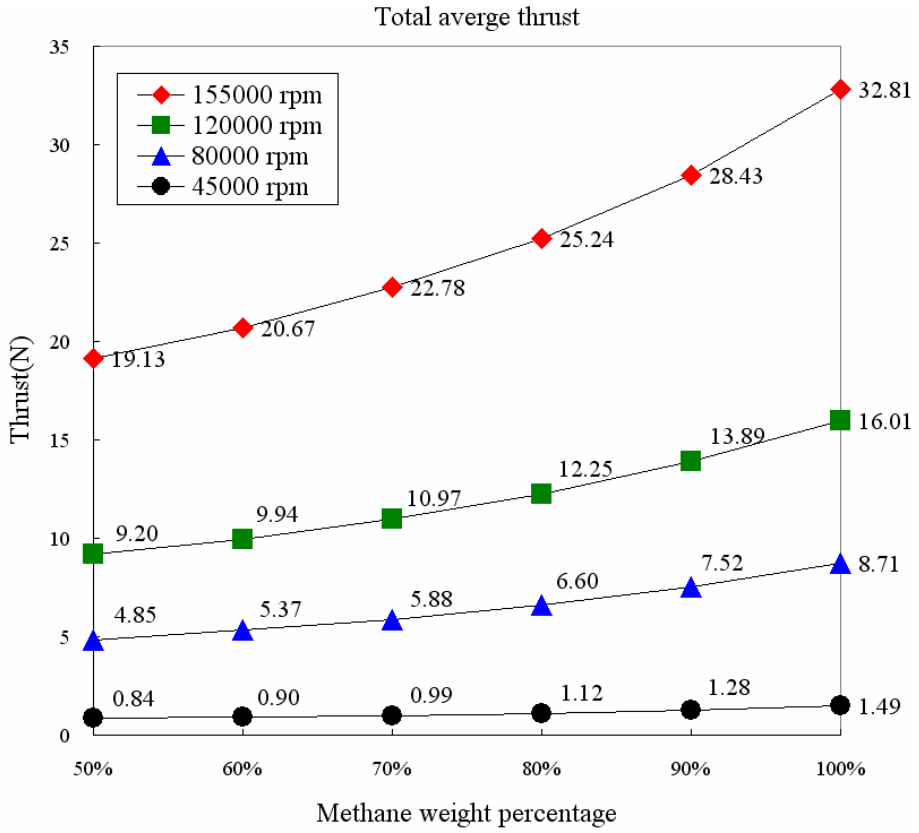

Fig. 4-3 Total average thrust with different methane mass fractions

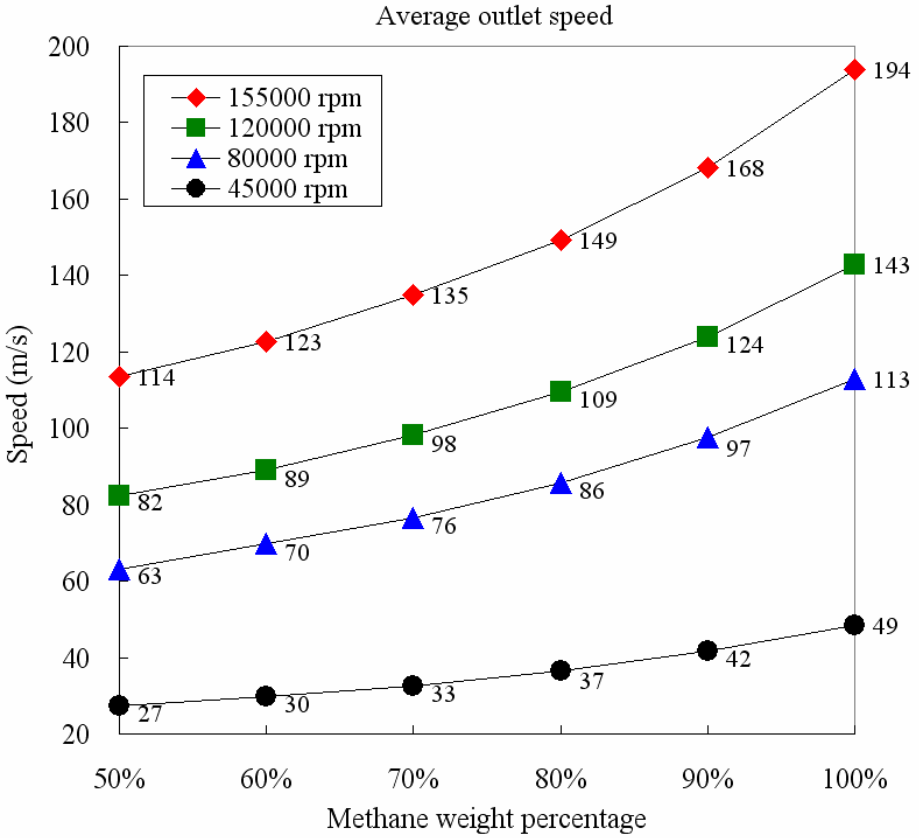

Fig. 4-4 Average flow speed of combustor outlet

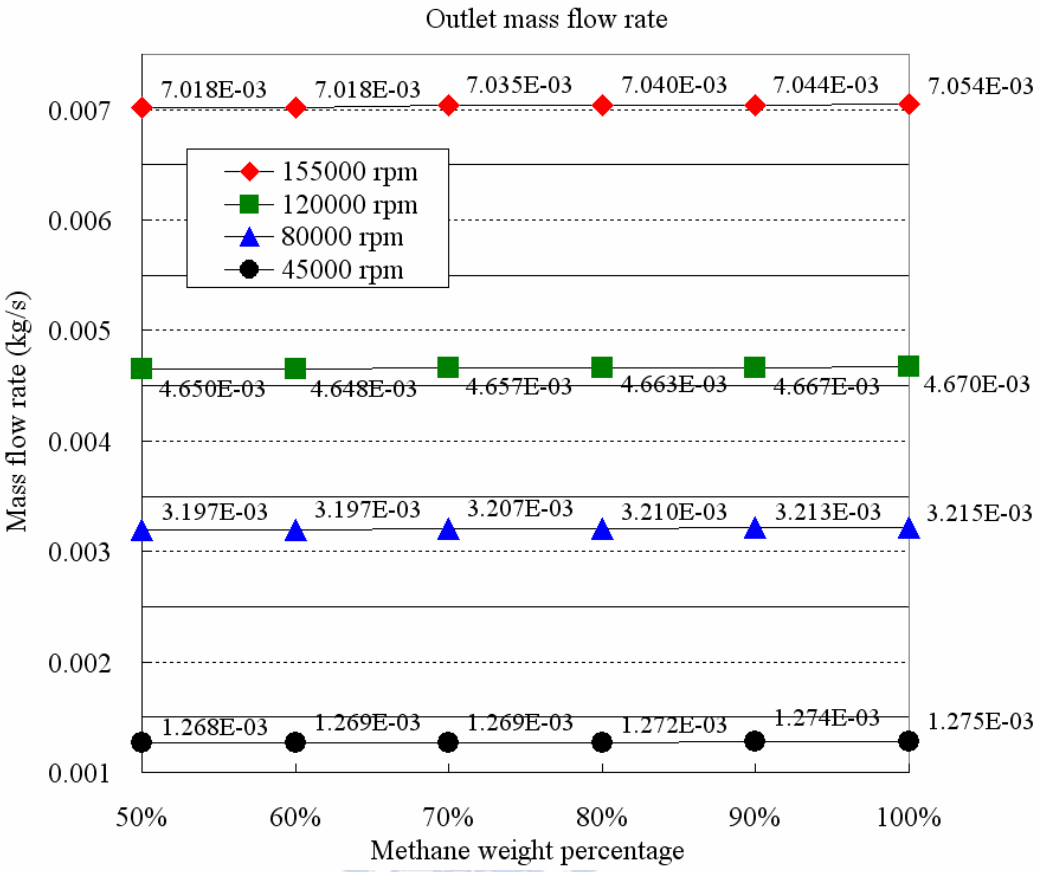

Fig. 4-5 Outlet mass flow rate of combustor

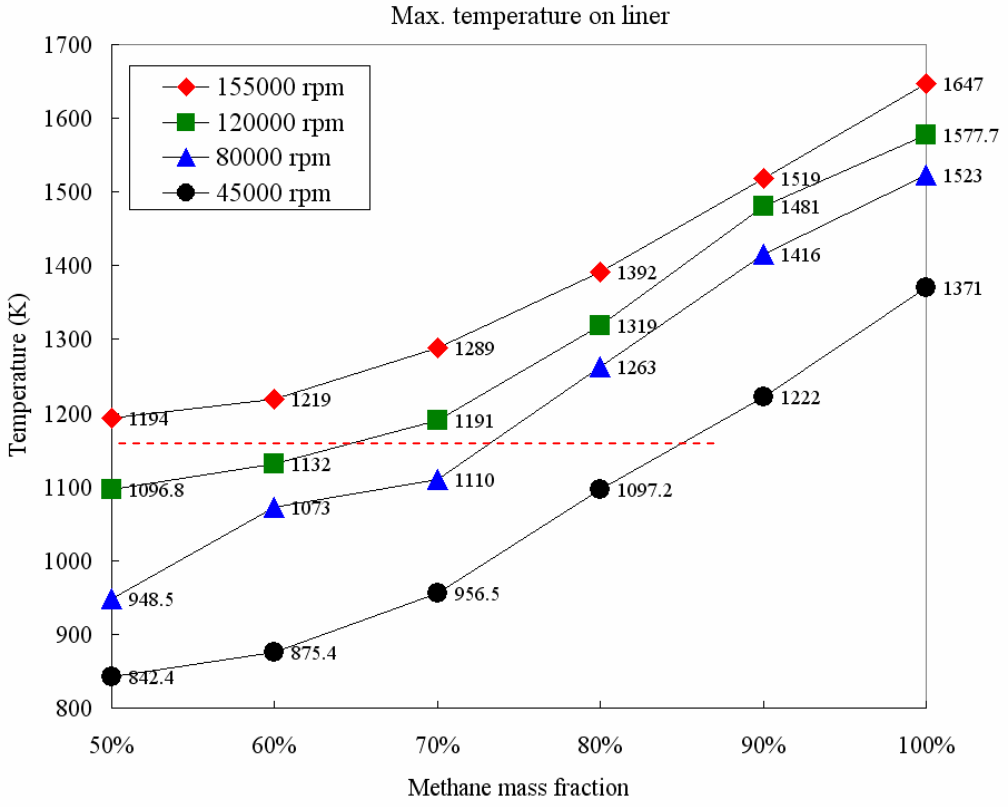

Fig. 4-6 Maximum temperature on liners of combustor

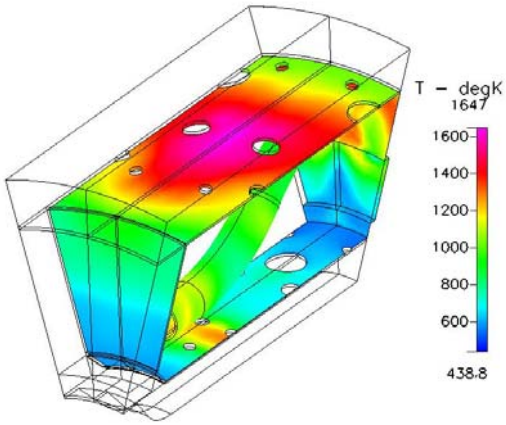

(a) Methane concentration 100%

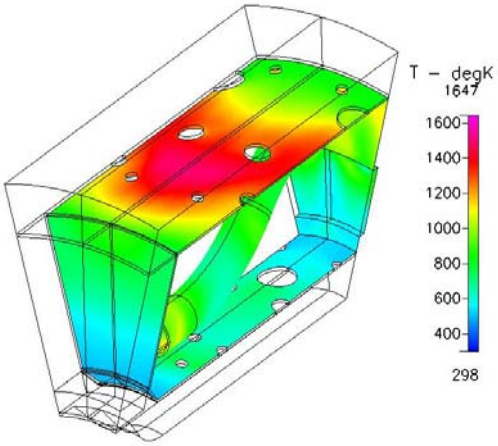

(b) Methane concentration 90%

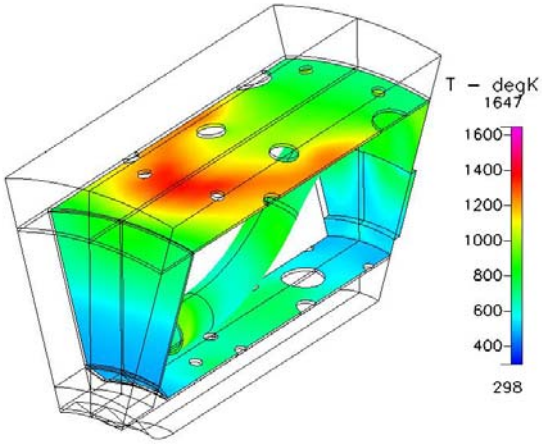

(c) Methane concentration 80%

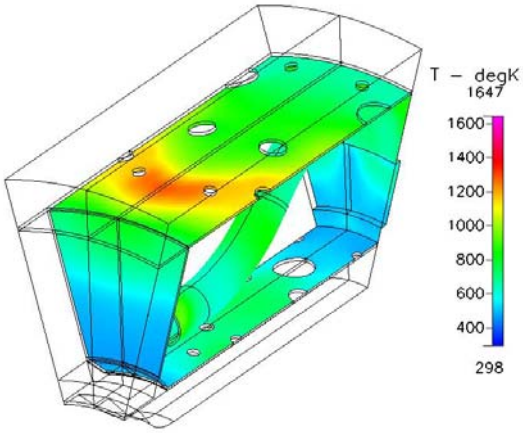

(d) Methane concentration 70%

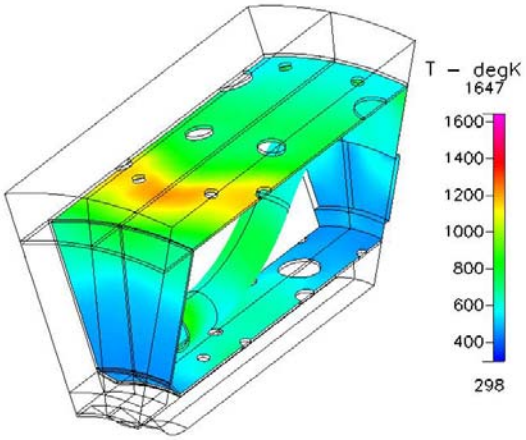

(e) Methane concentration 60%

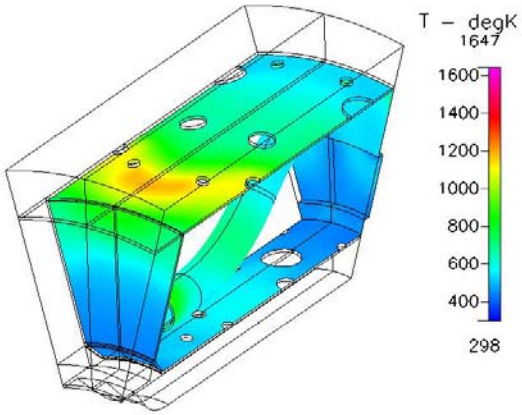

(f) Methane concentration 50%

Fig. 4-7 Temperature distributions on solid liners and vaporizing tube

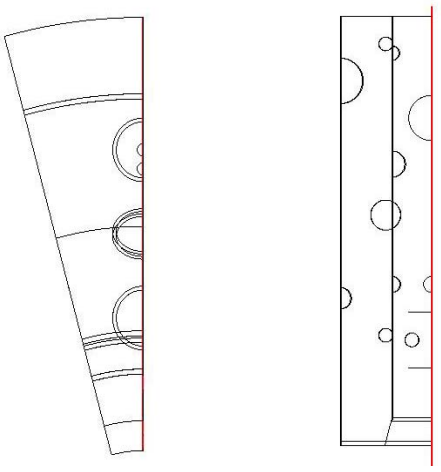

(a) Front view (b) Top view

Fig. 4-8 Cross-section at 0 degree (on symmetric face)

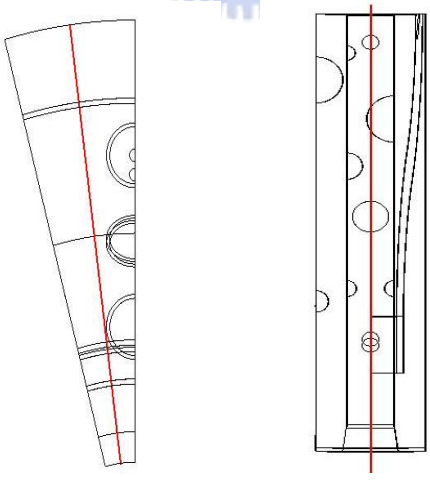

(a) Front view (b) Top view

Fig. 4-9 Cross-section at 7.5 degrees (datum on symmetric face)

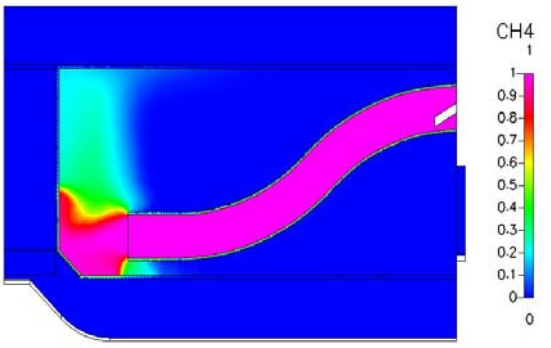

(a) Methane concentration 100%

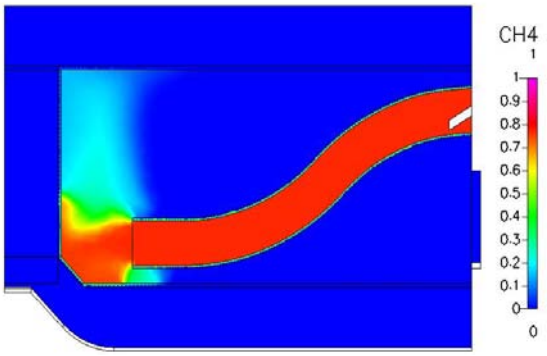

(b) Methane concentration 90%

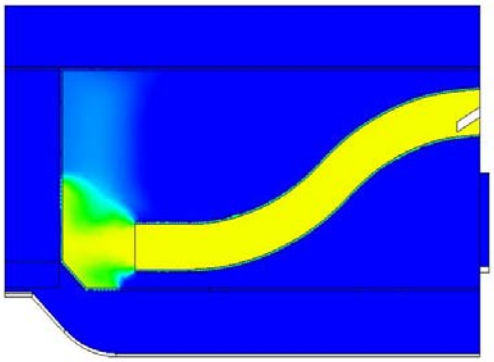

(c) Methane concentration 80%

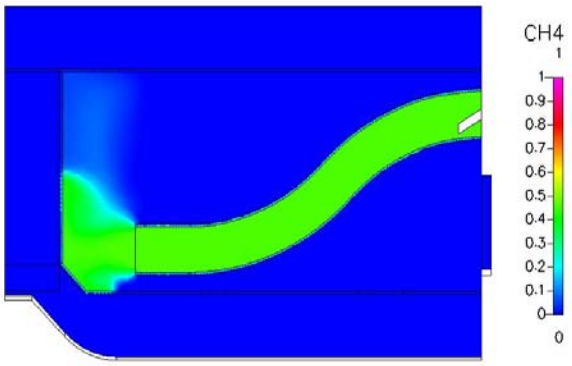

(d) Methane concentration 70%

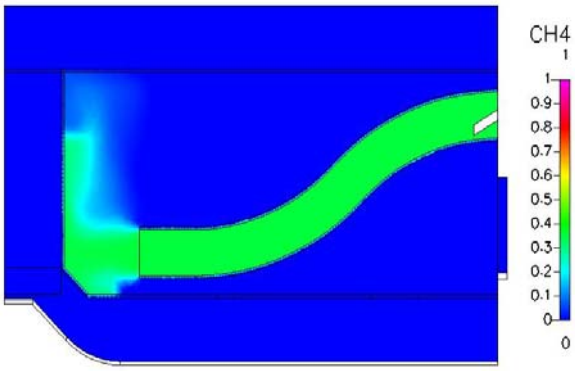

(e) Methane concentration 60%

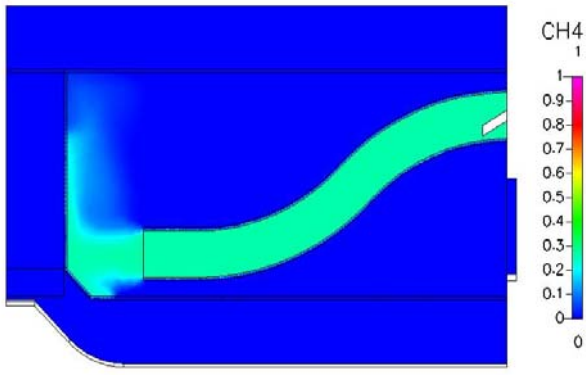

(f) Methane concentration 50%

Fig. 4-10 Distributions of CH_4 mass fraction for combustion case 155000 rpm (0 degree cross-section)

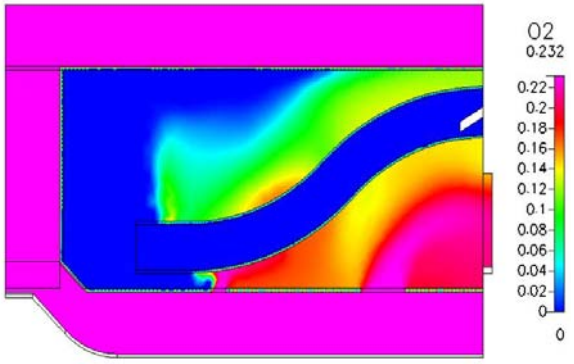

(a) Methane concentration 100%

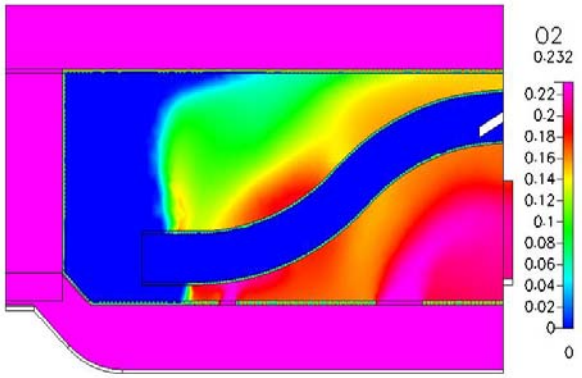

(b) Methane concentration 90%

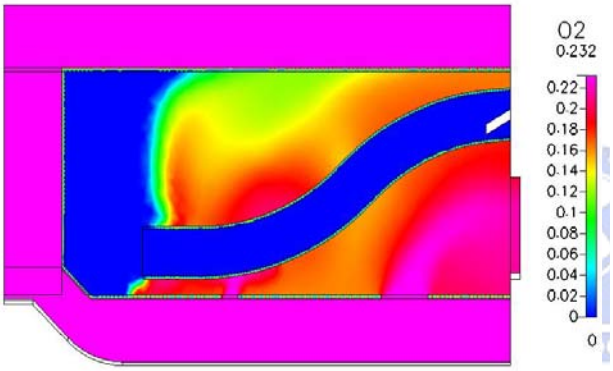

(c) Methane concentration 80%

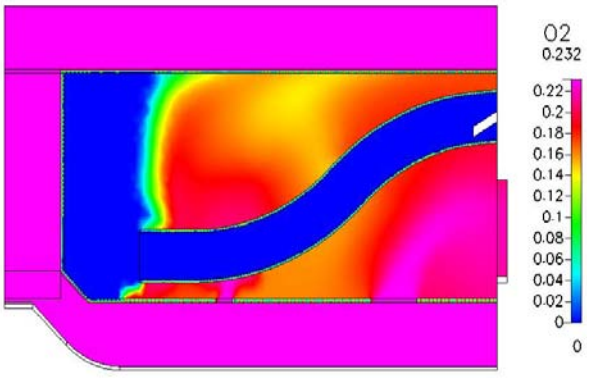

(d) Methane concentration 70%

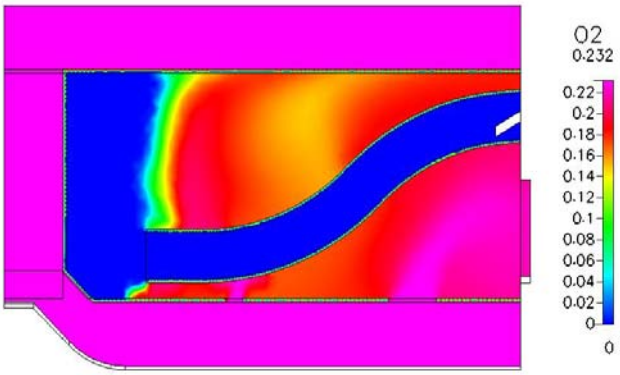

(e) Methane concentration 60%

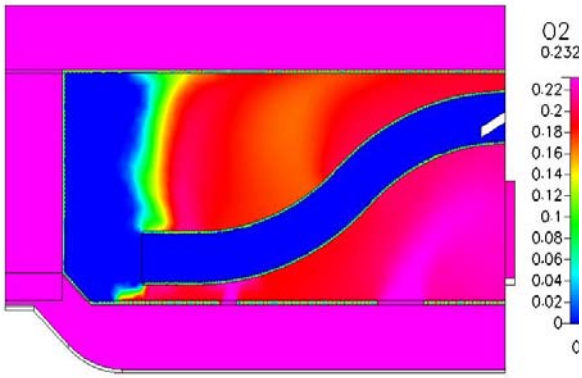

(f) Methane concentration 50%

Fig. 4-11 Distributions of O_2 mass fraction for
combustion case 155000 rpm
(0 degree cross-section)

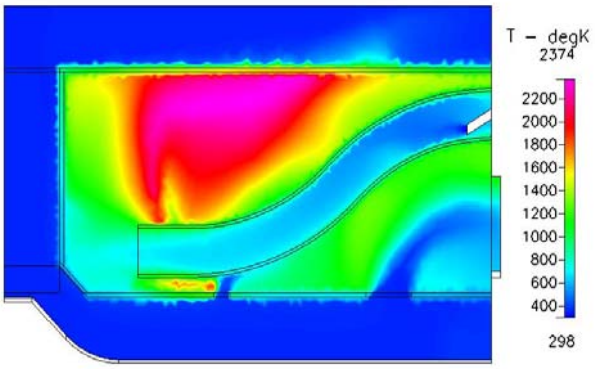

(a) Methane concentration 100%

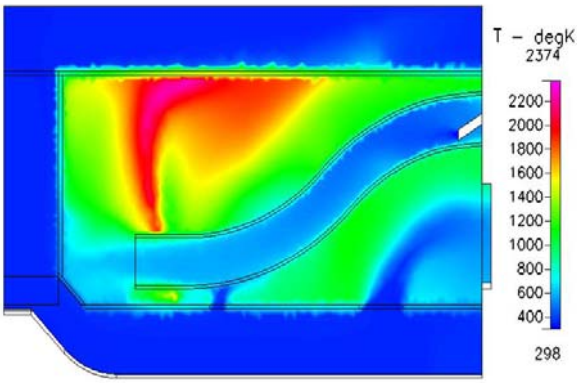

(b) Methane concentration 90%

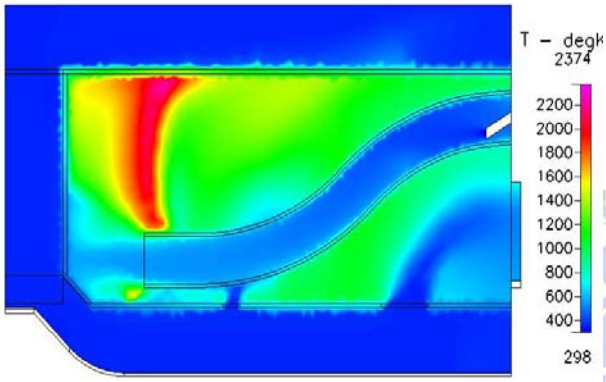

(c) Methane concentration 80%

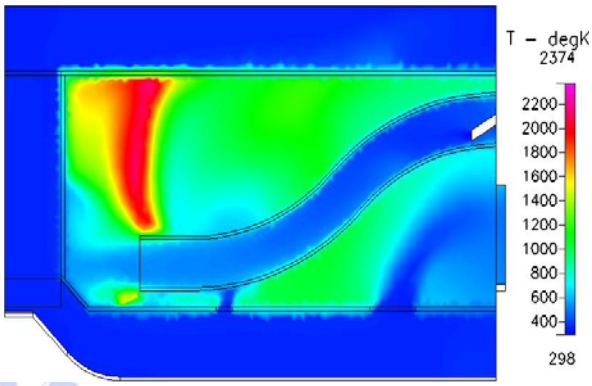

(d) Methane concentration 70%

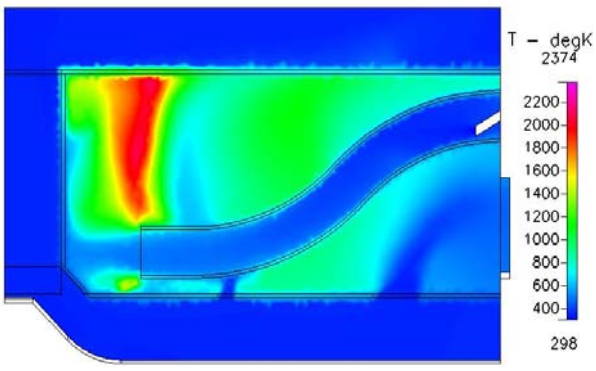

(e) Methane concentration 60%

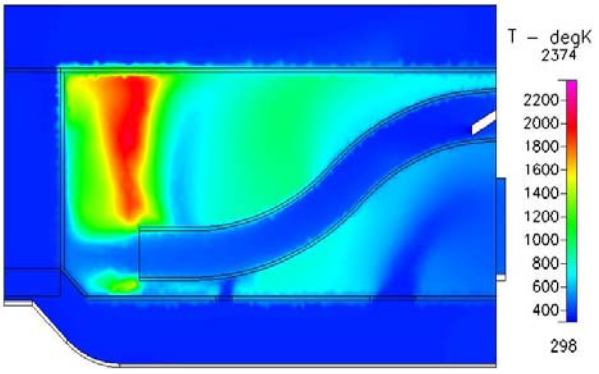

(f) Methane concentration 50%

Fig. 4-12 Distributions of temperature for combustion case 155000 rpm (0 degree cross-section)

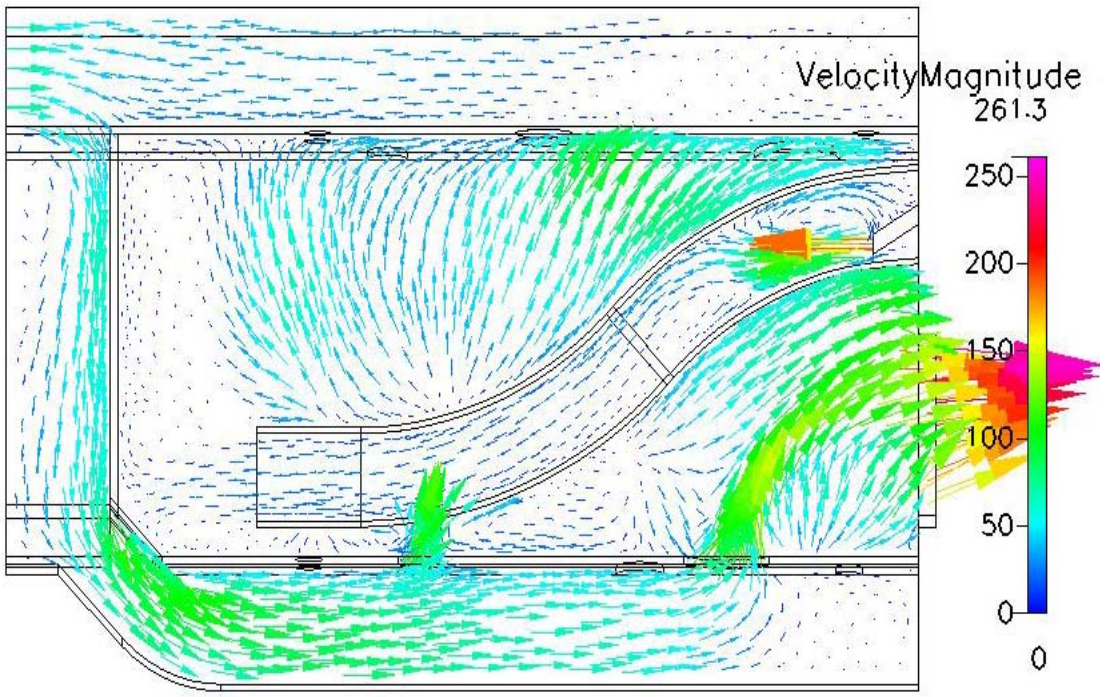

(a) Methane concentration 100%

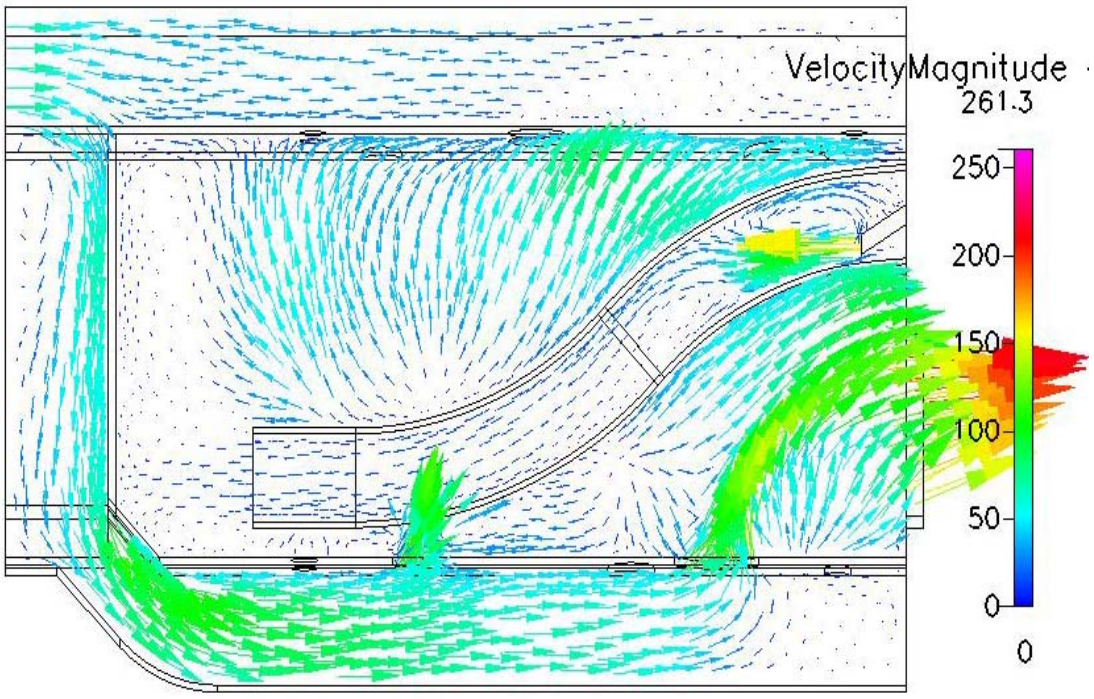

(b) Methane concentration 90%

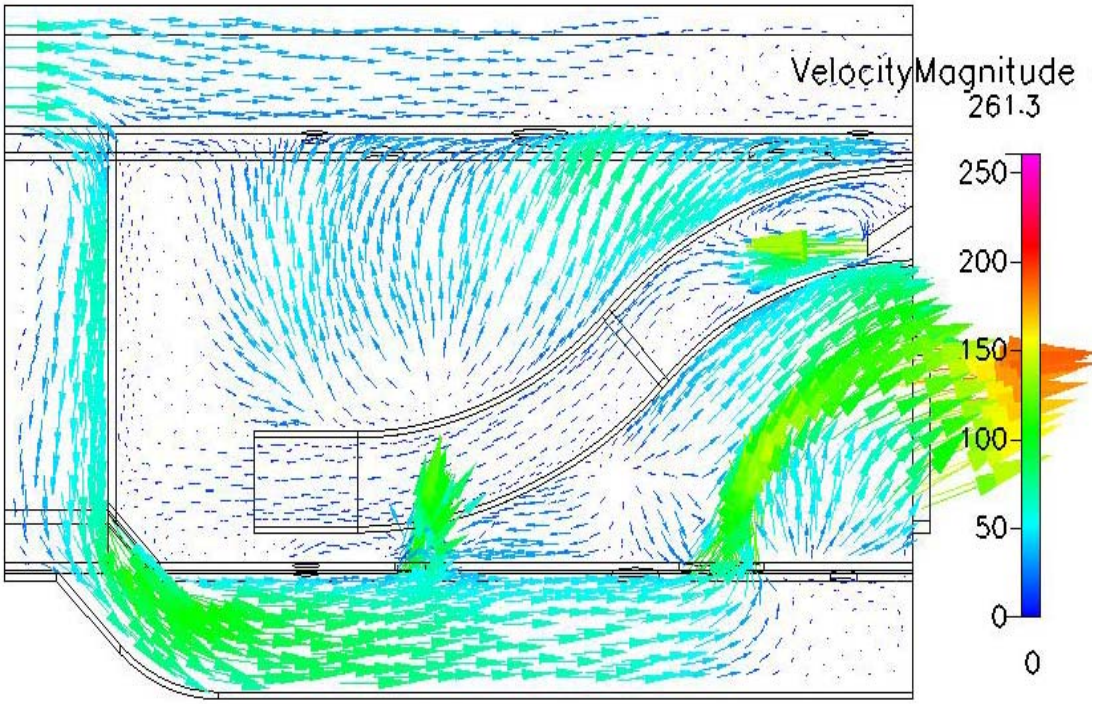

(c) Methane concentration 80%

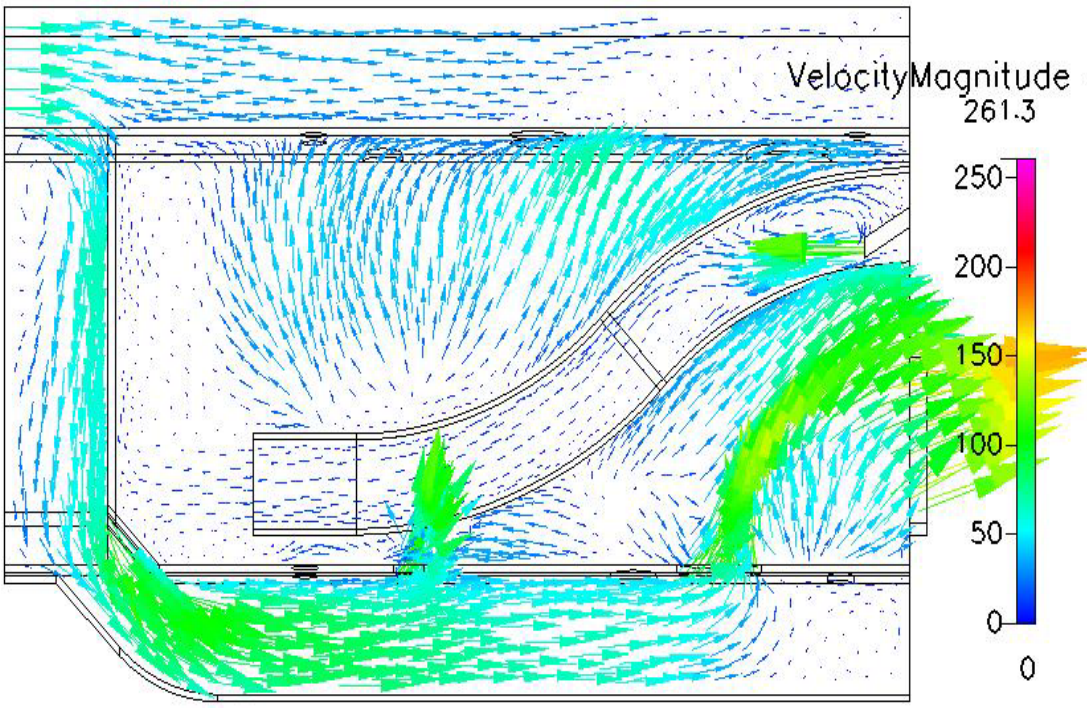

(d) Methane concentration 70%

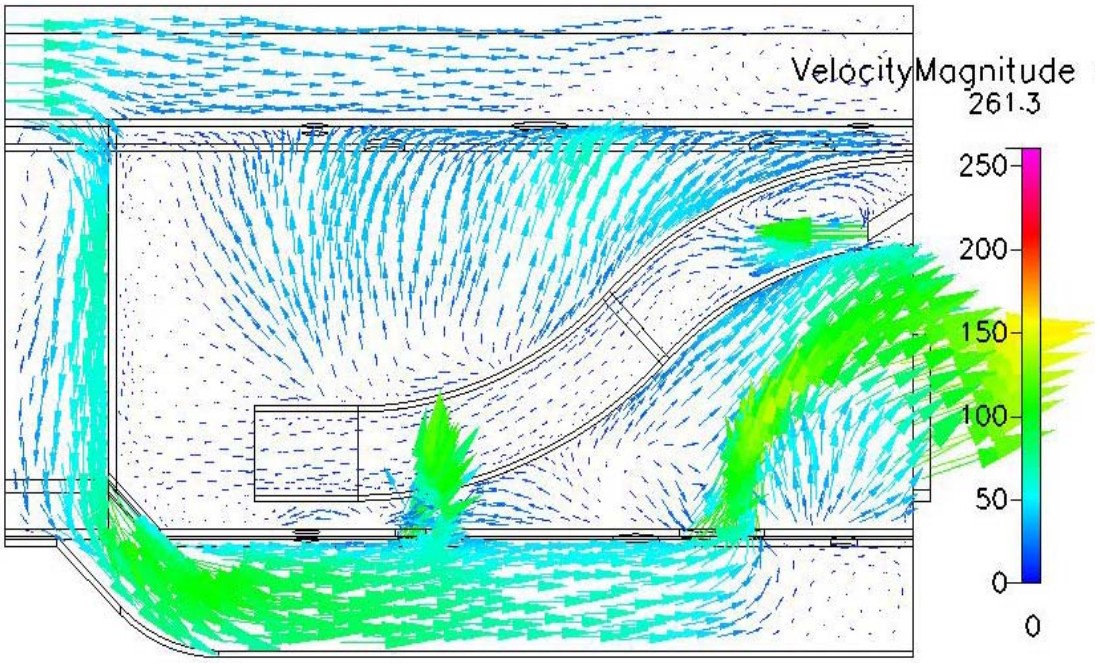

(e) Methane concentration 60%

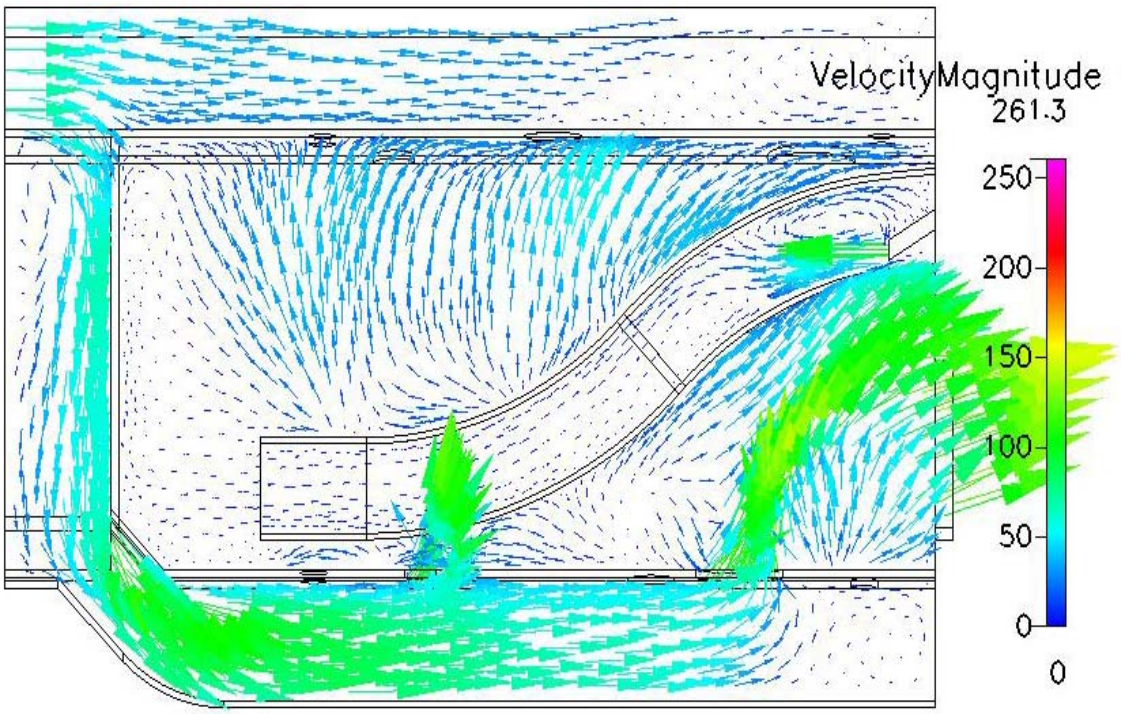

(f) Methane concentration 50%

Fig. 4-13 Velocity vector of flow field for combustion case 155000 rpm (0 degree cross-section)

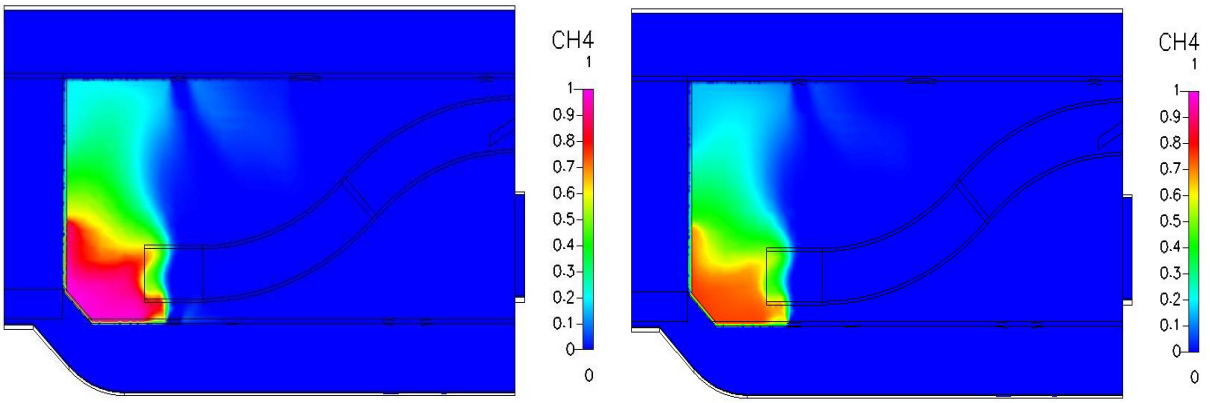

(a) Methane concentration 100% (b) Methane concentration 90%

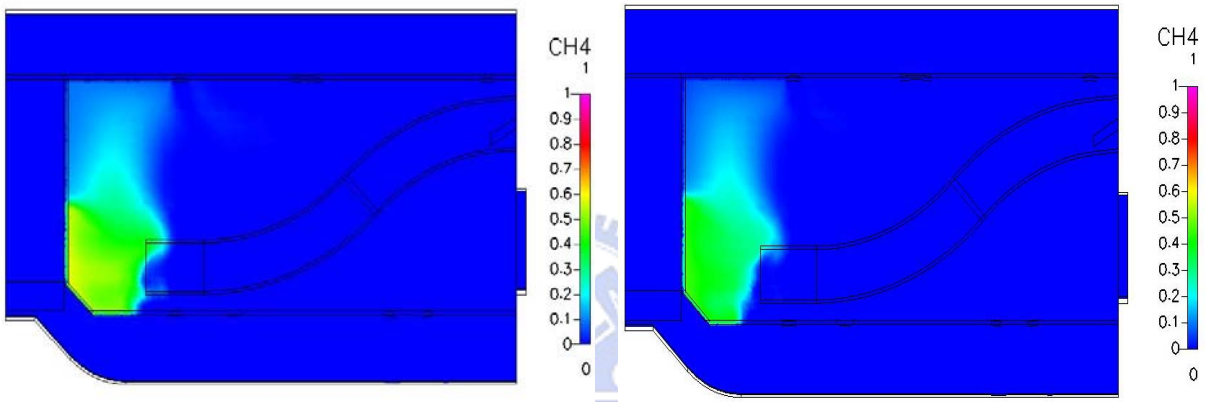

(c) Methane concentration 80% (d) Methane concentration 70%

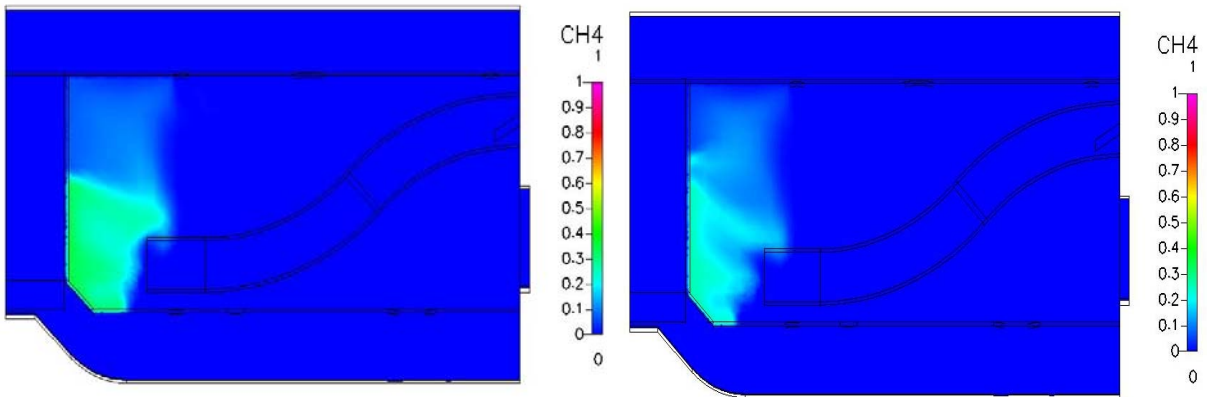

(e) Methane concentration 60% (f) Methane concentration 50%

Fig. 4-14 Distributions of CH_4 mass fraction for combustion case 155000 rpm (7.5 degrees cross-section)

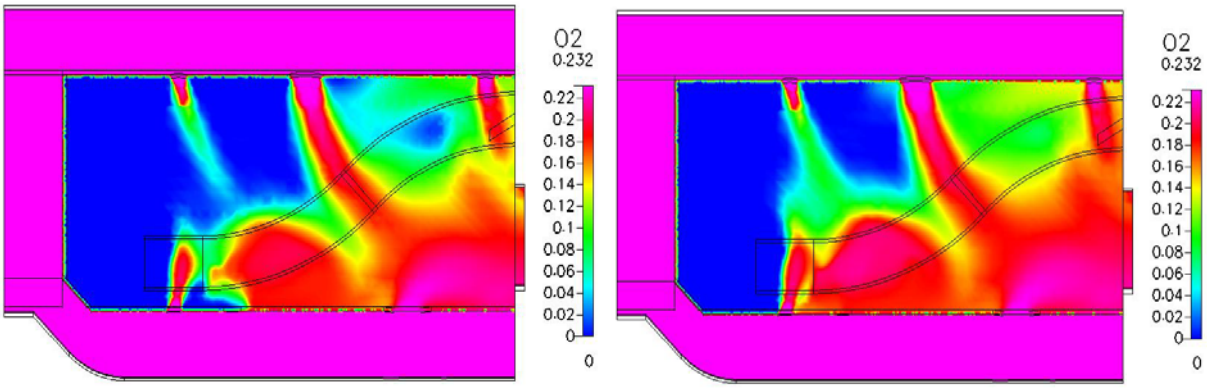

(a) Methane concentration 100%

(b) Methane concentration 90%

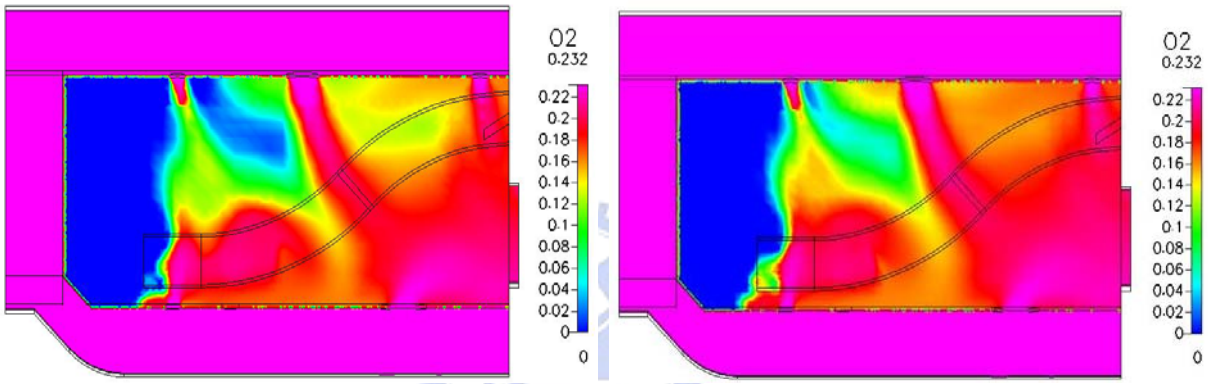

(c) Methane concentration 80%

(d) Methane concentration 70%

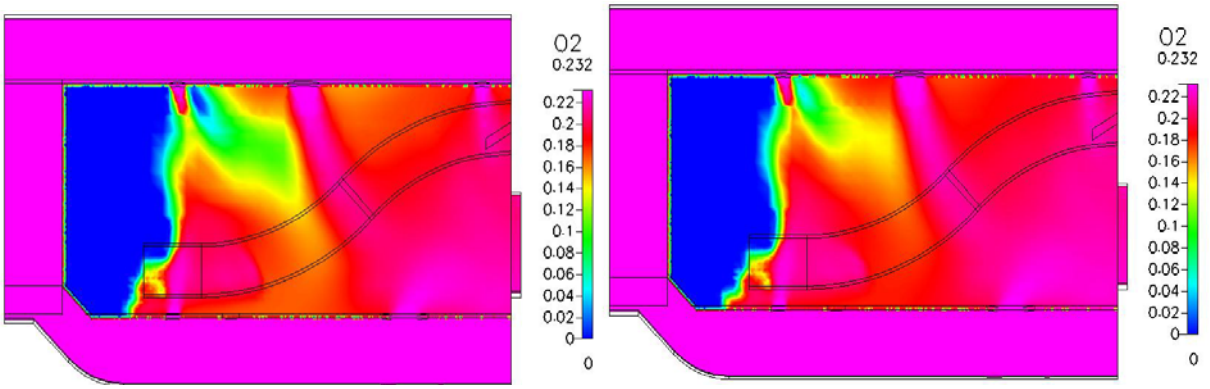

(e) Methane concentration 60%

(f) Methane concentration 50%

Fig. 4-15 Distributions of O_2 mass fraction for combustion case 155000 rpm (7.5 degrees cross-section)

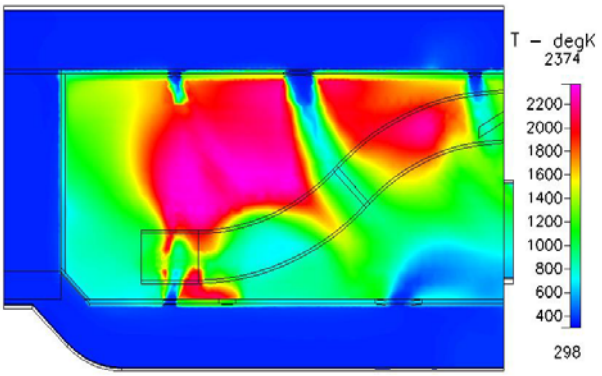

(a) Methane concentration 100%

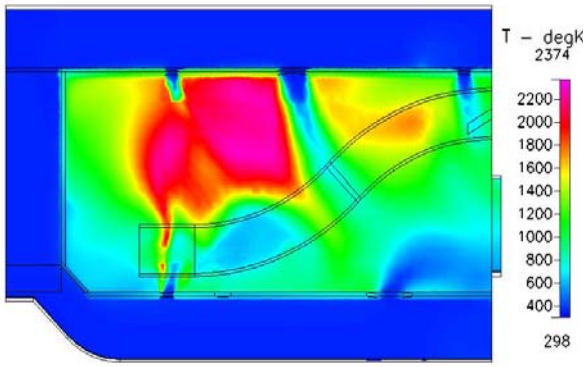

(b) Methane concentration 90%

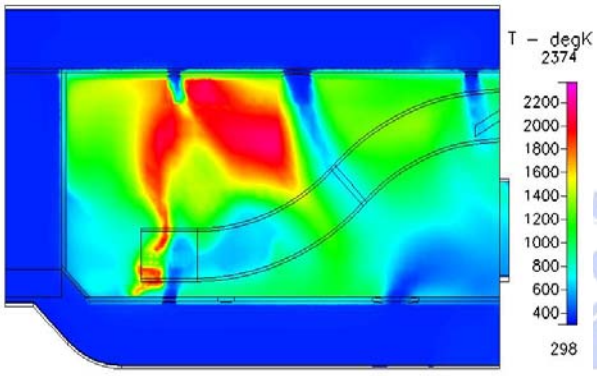

(c) Methane concentration 80%

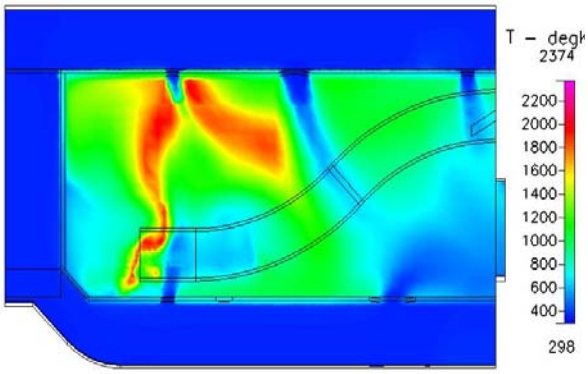

(d) Methane concentration 70%

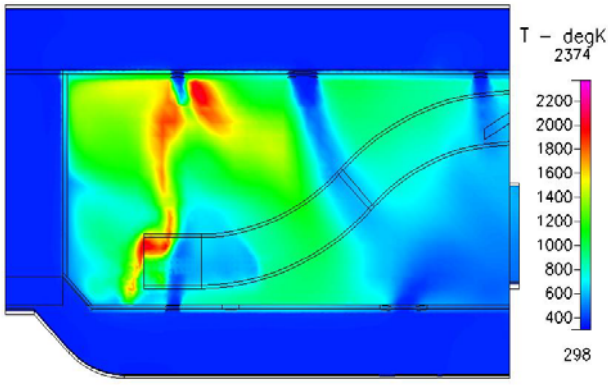

(e) Methane concentration 60%

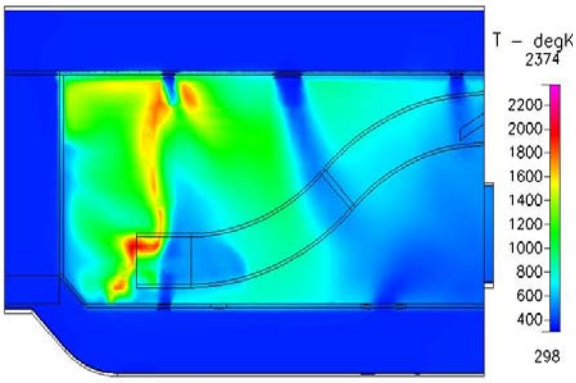

(f) Methane concentration 50%

Fig. 4-16 Distributions of temperature for combustion case 155000 rpm (7.5 degrees cross-section)

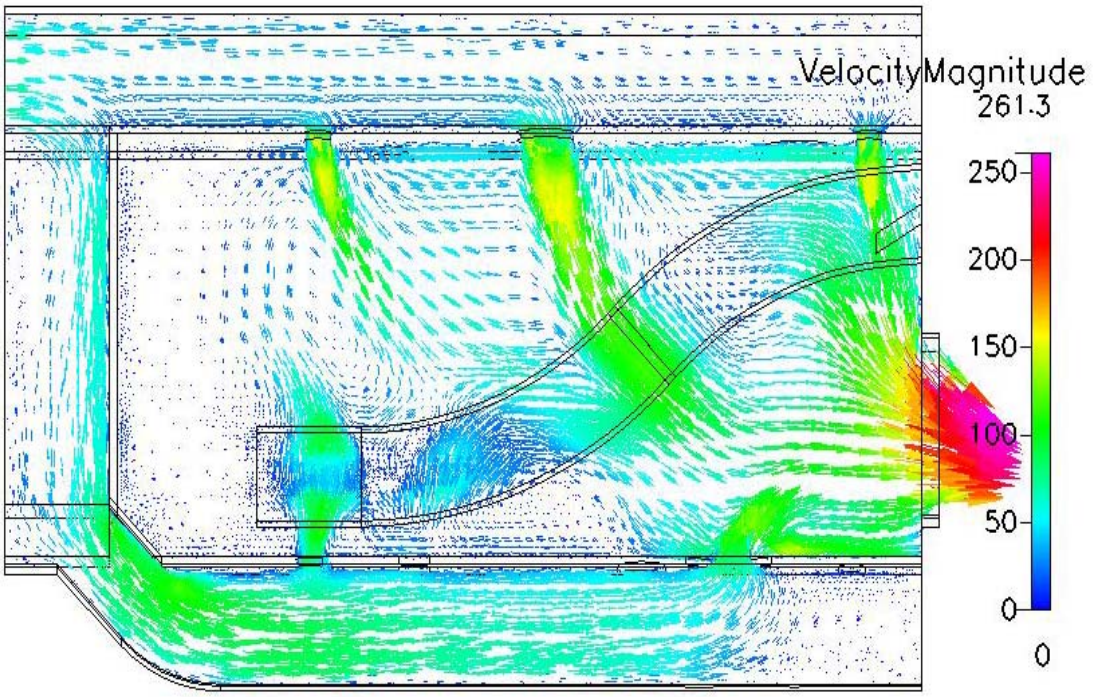

(a) Methane concentration 100%

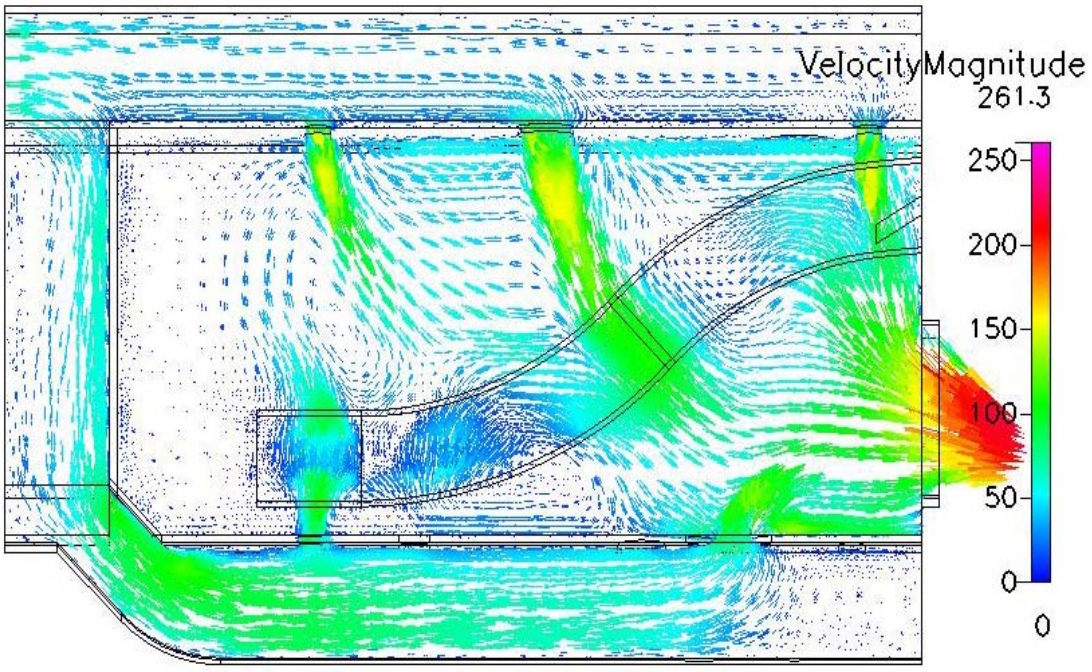

(b) Methane concentration 90%

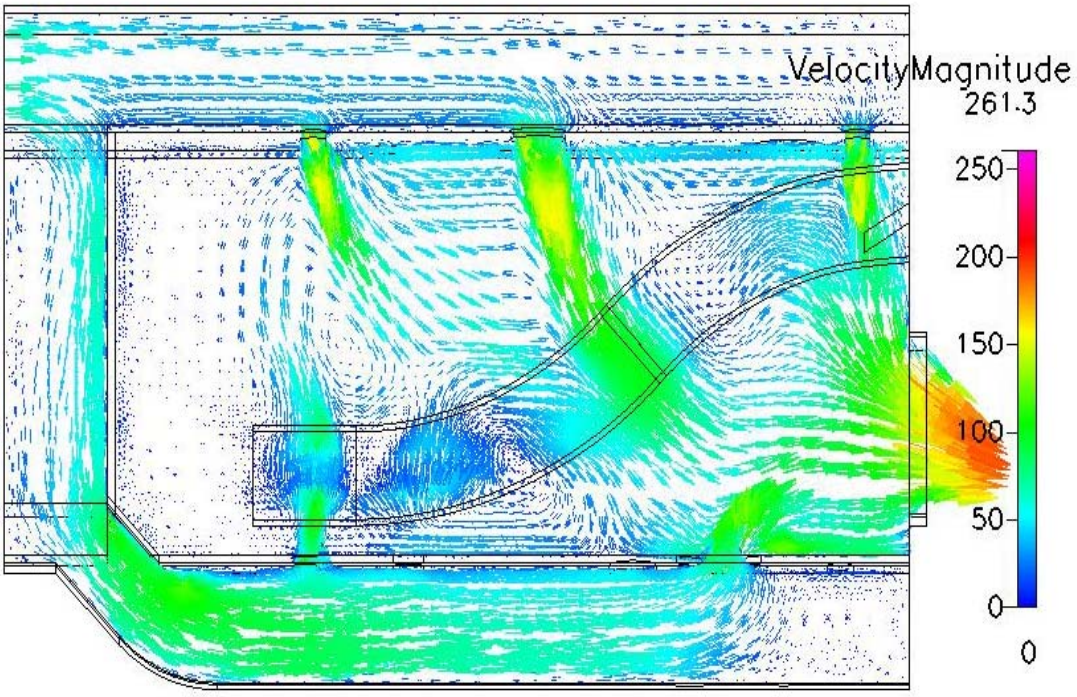

(c) Methane concentration 80%

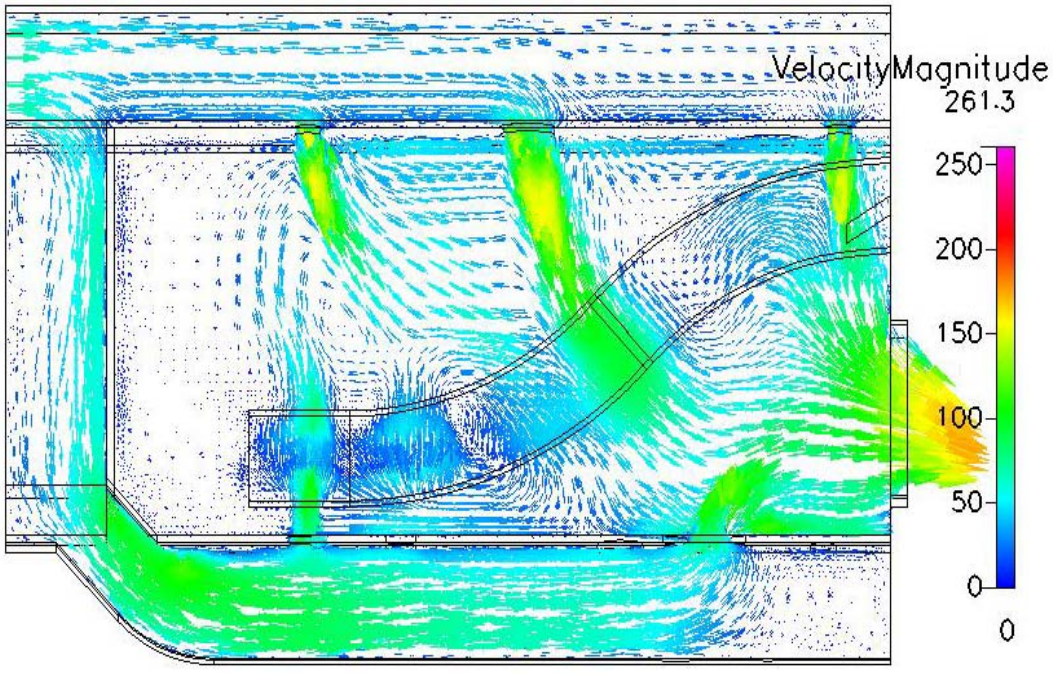

(d) Methane concentration 70%

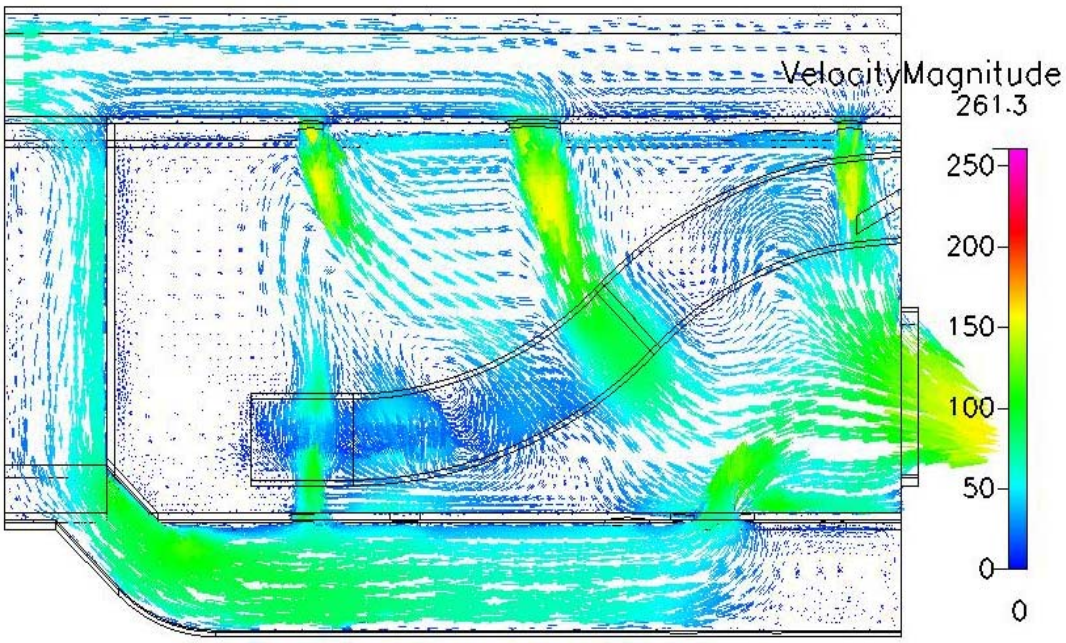

(e) Methane concentration 60%

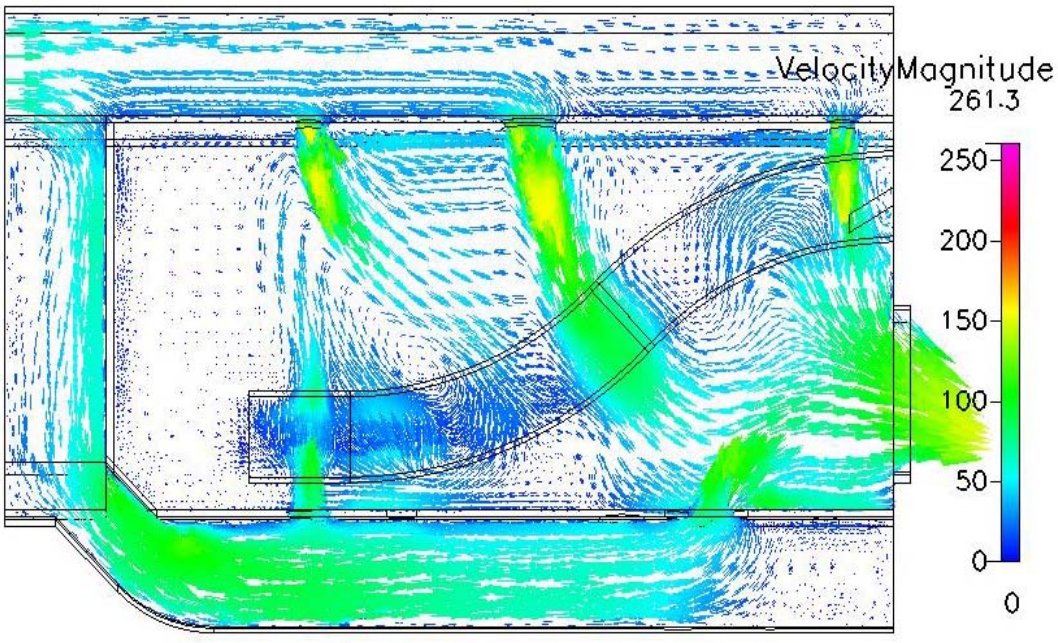

(f) Methane concentration 50%

Fig. 4-17 Velocity vector of flow field for combustion case 155000 rpm (7.5 degrees cross-section)

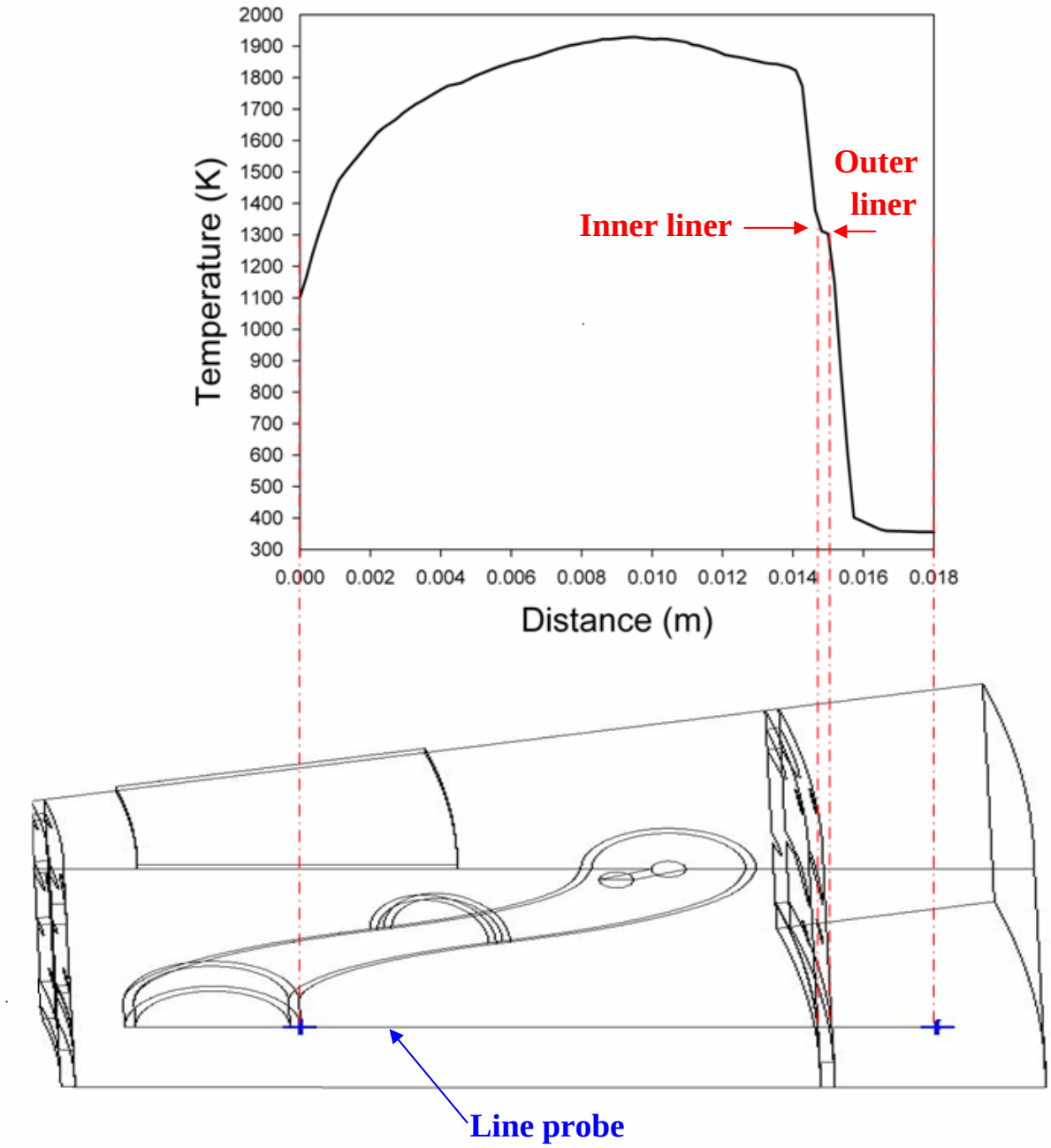

Fig. 4-18 Temperature distribution on line probe on symmetric face

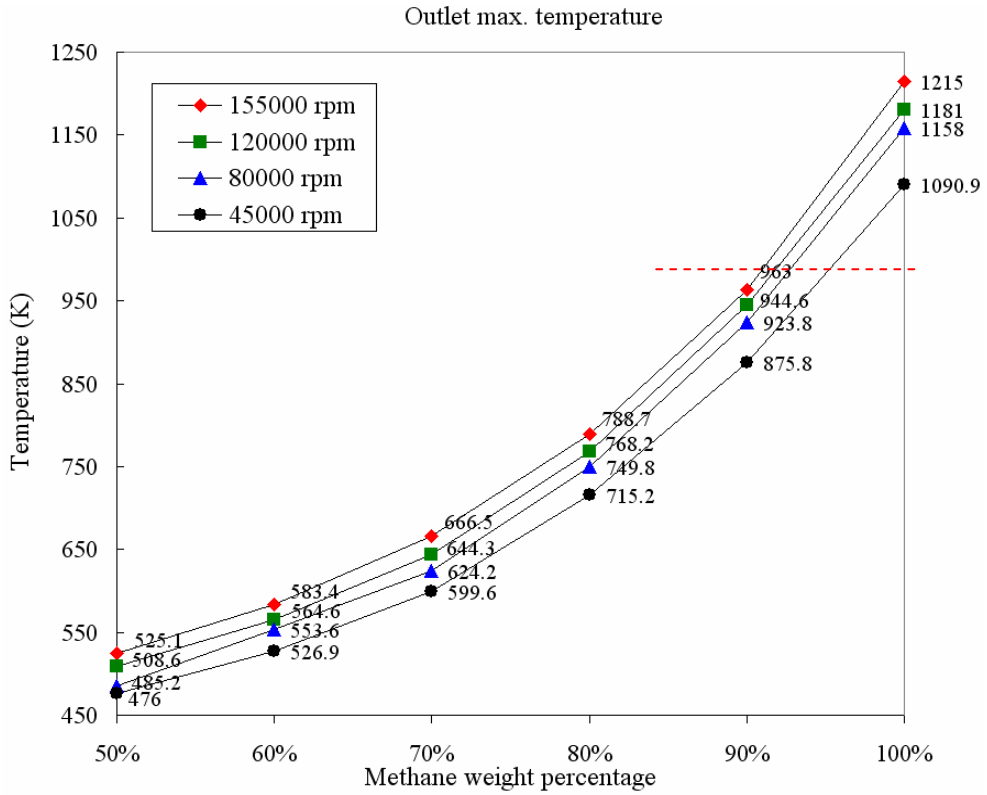

Fig. 4-19 Maximum temperature of combustor outlet

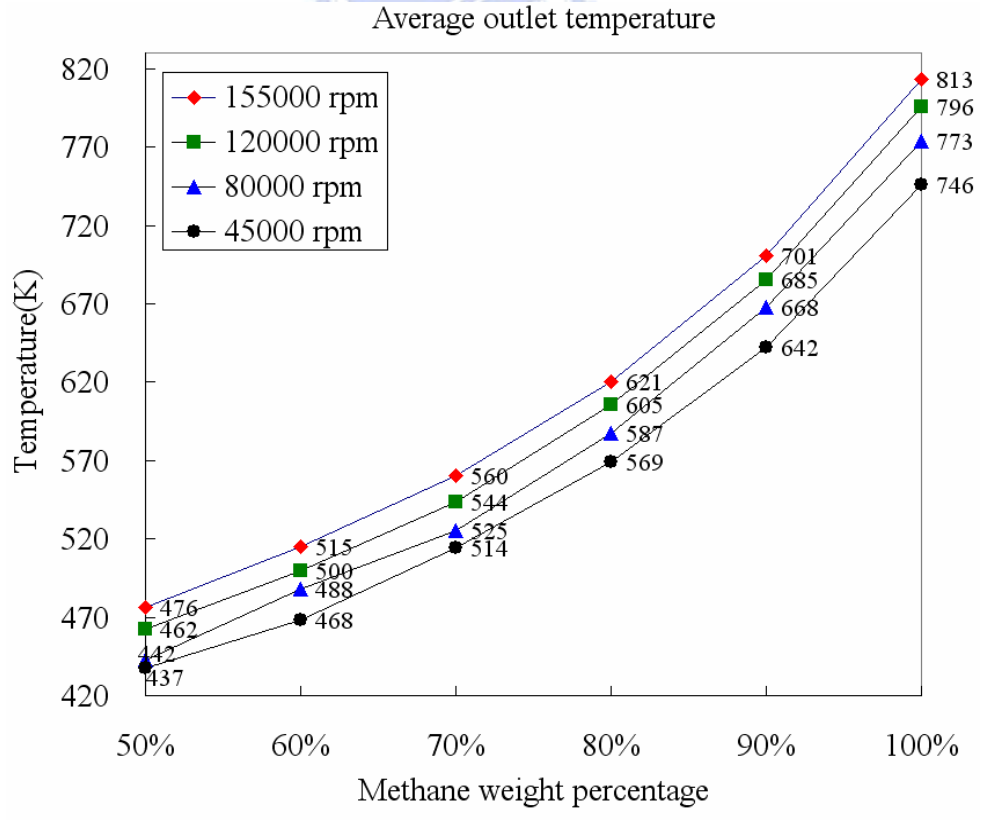

Fig. 4-20 Average temperature of combustor outlet

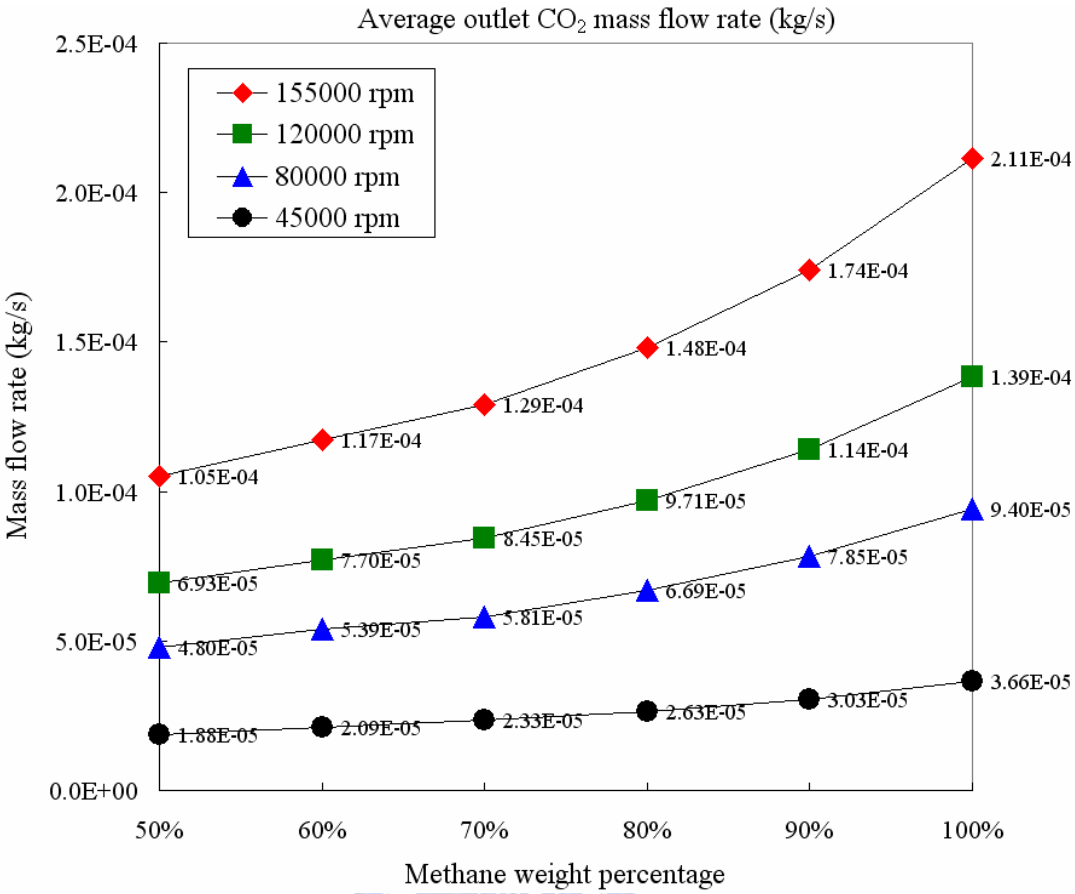

Fig. 4-21 Average CO_2 mass flow rates of combustor outlet

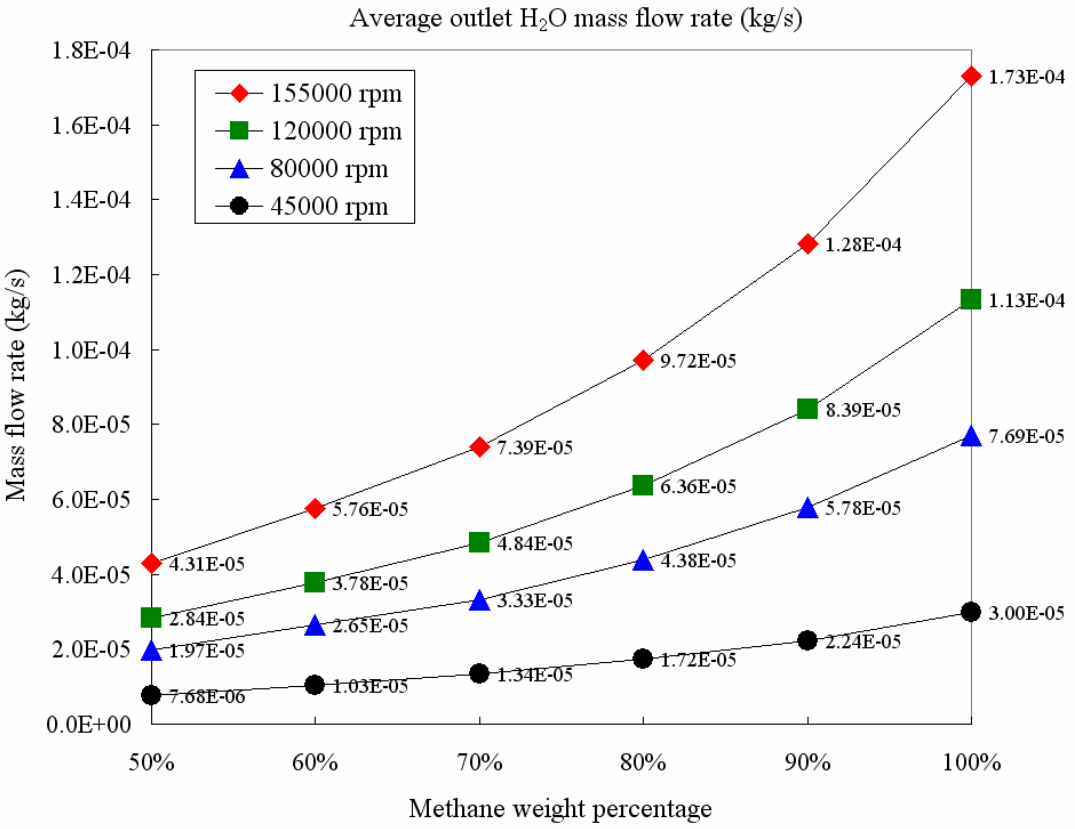

Fig. 4-22 Average H_2O mass flow rates of combustor outlet

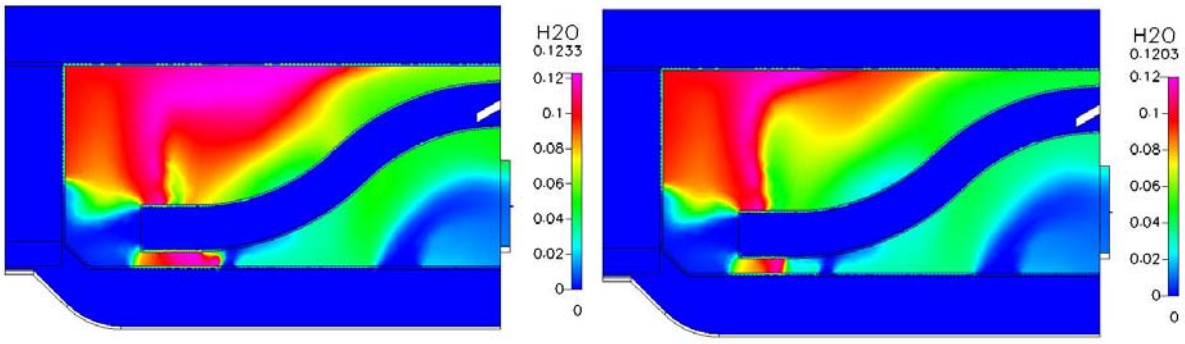

(a) Methane concentration 100% (b) Methane concentration 90%

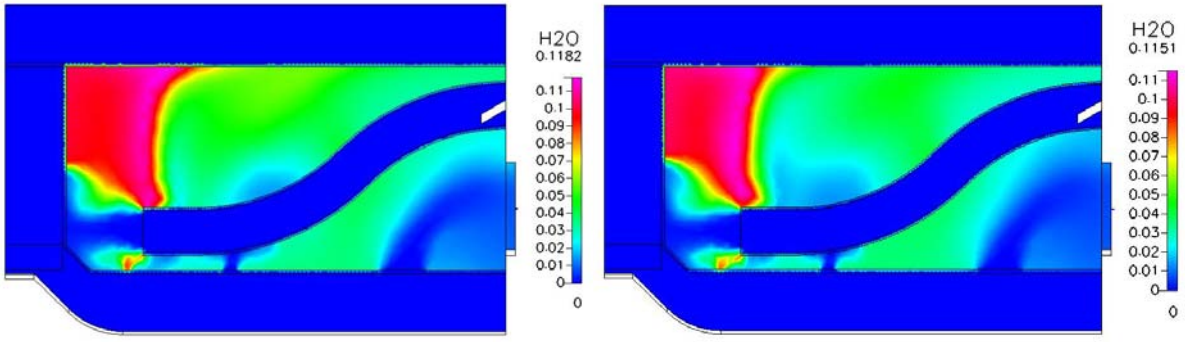

(c) Methane concentration 80% (d) Methane concentration 70%

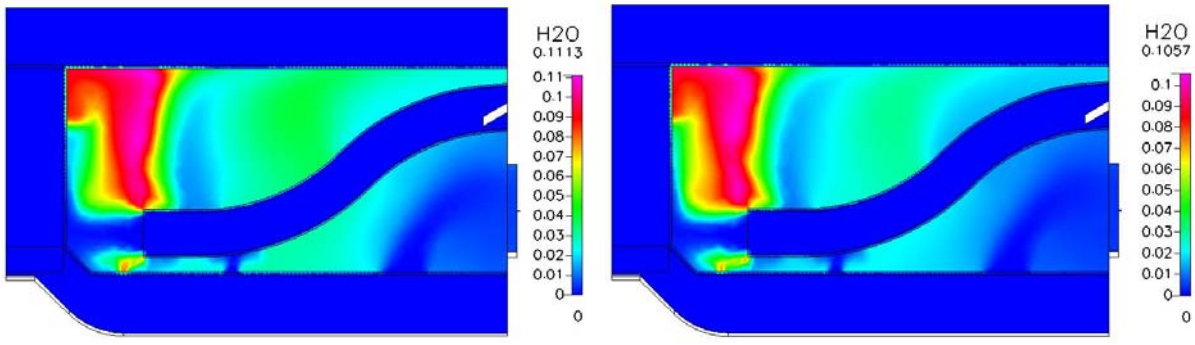

(e) Methane concentration 60% (f) Methane concentration 50%

Fig. 4-23 Mass fraction distributions of product H_2O at symmetric face for case 155000 rpm

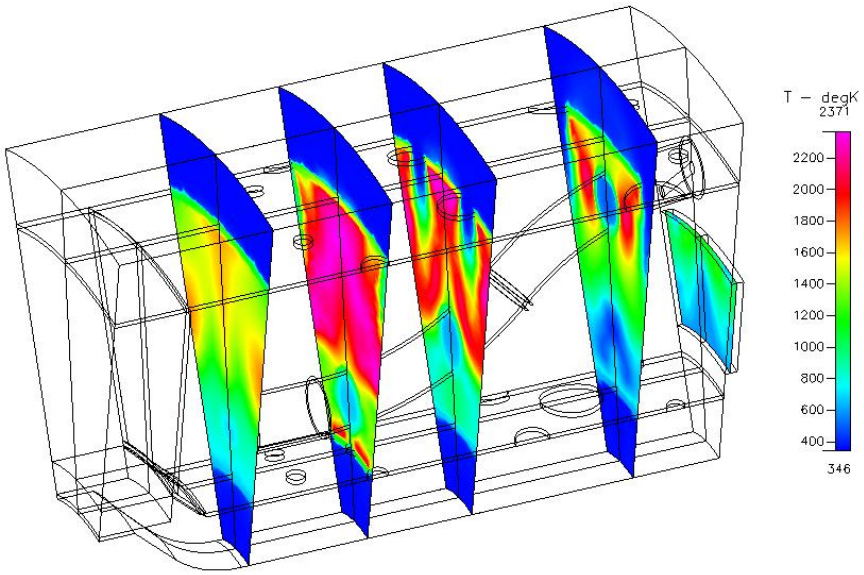

Fig. 4-24 Temperature patterns of combustor cross-sections

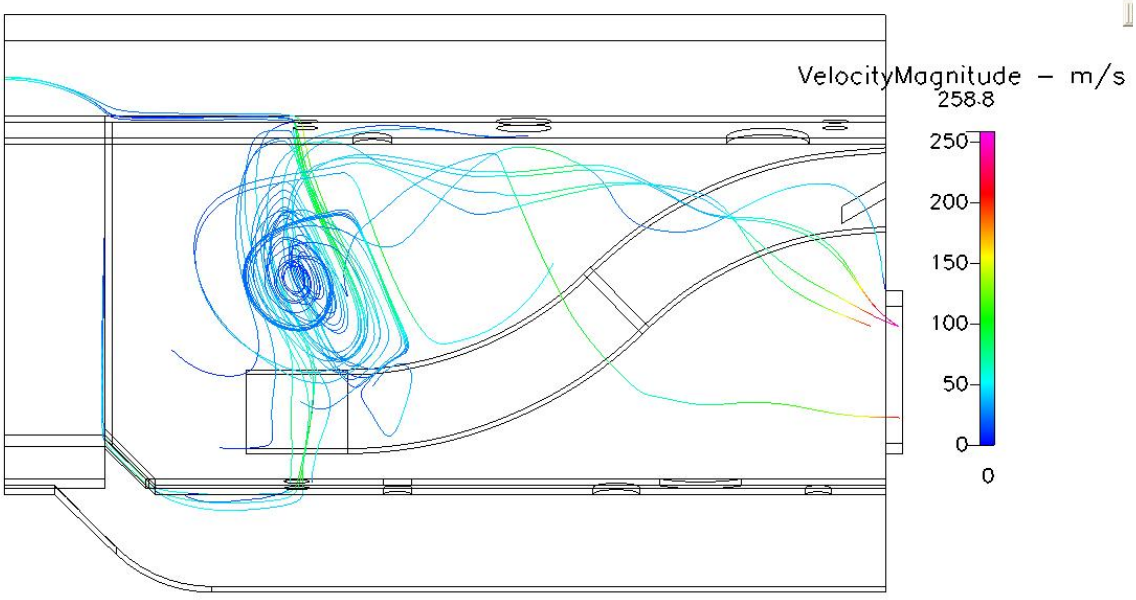

(a) Lateral view

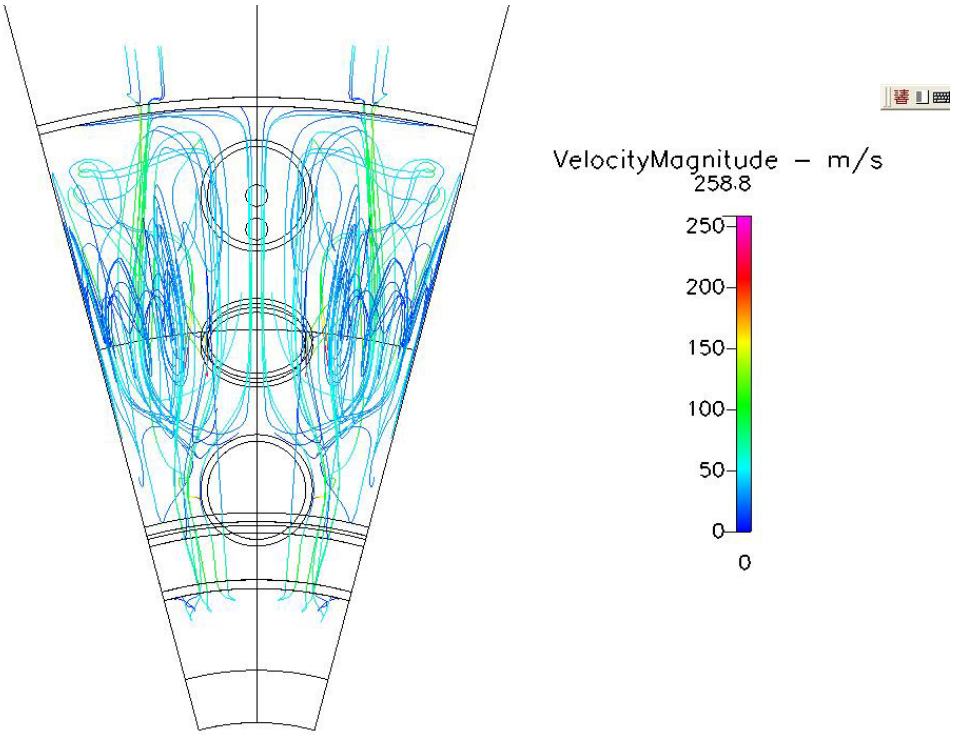

(b) Front view

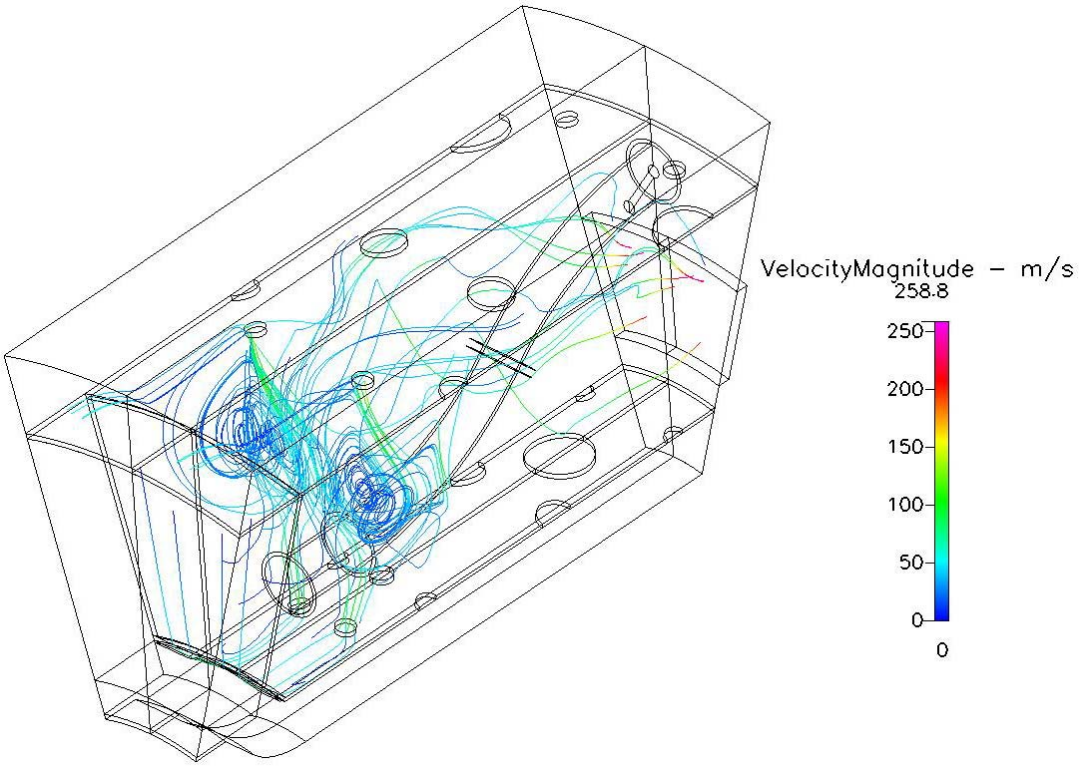

(c) The other view

Fig. 4-25 Stream lines in combustor